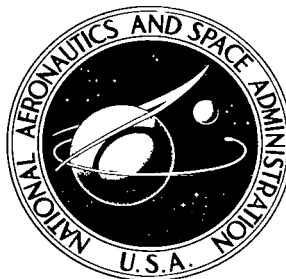
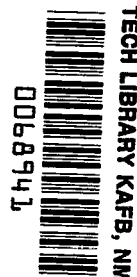


**NASA TECHNICAL
TRANSLATION**



NASA TT F-588

NASA TT F-588



ELEMENTARY PARTICLES AND COSMIC RAYS

V. A. Bezus and I. L. Rozenthal', Editors

Atom Press, Moscow, 1967

NATIONAL AERONAUTICS AND SPACE ADMINISTRATION • WASHINGTON, D. C. • MAY 1970

Quality Deficiencies In Original Document

 Missing Pages

 Bleed Through Pages

 X **Poor Quality Text/Image**



0068941

ELEMENTARY PARTICLES AND COSMIC RAYS

V. A. Bezus and I. L. Rozenhal', Editors

Translation of "Elementarnyye Chastitsy i Kosmicheskiye Luchi"
Atom Press, Moscow 1967

NATIONAL AERONAUTICS AND SPACE ADMINISTRATION

For sale by the Clearinghouse for Federal Scientific and Technical Information
Springfield, Virginia 22151 - CFSTI price \$3.00

ELEMENTARY PARTICLES AND COSMIC RAYS

V. A. Bezus and I. L. Rozenhal'

Annotation: This collection presents the papers on elementary particles and cosmic rays completed in recent years at the Chair of Experimental Nuclear Physics of MIFI. In order to expand the reading audience a significant place has been given in the collection to survey and semi-survey papers which recount the results of certain trends being developed at MIFI. The article contains both theoretical and experimental papers and methodical developments. A large number of the papers is devoted to the study of cosmic rays (the passage of cosmic rays, the study of cosmic μ mesons, photons and the primary spectrum, etc. A number of papers were completed on the basis of materials obtained in an accelerator, and will contain the methodology of processing the results. The collection is intended for scientists, graduate students and students majoring in the physics of elementary particles and cosmic rays. The article contains 69 figures, 16 tables, and 232 references.

Table of Contents

Annotation	iii
Cosmic Rays and Very Slow Particles I. L. Rozenthal'	1
The Energy Spectrum of Cosmic Muons of Ultrahigh Energies at Sea Level V. V. Borog, V. G. Kirillov Ugryumov, A. A. Petrukhin, V. V. Shestakov	17
Elastic π^+ -p-Scattering at a π^+ -Meson Energy at 2.06 GeV S. P. Kruchinin and K. N. Mukhin	30
The Mass Spectrum of Systems of Strange Particles Generated by the Interaction of π -Mesons with Light Nuclei V. S. Demidov, V. G. Kirillov-Ugryumov, A. A. Ponosov, V. P. Protasov, and F. M. Sergeyev	36
The Theory of Complex Moments and Resonance Nuclear Reactions V. V. Grushin and Yu. P. Nikitin	44
A Universal Method of Processing the Tracks of Arbitrary Curvature on Bubble Chamber Tracks K. N. Mukhin, A. S. Romantseva, I. A. Svetlolobov, M. M. Sulkovskaya, S. A. Chuyeva, R. S. Shlyapnikov	65
A Method of Registering the Energy of Charged Particles with a Proportional Light Counter V. G. Variamov, B. A. Dolgoshein and A. M. Rogozhin	77
Modeling Processes with Generation of Neutral Particles in Non-hydrogen Bubble Chambers K. N. Mukhin and I. A. Svetlolobov	81
Generation of High-Energy Muons during Interaction of Cosmic Ray Nuclei with Nuclei of Air Yu. D. Kotov	89
Cosmic γ -Radiation A. M. Gal'per and B. I. Luchkov	94
Absorption of π -Mesons by Complex Nuclei V. G. Kirillov-Ugryumov, F. M. Sergeyev and A. I. Fesenko	112
Study of the Physical and Chemical Properties of the Surfaces of Solids Using Nuclear γ -Resonance (The Mossbauer Effect) I. P. Suzdalev	121

COSMIC RAYS AND VERY SLOW PARTICLES

I. L. Rozenthal¹

ABSTRACT. The purpose of this paper is to show that an area exists where the characteristics of relativistic interactions overlap with properties of extremely slow particles (compared to cosmic rays). A significant fraction of cosmic ray energy is converted into ionization, i.e., into kinetic energy of slow electrons with energies of the order of 10-1,000 electron volts, i.e., close to the ionization potential. Before the energy of these electrons is converted into heat, they will radiate (during atomic excitation or during deceleration), which leads to new phenomena. The paper describes the various mechanisms which generate slow particles.

1. Introduction

It is usually assumed that the properties of cosmic rays are worked out by the characteristics of the interaction at relativistic (or quasi-relativistic) energies. A similar concept is related to a significant degree to the known characteristic of the energy spectrum of primary cosmic rays--its geomagnetic cut-off at energies of the order of a billion electron volts. Digressing for the meantime from the hypothetical existence in interstellar space of subcosmic rays with an energy less than a billion electron volts, we can say that just familiarity with fast cosmic particles is the physiological basis of a similar point of view. The purpose of this article is to show that a branch exists where singularities of relativistic interactions intersect with properties of extremely slow particles (compared to cosmic rays). The idea of such a position is quite simple. A significant part of the energy of cosmic rays is transformed into ionization, i.e. into kinetic energy of slow electrons with energies of the order of 10-1000 electron volts, i.e. close to the ionization potential. Before the energy of these electrons is converted into heat, they will radiate (when the atoms are excited or decelerated), which leads to new phenomena.

There is a serious barrier in the path of the quantitative study of this cycle of phenomena. As far as approaching a critical energy--the ionization potential I ($I \sim 10$ electron volts), usual computation methods, particularly the first Born approximation, become unsuitable. Unfortunately, other more modern methods of calculating the cross-sections also do not afford confidence in the accuracy of the results obtained with their help in the area of very low energies. On the other hand, these methods differ from the Born approximation by the awkwardness of their results. We shall therefore use in our estimates either the Born approximation or rely on experimental data.

*Numbers in the margin indicate pagination in the foreign text.

Although this article is devoted to consideration of the effects related to the passage of cosmic rays through matter, we shall note nevertheless that similar phenomena must play a very important role in many other branches of this. It is possible that the Northern Lights and scintillations encounters are caused to a significant degree by a similar mechanism. /4

2. The Spectrum of Secondary Electrons

The basic mechanism of slow electron genesis is the δ -process. The probability $W(E_0, E)dE$ of δ -electron formation with an energy in the range of E to $E+dE$, and with the particles with an energy E_0 is determined by the familiar expression

$$W(E_0, E) = \frac{2 C m}{\beta^2} \frac{dE}{E^2} \left[1 - \beta^2 \frac{E}{E_{\max}} + \frac{1}{2} \left(\frac{E}{E_0 + m} \right)^2 \right], \quad (1)$$

where

$$C = \pi n \frac{Z}{A} r_e^2; \quad E_{\max} = 2m \frac{P^2}{m^2 + M^2 + 2m(P^2 + M^2)^{1/2}};$$

n is the number of atoms in a column having a height equal to the length of the path and a cross-section of 1 cm^2 ; the speed of light $C = 1$; m is the mass of the electron; β is the speed of the incident particle; P and M are the pulse and mass of the incident particle; and E and E_0 are the kinetic energies of the electron and the incident particle.

For a more interesting case (for us) $P \ll M^2/m$, $E_{\max} \sim 2m(\beta^2/1-\beta^2)$. If $M \ll m$ and $E_0 \sim M$, the last member in expression (1) is negligible $\left[\ll \left(\frac{m}{M} \right)^2 \right]$.

The probability of δ -electron formation in a hydrogen layer having a thickness $x = 1 \text{ g/cm}^2$ for this case is

$$W(E_0, E) dE = \frac{0,3m}{\beta^2} \frac{dE}{E^2} \left[1 - \frac{E}{2m} \left(\frac{M}{E_0} \right)^2 \right]. \quad (2)$$

We shall assume that the differential spectrum of primary cosmic proton is in the form:

$$P(E_0) dE_0 = \begin{cases} A E_0^{-\gamma} dE_0 & \text{when } E_0 > 500 \text{ MeV} = E_{0\min}; \\ 0 & \text{when } E_0 < 500 \text{ MeV}. \end{cases} \quad (3)$$

where E_0 is the kinetic energy of the protons and Mev, $\gamma = 2.6$, and $A = 10^5$.

The spectrum of (3) is a rough approximation of the spectrum of primary cosmic rays in the solar system. The value of index γ in the true spectrum begins to decrease in the range of $E_0 \sim 1$ GeV and passes through zero in the range of $E_0 \sim 500$ MeV. Therefore, the following analyses claim an accuracy only by the order of magnitude.

We should also note the other circumstance. It is assumed in computations /5 that primary cosmic rays consist of protons. Calculation of complex nuclei in the composition of primary radiation approximately doubles the number of δ -electrons.

The spectrum of δ -electron generation is

$$\Gamma(E) dE = dE \int_{E_{0\min}(E)}^{\infty} W(E_0, E) P(E_0) dE_0, \quad (4)$$

where

$$E_{0\min} = \begin{cases} 500 & \text{when } E < 2 \text{ MeV;} \\ \frac{M}{4} \left[\sqrt{1 + \frac{2E}{m}} - 1 \right] & \text{when } E > 2 \text{ MeV.} \end{cases} \quad (5)$$

We obtain

$$\begin{aligned} \Gamma(E) &= \frac{0,2}{E^2}; \\ E &< 2 \text{ MeV;} \end{aligned} \quad (6)$$

$$\begin{aligned} \Gamma(E) &= \frac{0,7}{E^2} \left[\sqrt{\frac{2E}{m}} - 1 \right]^{-(\gamma-1)}; \\ 2 &< E < 6 \text{ MeV;} \end{aligned}$$

$$\Gamma(E) = \frac{5}{E^2} \left(\frac{m}{2E} \right)^{\frac{\gamma}{2}}; \quad (7)$$

$$E > 6 \text{ MeV.} \quad (8)$$

with an accuracy of 15-20% from formulas (4) and (5).

It is apparent from expressions (6)-(8) that the probability of δ -electron formation with an energy ~ 1 MeV is quite high. It exceeds by 5-6 orders the probability of electron formation during π - μ -e-decay¹. It is more important for subsequent calculations that the generation spectrum (see expressions (6)-(8)), and the energy spectrum $\mathcal{P}(E)$ of secondary electrons in cosmic space. Approximately

¹ The spectrum of electron generation occurring during π - μ -e-decay was computed by V. L. Ginzburg and S. I. Syrovatskiy [1].

$$\mathcal{P}(E) = \Gamma(E) R(E), \quad (9)$$

where $R(E)$ is the mean path of an electron with an energy E . In order to determine the spectrum of $\mathcal{P}(E)$ it is necessary to solve the kinetic equation. When the spectrum does not depend on time (this case apparently occurs), the kinetic equation may be written in the form

$$\frac{d\mathcal{P}}{dx} = \Gamma(E) + \frac{d\mathcal{P}}{dE} \cdot \frac{dE}{dx}. \quad (10)$$

Assuming that the spectrum of \mathcal{P} at any point of space is identical, we obtain /6

$$\mathcal{P}(E) = \int_0^E \frac{\Gamma(E') \frac{dE'}{dx}}{\frac{dE}{dx}}. \quad (11)$$

In a special case when $\Gamma(E) \sim E^{-\gamma}$ and $-\frac{1}{\frac{dE}{dx}} \sim E^{\alpha}$ (γ, α — are constants and the integral of (11) is converted into expression (9). For relativistic particles $\alpha = 0^1$ (in the energy ranges of $E \sim 0.1-1$ MeV for aluminum $\alpha \sim 0.3$ [2]). In a non-relativistic case [3]²

$$-\frac{dE}{dx} = \frac{2Cm^2}{E} \ln \frac{E}{I} \sqrt{\frac{e}{2}}. \quad (12)$$

Ignoring the logarithmic dependence for the power spectrum of $\mathcal{P}(E)$, we will obtain (9).

We should note that formula (12) is valid only for a case of $E \gg I$. The whole difficulty of a quantitative analysis of the effects related to the slow particles (about which we talked above) is the impossibility of accurately assessing the role of electrons with energies $\lesssim I$.

3. The Origin of Isotropic Cosmic X-Radiation

Two types of cosmic X-radiation have been discovered in recent years-- a) that related to specific point sources and b) the isotropic component of X-radiation clearly unrelated to point sources.

We shall attempt to explain the latter phenomenon in this section of the article. A number of hypotheses now exist explaining isotropic X-radiation.

¹ Ignoring the logarithmic increase of ionization as energy increases.

² Formula (12) takes into consideration total losses including the energy of atomic excitation.

The most interesting in our view will be those related to a very hot universe [4, 5] and the reverse Compton effect of metagalactic electrons in relict photons [6, 7].

We shall make a distinction here between the different explanations of isotropic X-radiation, which is a very interesting question in itself. It is not possible to explain this at present; additional measurements of the energy spectrum of isotropic X-radiation are needed for this. We shall dwell in more detail only on an explanation of isotropic X-radiation. Quite similar explanations were expressed independently by Hayakawa and Matsuoka [8] and by this author [9]. We shall use expression (9) to calculate the spectrum of $\mathcal{P}(E)$, assuming that the electron path is

/7

$$R(E) = 0,25E^{1,3} \text{ when } E < 2 \text{ MeV,} \quad (13)$$

and

$$R(E) = \frac{E}{3,7} \text{ when } E > 2 \text{ MeV.} \quad (14)$$

Relation (13) was obtained by extrapolation of the value of the path in aluminum [2] with consideration of the fact that the mean ionization losses in hydrogen are approximately 1.5 times greater than in aluminum. Relation (14) reflects the fact that the mean losses for the relativistic particles comprise 3.7 MeV/g/cm².

The number of photons with energies of w and dw , formed in a 1 g/cm⁻² layer is

$$T(w) = \int_{E_{\min}}^{\infty} \mathcal{P}(E) \sigma_r(E, w) dw, \quad (15)$$

where $E_{\min} = 0.01$ MeV (insofar as we are interested in X-ray photons with an energy of 0.0015-0.007 MeV).

We further assume that the probability $\sigma_r(E, w)dw$ of photon Bremsstrahlung with an energy of w and dw , having an electron with energy E on a path of 1 g/cm⁻² has the form:

$$\sigma_r(E, w) = \frac{8 \cdot 10^{-3}}{w}. \quad (16)$$

Formula (16) is valid if $E > 2$ MeV (an ultrarelativistic case, complete shielding)

$$\sigma_r(E, w) = \frac{10^{-3}}{w} \cdot \frac{m}{E} \ln \frac{4E}{w}. \quad (17)$$

Formula (17) was obtained from the familiar formula for Bremsstrahlung of non-relativistic electrons in which $E = E^1$ (where E^1 is the energy of the electron after collision) was placed under the logarithmic sign for analysis.

Formulas (16) and (17) join poorly since they are both valid only by an order of the magnitude in the intermediate range of $E \sim m$.

Using formulas (6)-(8) and (16)-(17), it is easy to establish that $1.2-1.3 \cdot 10^{-2}$ particles/(cm²·sec) are emitted at 1 g/cm^{-2} in the range of $1.5 < w < 7$ kiloelectron volts.

The length of the path according to the visual beam is $6 \cdot 10^{-2} \text{ g/cm}^{-2}$ in a direction toward the galactic center. Therefore, a flux of decelerated photons, determined by the δ -process from nucleons with an energy of $E_0 > 500 \text{ MeV}$, is $\frac{1}{8}$ equal to 10^{-3} particles/cm²/sec⁻¹/steradian⁻¹, which is approximately three orders less than that observed ($5 \text{ particles/cm}^{-2}/\text{sec}^{-1}/\text{steradian}^{-1}$) [10].

We shall try to estimate the possible photon flux generated by δ -electrons which form in turn sub-cosmic protons ($E_0 < 500 \text{ MeV}$). Nothing is known of the presence of such protons in interstellar space. Let us assume that the spectrum of sub-cosmic protons has the form

$$P_1(E_0) dE_0 = BE_0^{-\gamma_1} dE_0 (10 < E_0 < 500 \text{ MeV}), \quad (18)$$

where constants B and γ_1 are determined from the conditions: 1) joining of both spectra when $E_0 = 500 \text{ MeV}$ and 2) the equality of the calculated value of X-ray photon intensity to the experimental value.

For the spectrum (18)

$$\begin{aligned} \Gamma(E) dE = 0,15 B m M \frac{dE}{E^2} \int_{\frac{ME}{4m}}^{500} E_0^{-(\gamma_1+1)} \times \\ \times \left[1 - \frac{E}{m} \left(1 - \frac{2E_0}{M} \right) \right] dE_0. \end{aligned} \quad (19)$$

Using the conditions of joining and relations (13) and (17) we obtain a γ -photon flux in the range of $1.5-7 \text{ KeV}$ equal to $\frac{10^{-3} \cdot 2\gamma_1}{\gamma_1(\gamma_1 + 0,7)}$.

Assuming this expression to be equal to 5 (the experimental value of the X-ray flux, we obtain $\gamma_1 \sim 2.3$. The hypothesis of the existence of sub-cosmic rays¹ is also advanced in [8] to explain isotropic X-radiation. However, "internal" Bremsstrahlung-photon emission when electrons are accelerated during the δ -process²--is considered instead of ordinary Bremsstrahlung. A serious question arises about the argumentation for the existence of sub-cosmic rays. Hayakawa and others [11] advanced the hypothesis for the existence of a large flux of sub-cosmic rays, connecting them to heating of the interstellar gas. V. L. Ginsburg and L. M. Ozernoy [5] linked metagalactic sub-cosmic rays to a model of a hot universe. It is necessary, however, to note that the energy of cosmic radiation determined by (18) will be approximately 1.5-2 orders greater in the galaxy than the energy corresponding to the spectrum of (3). It is difficult to reconcile the circumstance with the proposal that the basic sources of galactic cosmic rays are supernova (assuming the invariability of frequency and output of supernova flares). On the other hand, a certain argument in favor of the δ -mechanism considered is the unconstrained explanation of a large number of electrons with an energy of ~ 1 MeV, observed beyond the boundaries of the atmosphere [12]. It is important to determine the sign of the charge of these electrons in order to verify the stated hypothesis.

/9

4. The Energy Balance of Cosmic Rays in the Galaxy

Let us now examine the channels for dissipation of cosmic ray energy during their passage through the interstellar medium. This question is important from the viewpoint of cosmic space being heated by cosmic rays [4, 5, 11].

Although it is considered natural that the entire energy of cosmic rays is converted to heat, in reality, this question is far from clear because of the presence of an intermediate δ -mechanism.

Let us assume henceforth that cosmic rays consist of nucleons, and interstellar gas--from non-ionized hydrogen. Although there are heavier nuclei in the primary component of cosmic rays, and although interstellar hydrogen is partially ($\sim 10\%$) ionized and atoms and heavier elements are present in the interstellar medium, the corrections determined by the effect of these factors are apparently less than the ambiguity of the cross-section values at very low energies ($E \sim I$).

Papers [13, 14] analyzed the fractions of cosmic ray energy converted into different components--in order of 1/4 total energy as converted into photons, an order of 1/3--into neutrinos, an order of 1/7--into electrons, and an order of 1/4--into ionization. Neutrinos and photons leave the galaxy almost without hinderance [1]. The fate of electrons is more interesting, the energy of which is substantially (or even completely) expended within the boundaries of the galaxy. It is not difficult to estimate the energy spectrum $P_e(E_e)$ of electrons generated as a result of nuclear interactions and subsequent decays.

¹ True, with a spectrum somewhat different from that of expression (18).

² This effect was calculated in the classic manner.

$$\begin{aligned}
P_e(E_e) &\sim P(E_0) \quad E_e > 0,05E_0 \text{ min;} \\
P_e(E_e) &= 0 \quad E_e < 0,05E_0 \text{ min,}
\end{aligned}
\tag{20}$$

where E_0 is the initial energy of the electrons.

The equation describing the equation of electrons in time has the form

$$-\frac{dE}{dt} = c + bE + aE^2. \tag{21}$$

Assuming that the density of interstellar gas is $n = 0.1$ particle/cm³, and the intensity of the magnetic field in the galaxy is $H = 5 \cdot 10^{-6}$ oersted, we obtain $c_1 = 2.5 \cdot 10^{-8}$ sec⁻¹, which is a term describing ionization losses of $b = 5.5 \cdot 10^{-17}$ sec⁻¹, and bE is a term corresponding to Bremsstrahlung losses. This term in a certain range is actually weakly (logarithmically) dependent on the energy of the electrons and photons. Its numerical value is selected when $E = 50$ MeV and when no shielding conditions exist, i.e. at photon energies comparable to an energy of E_0 . (This range is greater when calculating total losses). It is necessary to consider shielding for E and relatively weak photon energies, i.e. X-ray or light energies. In this case $b = 7.3 \cdot 10^{-17}$ sec⁻¹. Thus, the losses according to formula (21) are approximately 1.3 times less than actual losses; $a = 10^{-25}$ (electron volts per second)⁻¹. The last term in the right member of equation (21) describes losses to magnetic Bremsstrahlung and the reverse Compton effect. /10

It is assumed when calculating the coefficient of a that the density of w_{ph} photons in the galaxy is $\ll 1$ ev/cm⁻³.

Solving equation (21) we obtain

$$\begin{aligned}
E &= \frac{\sqrt{\Delta}}{2a} \tan \left\{ \left[\frac{2}{\sqrt{\Delta}} \arctan \frac{b + 2aE_e}{\sqrt{\Delta}} - t \right] \frac{\sqrt{\Delta}}{2} \right\} - \frac{b}{2a}; \\
\Delta &= 4ac - b^2.
\end{aligned}
\tag{22}$$

Hence, it is easy to determine the line of the electrons relative to total losses.

$$T_e = \frac{2}{\sqrt{\Delta}} \left(\arctan \frac{b + 2aE_e}{\sqrt{\Delta}} - \arctan \frac{b}{\sqrt{\Delta}} \right). \tag{23}$$

[†] Calculations of the coefficients of a , b and c were based on the results of paper [1].

Let us write total energy losses for each of the processes separately.

$$\begin{aligned}\epsilon_{ei} &= cT_e; \\ \epsilon_{er} &= b \int_0^{T_e} E(t) dt; \\ \epsilon_{emr} &= a \int_0^{T_e} [E(t)]^2 dt,\end{aligned}\tag{24}$$

where ϵ_{ei} , ϵ_{er} , and ϵ_{emr} are total losses to ionization, Bremsstrahlung and magnetic Bremsstrahlung respectively. Let us cite as an example the energy losses for two values of E_e with consideration of the influence of the reverse Compton effect where $w_\gamma = 0.3 \text{ ev/cm}^{-3}$ (Table 1).

Table 1

$E_e, \times 10^{-7} \text{ ev}$	$\epsilon_{ei}, \times 10^{-7} \text{ ev}$	$\epsilon_{er}, \times 10^{-7} \text{ ev}$	$\epsilon_{emr}, \times 10^{-7} \text{ ev}$	$\epsilon_{ek}, \times 10^{-7} \text{ ev}$
50	28	13	6,4	2,2
200	45	52	60	20

Losses due to the reverse Compton effect are given in the last column on Table 1. We note that the relative (in %) dissipation of energy along different channels is strongly dependent on the value of n (Table 2).

/11

A substantial role in the distribution of relative losses is laid by the density of w_γ photons (Table 3).

Table 2

$n(\text{cm}^{-3})$	ϵ_i	ϵ_r	ϵ_{mr}
0,1	58	27	15
0,01	30	10	60

Table 3

$w_\gamma (\text{ph} \cdot \text{cm}^{-3})$	ϵ_i	ϵ_r	ϵ_{mr}	ϵ_k
0	40	34	32	0
1	34	24	23	23
10	20	8	10	70

The calculations and Tables 1-3 were done numerically with an accuracy of 5%. The values of relative losses in Tables 2 and 3 are presented after they have been averaged according to the spectrum of electrons of (20). Let us now try to clarify the specific forms of energy transfer initially expended by cosmic rays due to ionization. For this purpose, we must know the effective cross-sections of collisions at low energies. We shall give a summary of the cross-sections of elementary processes in this energy range and their approximations. We shall use formula (2) without a second member right up to an energy of

$E = 35$ ev for the cross-section of hydrogen atom ionization; we shall assume $d\sigma_\delta = 0$ at lower energies. A similar approximation has the following basis: a) the second term in the energy range of interest to us comprises 10^{-3} - 10^{-5} of the first; b) after integrating $d\sigma_\delta$ by E_δ we can obtain the value of a total cross-section of σ_δ ionization and can correlate it with the experimental data of [15]. It turns out that $\sigma_{\text{ext}}/\sigma_\delta = 1.7$ when $E = 200$ ev, at the same time that $\sigma_{\text{ext}}/\sigma_\delta = 0.6$ when $E = 40$ ev.

According to the analysis of [16], the total cross-section of $\sigma_i \sim \frac{1}{E_\delta}$ during δ -electron formation in an energy range of 13-100 ev, which also agrees with formula (2).

The cross-sections of hydrogen atom excitation during collision of slow electrons. Basically, excitation is determined by the $1s - 2p$ -transition (see the summary of excitation cross-section in the Born approximation). /12

The results of experimental study of $1s - 2p$ excitation cross-sections is given in Fayt's article [17]. The cross-section in the range of 10-250 ev may be approximated by the following expression:

$$\sigma_{12} = \begin{cases} 2\sigma_0(E - \epsilon_2) & 10 < E < 20 \text{ ev} \\ \sigma_0 & 20 < E < 250 \text{ ev} \\ \frac{250\sigma_0}{E} & 250 \text{ ev} > E, \end{cases} \quad (25)$$

$\sigma_0 \sim 10^{-16} \text{ cm}^2$; and ϵ_2 is the excitation energy of the second level.

Elastic collisions. The cross-section of $\sigma_y \sim 12 \sigma_0$ when $E = 12$ ev and then drops faster than $1/E^2$ to energies of 50 ev [18]. A fraction of energy equal to $m/M E \sim 5 \cdot 10^{-5}$ is converted to hydrogen on the average during each elastic collision.

Let us consider the processes which occur as ionization energy is absorbed. Since total ionization and excitation cross-section is $\sim 1E$ at $100 > E > 250$ ev, and the cross-section of elastic collisions decreases significantly faster, it is clear that multiple ionization and excitation will take place to energies of $E \gtrsim 250$ ev; the elastic processes play a negligible role. All three of the processes mentioned above become important in the range of $E < 250$ ev. In proportion to electron deceleration, excitation and elastic collisions are beginning to play an ever more important role.

According to our analyses which rely on the cross-sections presented above, it turned out that approximately 25% of all ionization energy is converted irreversibly into elastic collisions, and the remaining 75% is converted into lye, mainly into a Lyman series¹.

¹ We shall ignore here the process of ionized hydrogen recombination with subsequent emission of photons in the light and ultraviolet bands.

We shall analyze the lower boundary of the energy fraction which is converted into ultraviolet radiation, and the excitation cross-section of hydrogen atom electrons in the Born approximation. We shall find the relationship of the values of excitation energy and hydrogen atom ionization per unit of path. This relationship will also be (in the given approximation) the lower boundary of the desired fraction, since part of the ionization energy will again be converted into excitation photons. We shall present the cross-section bodies of hydrogen atom excitation by electrons:

$$\left. \begin{aligned} \sigma(1s-2s) &= \frac{6 \cdot 10^{-3}}{E} \left(1 - \frac{4 \cdot 10^{-3}}{E}\right) \sigma_0; \\ \sigma(1s-2p) &= \frac{7 \cdot 10^{-2}}{E} \left(\log, 8 \cdot 10^3 E - 1,2 + \frac{2,2 \cdot 10^{-3}}{E}\right) \sigma_0; \\ \sigma(1s-3s) &= \frac{1,9 \cdot 10^{-3}}{E} \left(1 - \frac{4 \cdot 10^{-3}}{E}\right) \sigma_0; \\ \sigma(1s-3p) &= \frac{1,1 \cdot 10^{-2}}{E} \left(\log, 8 \cdot 10^3 E - 1,1 + \frac{1,3 \cdot 10^{-3}}{E}\right) \sigma_0; \\ \sigma(1s-3d) &= \frac{9 \cdot 10^{-4}}{E} \left(1 - \frac{10^{-2}}{E} + \frac{5 \cdot 10^{-5}}{E^2}\right) \sigma_0; \\ \sigma(1s-4s) &= \frac{5 \cdot 10^{-4}}{E} \left(1 - \frac{4 \cdot 10^{-3}}{E}\right) \sigma_0; \\ \sigma(1s-4p) &= \frac{4 \cdot 10^{-3}}{E} \left(\log, 8 \cdot 10^3 E - 1,8 + \frac{10^{-3}}{E}\right) \sigma_0; \\ \sigma(1s-4d) &= \frac{4 \cdot 10^{-4}}{E} \left(1 - \frac{10^{-2}}{E}\right) \sigma_0, \end{aligned} \right\} \quad (26)$$

where E is given in kiloelectron volts¹.

/13

It follows from expressions of (26) that the main contribution to total excitation cross-section is made by the 1s - p2 and 1s - 3p transitions. It is known that the transition energies with a change of the principal quantum number in hydrogen atoms hardly differ from each other and are equal to an order to 10 ev. Therefore, we can summarize all cross-sections of (26) for energy analysis according to all similar transitions, assuming that an energy of ~ 10 ev is lost in each transition. We obtain a total cross-section

$$\sigma_r \sim \frac{8,5 \cdot 10^{-2}}{E} \left(\log, 8 \cdot 10^3 E - 1,2 + \frac{2 \cdot 10^{-3}}{E}\right) \sigma_0 \quad (27)$$

and total losses in kiloelectron volts on a path of 1 g/cm⁻² is

$$-\left. \frac{dE}{dx} \right|_{\text{exc}} = \frac{8,5N \cdot 10^{-4}}{E} \left(\log, 8 \cdot 10^3 E - 1,2 + \frac{2 \cdot 10^{-3}}{E}\right) \sigma_0, \quad (28)$$

¹ The cross-sections were computed by M. L. Fil'chenkov without consideration of the exchange on the basis of nonexcitation cross-sections of hydrogen atoms by protons (see for example paper [11]).

where N is an Avagadro number. Average energy losses due to ionization are expressed by relation (12) which may conveniently be written in the form

$$-\frac{dE}{dx}\Big|_{\text{ion}} = \frac{8\sigma_0 I^2}{E} N \ln \frac{E}{I} \sqrt{\frac{e}{2}}. \quad (29)$$

Strictly speaking, expressions (28) and (29) must be averaged according to the spectrum of (9) or (11) in order to compute the desired relation. Assuming that the spectrum of $\mathcal{P}(E)$ in an energy range of the order of 100 ev has a de-

creasing character even in the range of ~ 10 KeV. The relation $u = \frac{dE}{dx}\Big|_{\text{exc}} / \frac{dE}{dx}\Big|_{\text{ion}}$ will be determined by the values of E which lie near the lower boundary of the spectrum of $\mathcal{P}(E)$, i.e., by the values of E only slightly exceeding I . Let us give the values of the relation of $E = 30$ ev ($\sim 2 I$) and $E = 60$ ev ($\sim 4 I$):

$$u(E = 30 \text{ ev}) \sim 0,5; \quad u(E = 60 \text{ ev}) \sim 0,4.$$

Thus, approximately half of the energy withdraws to the ultraviolet range even at similar extreme estimates. The question about the future fate of ultraviolet radiation is not yet clear. Apparently, according to [19], the main process of energy absorption of the ultraviolet spectrum is photoabsorption of interstellar dust. For example, if we accept the thesis of [19] that the number of dust particle comprises $5 \cdot 10^{-12} \text{ cm}^{-3}$, and the effective cross-section of photoionization is equal to a geometrical cross-section of 10^8 cm^2 , the path of ultraviolet radiation is equal to 1 parsec by ignoring the possible consumption of ultraviolet radiation energy due to other processes within the limits of a parsec and ignoring secondary processes inside the dust particles, ultraviolet radiation energy is almost completely converted into heat without reaching the solar system or the borders of the galaxy. If the γ -photon path is substantially greater than a parsec (and we compare it with the dimensions of the galaxy) or the regeneration coefficient of ultraviolet radiation in visible light is close to unity, a significant part of ionization energy will be converted to light radiation.

It is interesting to compare total energy converted into ultraviolet radiation in the galaxy with the value of the energy leaving the galaxy in the form of light. Estimating only the order of both values, we use the following values: we assume a volume of the galaxy of an order of 10^{69} cm^3 , and its area as 10^{46} cm^2 ; the density of photon energy as $w_{\text{ph}} \sim 0.1 \text{ ev/cm}^{-3}$, and the value of coefficient $c_1 = 10^{-8} \text{ sec}^{-1}$; and we also assume that all ionization energy is converted to ultraviolet radiation. In such a case the total energy converted into ultraviolet radiation from cosmic rays is of the order of $10^{51} \text{ ev/sec}^{-1}$, and the energy leaving the galaxy in the form applied is of the order of $10^{55} \text{ ev/sec}^{-1}$.

In conclusion, let us estimate the energy given off by δ -electrons during

the process of Bremsstrahlung. We shall use the generation spectrum $\Gamma(E)$ δ -electrons and the δ -electron path in hydrogen used in paper [9]. Since the expression for $R(E)$ is also suitable for $E \gtrsim 1$ KeV, we shall limit ourselves to consideration of δ -electrons satisfying this condition. The fraction Δ of total ionization energy converted into radiation in the range of w_{\min} - w_{\max} ,

/15

$$\Delta = \frac{\int_{E_{\min}}^{\infty} \Gamma(E) R(E) dE}{\alpha} \frac{\int_{w_{\min}}^{w_{\max}} \sigma(E, w) dw}{\alpha} \quad (30)$$

Here $\alpha = 3.7 \text{ MeV/g/cm}^{-2}$ and $\sigma = \frac{10^{-3}}{w} \cdot \frac{m}{E} \ln \frac{4E}{w}$ is the Bremsstrahlung cross-section (non-relativistic case) at 1 g/cm^{-2} . Computing the interval [30] in a logarithmic approximation, we obtain the following data (Table 4):

Table 4

	Radial band	Visible light	X-radiation
$\Delta =$	10^{-12}	10^{-7}	10^{-5}

The figures presented in Table 4 give only the lower boundary of the energy converted to radiation, since two factors are not considered here: 1) δ -electron radiation when $E < 1$ KeV and 2) δ -electron radiation of subsequent population (δ -electrons formed from δ -electrons of the first population). But it already follows

from Table 4 that δ -electrons may play a substantial role during formation of x-radiation (see §3).

5. Radiation and Extensive Air Showers Caused by Slow Particles

Let us examine a phenomenon directly related to radiation and extensive air showers. There are two important interrelated problems here. The first is related to the techniques for detecting extensive showers. We know that the frequency of extensive showers drops at a disastrous rate as their energy increases. Therefore, the question arises of increasing the effectiveness of the recording area of extensive showers due to possible emissions of extensive showers, and first, of their radio emission. The second problem, in its simplest statement, may be formulated in the following manner: where does the energy of extensive air showers go? The negligible part ($\sim 10^{-4}$) of the energy goes into Cerenkov radiation [20]. A. Ye. Chudakov long ago investigated the possibility of using the glow caused by atomic excitation of air by particles of extensive showers to record these showers. However, the investigations conducted by him [21] showed that even less energy is converted into a similar glow in the visible range than into Cerenkov radiation.

This important problem on the dissipation channels of extensive showers is still awaiting a solution. We shall try here to analyze the emissions of extensive showers caused by slow particles¹.

/16

¹ This problem was investigated by the author jointly with M. L. Fil'chenkov [22].

Let us dwell in more detail on the radio emission of extensive showers recently discovered [23]. Although mechanisms of radio emission genesis were proposed (see, for example, paper [24]), we feel that the quantitative side of hypotheses explaining the genesis of a radio emission is unclear. On the other hand, the coherent radiation of extensive air showers studied by G. A. Askaryan [24] is approximately coincident in alignment with the axis of an extensive shower and therefore could hardly be recorded at great distances from the axis. In this regard we think it is feasible to consider other mechanisms which predict isotropic or quasi-isotropic radiation.

Let us analyze the Bremsstrahlung of the electron component of extensive showers under the following assumptions:

a) The energy spectrum of the electron component is a Tamm-Belen'kiy [25] equilibrium spectrum $N(E)$ down to the very lowest energies¹.

b) The Bremsstrahlung cross-sections of an electron and a positron with an electron are equal and have the following form:

$$\left. \begin{aligned} \sigma_{er}(E, \omega) d\omega &= 11\alpha_e^2 \frac{m}{E} \cdot \frac{d\omega}{\omega} \ln \frac{E}{\omega} \quad E < m; \\ \sigma_{er}(E, \omega) d\omega &= \frac{16}{3} \alpha_e^2 d\omega \ln \frac{E^2}{m\omega} \quad E > m; \end{aligned} \right\} \quad (31)^2$$

c) The Bremsstrahlung cross-section of an electron with a nucleus is

$$\left. \begin{aligned} \sigma_{Nr}(E, \omega) d\omega &= \frac{8}{3} \alpha_e^2 Z^2 \frac{d\omega}{\omega} \ln \frac{E}{\omega} \quad E < m; \\ \sigma_{Nr}(E, \omega) d\omega &= \frac{16}{3} \alpha_e^2 Z^2 \frac{d\omega}{\omega} \ln (183 z^{-1/2}) \quad E > m. \end{aligned} \right\} \quad (32)^2$$

The number $T(\omega)d\omega$ of emitted photons on a path of 1 g/cm^{-2} is

$$T(\omega) d\omega = -d\omega \int_{\omega}^{\infty} \frac{dN}{dE} \sigma_r(E, \omega) \frac{N}{A}, \quad (33)$$

where $\sigma_r = \sigma_{er} + \sigma_{Nr}$, and Z and A are the charge and atomic weight of the nuclei.

Let us assume $w_1 = 2 \text{ ev}$ (the light band), $w_2 = 2 \cdot 10^{-6} \text{ ev}$ (the radio band) /17 and a radiation interval of $\Delta w_{1,2} = w_{12}$. The fraction of δ -energy (from the

¹Strictly speaking, the Tamm-Belen'kiy spectrum is calculated to electron energies of $E \sim 1 \text{ MeV}$. Extrapolation of the spectrum to energies of $E < 1 \text{ MeV}$ contains a definite arbitrariness.

²See the derivation of expressions (31) and (32) and paper [26].

total energy of the shower) converted into the light band is equal to $\delta_1 \sim 10^{-6}$ (the light band) and $\delta_2 \sim 10^{-12}$ (the radio-frequency range).

Let us analyze the emission of real δ -electrons formed when the shower passes through the atmosphere:

$$T_1(\omega) = - \int_{E_{\min}}^{\infty} \sigma_r(E_\delta, \omega) R(E_\delta) dE_\delta \int_{2E_\delta}^{\infty} \frac{dN}{dE} \Gamma(E, E_\delta) dE, \quad (34)$$

where $R(E_\delta)$ is the path of the δ -electrons in air; E_δ is the energy of δ -electrons. Unfortunately, this path has been studied insufficiently for very weak energies (less than 1 KeV). Function $R(E_\delta)$ was extrapolated by the expression $0.4 E_\delta^{1.3}$ [2]. If we set $E_{\delta_{\min}} = 10^{-3}$ MeV, then $\delta_1 \sim 1.5 \cdot 10^{-6}$ and $\delta_2 \sim 1.5 \cdot 10^{-12}$. If $E_{\delta_{\min}} = 10^{-2}$ MeV, these values will decrease five times.

Let us compare the analysis obtained with an observed intensity of flares [23], which are characterized by the following parameters: a pulse of 10^{-10} - 10^{-11} ergs; an antenna area of 1000 m²; an energy of extensive showers of 10^{17} ev $\sim 10^5$ ergs; $\Delta w = w/10$; and $w \sim 10^{-7}$ ev. The total energy of radio emission upsets a shower and at the range of $\Delta w \sim w/10$ caused by slow particles of the order of 10^{-9} ergs, significantly exceeds the observed value. However, we must bear in mind that this radiation (because of its quasi-isotropic nature) impinges on an area which substantially exceeds the antenna area. Thus, if the effective area onto which the layer energy impinges is $S \sim 1$ km², then an energy of 10^{-12} ergs impinges on the antenna, and if $S \sim 10$ km², then $w \sim 10^{-13}$ ergs.

Thus, there is an entire area determined by the capability of cosmic rays to form very slow particles. It is now difficult to accurately determine its boundaries, and the problems considered in this paper have not been strictly and finally resolved because of gaps in the knowledge of the behavior of very slow particles. One of the tasks of this article is to attract attention to this area which has been hardly developed until the present.

In conclusion, the author expresses gratitude to M. L. Fil'chenkov for discussion of certain problems touched on in the paper.

REFERENCES

1. Ginzburg, V. L. and S. L. Syrovatskiy, *Proiskhozhdeniye Kosmicheskikh Luchen*, [The Origins of Cosmic Rays], An SSSR Academy of Sciences Press, Moscow, 1963.
2. Katz, L and A. Penfold, *Journal Revs. Mod. Phys.*, Vol. 24, p. 28, 1952.
3. Landau, L. D. and Ye. M. Lifshits, *Kvantovaya Mekhanika*, [Quantum Mechanics], Fizmatgiz Press, Moscow, 1963.
4. Hoyle, F., *Astrophys. J.*, Vol. 137, p. 993, 1963.

5. Ginzburg, V. L. and L. M. Ozernoy, *Astron. Zh.*, Vol. 42, p. 943, 1965.
6. Felten, Y. E., *Journal Phys. Rev. Lett.*, Vol. 15, p. 1003, 1965.
7. Rozenthal', I. L., *Astron. Zh.*, Vol. 44, 1967.
8. Hayakawa, S and M. Matsuoka, *Journal Progr. Theoret. Phys. Suppl.*, Vol. 30, p. 206, 1964.
9. Rozenthal', I. L., *Kosmicheskiye Issledovaniya*, Vol. 4, p. 404, 1966.
10. Ginzburg, V. L. and S. I. Syrovatskiy, *Uspekhi Fiz. Nauk*, Vol. 84, p. 201, 1964.
11. Hayakawa, S., S. Nishimura and K. Takayanagi, *Publ. Astr. Soc.*, Japan, Vol. 13, p. 184, 1961.
12. Cline, T. L., G. H. Ludwig and F. B. Donald, *Phys. Rev. Lett.*, Vol. 13, p. 786, 1964.
13. Rozenthal', I. L., *Astron. Zh.* Vol. 43, p. 332, 1966.
14. Rozenthal', I. L., *Izv. An SSSR Ser. Fiz.*, Vol. 30, No. 11, 1966.
15. Siton, M., In the collected works, *Atomnyye i Molekulyarnyye Protsessy*, [Atomic and Molecular Processes], *Mir Press*, Moscow, 1964.
16. Bates, D., M. McDowell and A. Omholt, *J. Atmos. and Terr. Phys.*, Vol. 10, p. 15, 1957.
17. Fayt, V., In the collected works, *Atomnyye i Molekulyarnyye Protsessy*, [Atomic and Molecular Processes], *Mir Press*, Moscow, 1964.
18. Moysevich, V., In the collected works, *Atomnyye i Molekulyarnyye Protsessy*, [Atomic and Molecular Processes], *Mir Press*, Moscow, 1964.
19. Kaplan, S. A. and S. B. Pikel'ner, In the collected works, *Mezhzvezdnaya Sreda*, [The Interstellar Medium], *Fizmatgiz Press*, Moscow, 1963.
20. Zatsepin, V. I. and A. Ye. Chudakov, *Zh. Eksperim. i Teor. Fiz.*, Vol. 42, p. 1622, 1962.
21. Belyeyev, V. A. and A. Ye. Chudakov, *Isv. An SSSR Ser. Fiz.*, Vol. 30, No. 10, 1966.
22. Rozenthal', I. L. and M. L. Ful'chenkov, *Izv. AN SSSR Ser. Fiz.*, Vol. 30, No. 10, 1966.
23. Jelley, J. W. et al, *Nature*, Vol. 205, p. 327, 1965.
24. Askarayan, G. A., *Zh. Eksperim. i Teor. Fiz.*, Vol. 41, p. 616, 1961.
25. Tamm, I. Ye. and S. Z. Belen'kiy, *J. Phys. USSR*, Vol. 1, p. 177, 1939.
26. Akhiezer, A. I. and V. B. Berestetskiy, *Kvantovaya Elektrodinamika*, [Quantum Electrodynamics], *Fizmatgiz Press*, Moscow, 1959.

THE ENERGY SPECTRUM OF COSMIC MUONS OF ULTRAHIGH ENERGIES AT SEA LEVEL

V. V. Borog, V. G. Kirillov-Ugryumov,
A. A. Petrukhin and V. V. Shestakov

ABSTRACT. This article is devoted to consideration of the energy spectrum in relation to the problem of cosmic muon origin. A comparison of the spectra measured in vertical and horizontal directions at sea level in the energy range of $\geq 10^{11}$ ev is carried out. The article also compares the energy spectra measured at different zenith angles in order to clarify the generation mechanism of ultrahigh energy muons.

1. Introduction

The energy spectrum of particles is one of the fundamental characteristics of cosmic radiation. Interest in the study of the energy spectrum of muons is determined by two main reasons. First, the use of cosmic rays at sea level as a muon source to study their interactions requires information about the energy spectrum. Secondly, comparison of energy spectrums measured at different zenith angles makes it possible to ascertain the generation mechanism of ultrahigh energy muons. /19

This article is devoted to consideration of the energy spectrum in connection with the problem of cosmic muon origin. Comparison of spectra measured in vertical and horizontal directions at sea level in the energy range of $\geq 10^{11}$ electron volts is conducted in order to do this.

An analysis is carried out below of studies of the energy spectrum of muons in vertical and horizontal directions.

2. Studies of the Energy Spectrum of the Vertical Flux in Magnetic Spectrometers

Three papers are presently known on the measurement of the energy spectrum of muons in the range of 10^{11} - 10^{12} ev in magnetic spectrometers which were carried out in England--at Manchester, Durham and Nottingham Universities [1, 3, 4]. The results of these studies are presented in Figure 1. Actually only in

two papers [1, 3], which were completed approximately at the same time, was the energy spectrum measured to $E_\mu \approx 10^{12}$ ev. However, the spectra obtained diverge quite strongly at energies greater than 2.5×10^{11} ev. Let us analyze in more detail the accuracy with which the data in these papers were obtained.

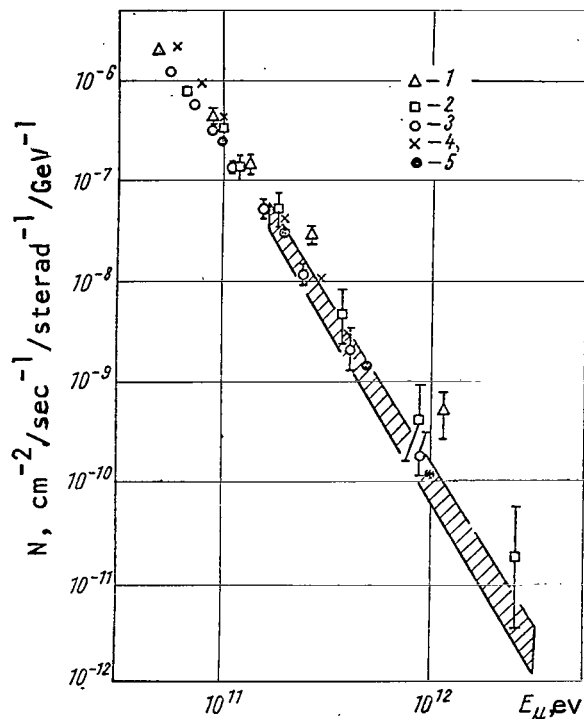


Figure 1. The Differential Energy Spectrum of Vertical Flux: 1, Data of the Manchester group [1]; 2, Preliminary data of the Durham group [2]; 3, Final data of the Durham group [3]; 4, Data of the Nottingham group [4]; 5, Data of the last analysis of the results of studying the vertical spectrum conducted by the Wolfendale group [5]. The shaded area represents the results of paper [36] where $I_{ov} = (1.0 \pm 0.25) \times 10^{-5} \text{ cm}^{-2}/\text{sec}^{-1}/\text{sterad}^{-1}$ and $\gamma_v = 2.4 \pm 0.2$.

The parameters of the magnetic spectrometers used at Manchester and Durham /20 are almost identical. The relation of the article pulse P with the deviation of its trajectory in a magnetic field Δ is given by almost identical formulas:

$$P\left(\frac{\text{GeV}}{c}\right) = \frac{368 \pm 2}{\Delta (\text{MM})} \quad (\text{Manchester});$$

$$P\left(\frac{\text{GeV}}{c}\right) = \frac{333,1 \pm 0,6}{\Delta (\text{MM})} \quad (\text{Durham}).$$

However, the accuracy of measuring the value of Δ differs substantially.

The Manchester group used a Wilson cloud chamber as a detector. The accuracy of measuring Δ was determined by the configuration of the photography and depended on the location of particle transit. Table 1 presents the errors in determining Δ and the corresponding maximum measured pulse as P_{\max} (according to the data of paper [1]).

/21

Table 1

Location of Transit	Error in Measurement of Δ , mm	P_{\max} , GeV/c
Center of spectrometer	0.25	1000
Edge of spectrometer	1.4	190
Middle position	0.9	300
70% of all trajectories	0.6/1.2	450/220

It is obvious from the table that particle pulses only up to 200 GeV/c can be measured on the Manchester spectrometer without introducing corrections. Measurements of pulses greater than 200 GeV/c require introduction of corrections for the transmission variation of the apparatus. Such an operation leads to a very great ambiguity in the case of low statistics. According to the data of [1], the statistics are the following: 25 particles with an average pulse of 270 GeV/c and four particles with an average pulse of 1160 GeV/c.

The Durham spectrometer used neon flash tubes as detectors which reduce ambiguities related to photography to zero, because only the number of the flash tube is determined by photography, and its position is known to the required accuracy. A large number of flash tubes intersected by a particle make it possible to determine the trajectory rather accurately. The authors note [3]: "...graphic analysis indicates that the mean square error in locating the particle track is equal to 0.20 mm for neon flash tubes with 100%-efficiency". This corresponds to $P_{\max} = 1650$ GeV/c. However, less than 100%-efficiency of the neon flash tubes and initial firings from δ -electrons decrease P_{\max} to 657 GeV/c. In this spectrometer P_{\max} does not depend on the location of particle transit.

The latest research and measurement of the vertical energy spectrum was carried out at Nottingham [4]. Neon flash tubes were also used in a magnetic spectrometer. The energy spectrum was measured to $4 \cdot 10^{11}$ ev. The results agree well with the data obtained at Durham, although they are somewhat higher in absolute value (Figure 1). Thus, the analysis conducted indicates that the data of the Durham group is more reliable in the energy range $> 2 \cdot 10^{11}$ ev than that of the Manchester group. The spectrum obtained at Nottingham agrees within the limits of errors with the spectrum obtained at Durham.

In order to obtain the quantitative characteristics of the spectrum, let us assume that the integral and differential muon spectra may be expressed by the step functions

/22

$$I(\geq E_\mu) = I_0 E_\mu^{-\gamma}; \quad N(E_\mu) = \gamma \cdot I_0 \cdot E_\mu^{-(\gamma+1)}. \quad (1)$$

In order to determine the value of γ_V to which the vertical spectrum obtained in magnetic spectrometers corresponds, let us present the available data in a graph with coordinates E_μ and $N(E_\mu)E_\mu^{\gamma_V+1}$. If the slope of the spectrum corresponds to γ_V , then the experimental points should lie on a straight line parallel to the axis of the abscissae. If the slope of the spectrum is steeper, the points will deviate downward, and if it is more inclined, they will deviate upward. The experimental data are compared in Figure 2 with four values of γ_V . It is obvious from the diagram that for $E_\mu > 10^{11}$ ev the spectrum obtained at Durham agrees more closely with $\gamma_V = 2.2$, the spectrum obtained at Nottingham--with $\gamma_V = 2.4$, and that at Manchester corresponds to $\gamma_V = 1.8$. Taking into consideration the evaluation of authenticity of different spectra obtained above, we can conclude that the most reliable value $\gamma_V = 2.3 \pm 0.1$.

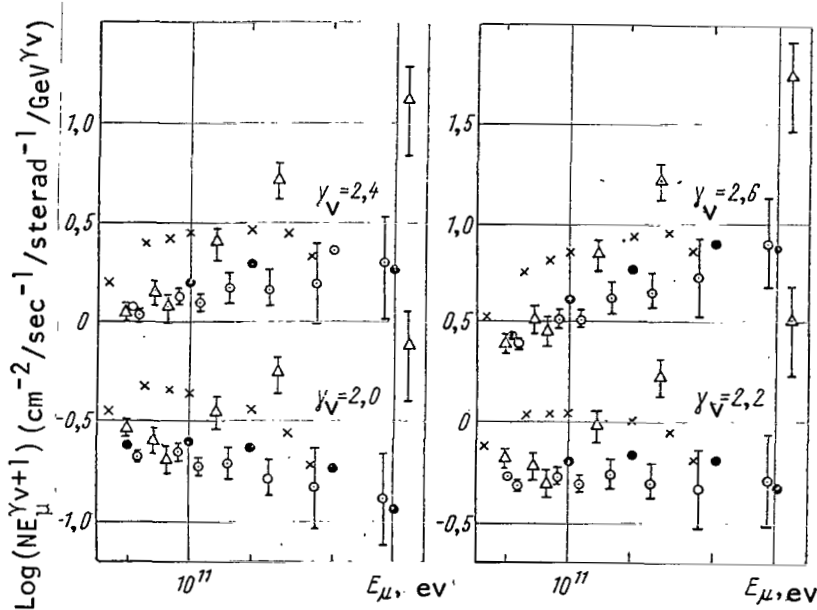


Figure 2. The Differential Energy Spectrum at Coordinates E_μ and $N(E_\mu) \cdot E_\mu^{\gamma_V+1}$. The notations are the same as in Figure 1.

3. Studies of the Energy Spectrum of Vertical Flux by Indirect Methods

The magnetic method of measuring the energy spectrum is presently limited by an energy range of the order of 10^{12} ev. Therefore, different indirect methods are used for higher energies--investigations of electromagnetic muon

interactions with subsequent conversion into the spectrum of muons; measurement of the muon absorption curve in the ground with subsequent reduction of the energy spectrum and study of the photon spectrum at high altitudes in the atmosphere which are genetically related to the spectrum of muons. All these methods make it possible to analyze the spectrum of muons to energies of $\sim 10^{13}$ ev, but definite disadvantages are inherent in all of them which cause a large ambiguity in the energy spectrum of muons.

In principle, the greatest accuracy may be attained in the first method, because well-known cross-sections of electromagnetic processes are used to obtain the energy spectrum of muons. However, the widely prevalent method of ionization bursts based on recording an electromagnetic shower at a single point had at least two disadvantages--first, the energy converted in the electromagnetic interaction is not known, and secondly, as a rule, the direction of the muon caused by the showers is not known, which makes it necessary to calculate the angular distribution of cosmic muons and the probability of recording showers of different energies dependent of the angle.

The basic uncertainty in the method of reducing the energy spectrum from the absorption curve is related to the unknown composition of the ground during measurement at great depths. Moreover, there are at present no accurate values of the integral losses of superhigh energy muons [6] and calculation of the fluctuation and energy losses is accordingly made difficult. There were no experimental data until recently on the angular distribution of superhigh energy muons, which also introduced a certain indeterminacy.

Investigation of γ -ray photons in the upper layers of the atmosphere also does not yield an unambiguous value of the energy spectrum of muons. In addition to the difficulties connected to conducting the experiment at high altitudes, a large ambiguity occurs during conversion into the muon spectrum. Such a conversion requires definite assumptions about the mechanisms of muon and γ -ray photon generation at superhigh energies and, most important, about the relationship of these mechanisms.

Much research has been completed on the study of the muon spectrum by all three methods. It is not possible here to analyze all the research in this field. Let us therefore consider only the fundamental research (Figure 3). It is obvious from the diagram that the results of different research in the energy range up to 10^{12} ev more or less agree in absolute intensity, although the slopes of the spectra are different (γ_v varies from 2.0 [8] to 2.8 [10]). The data diverge even more strongly in the energy range 10^{12} ev.

These maximum values of γ_v are hardly probable in the energy range of interest to us. The most probable values of γ_v in the two papers on investigation of ionization bursts [12] and [13] were equal to 2.4 and 2.5 respectively. The data of the remaining papers are given in Figure 4 in coordinates E_μ and $I(E_\mu) \cdot E_\mu^{2.4}$. The results of underground experiments [9] in the energy range up to $2 \cdot 10^{12}$ ev agree well with $\gamma_v = 2.4$ (see Figure 4). The data obtained from

/24

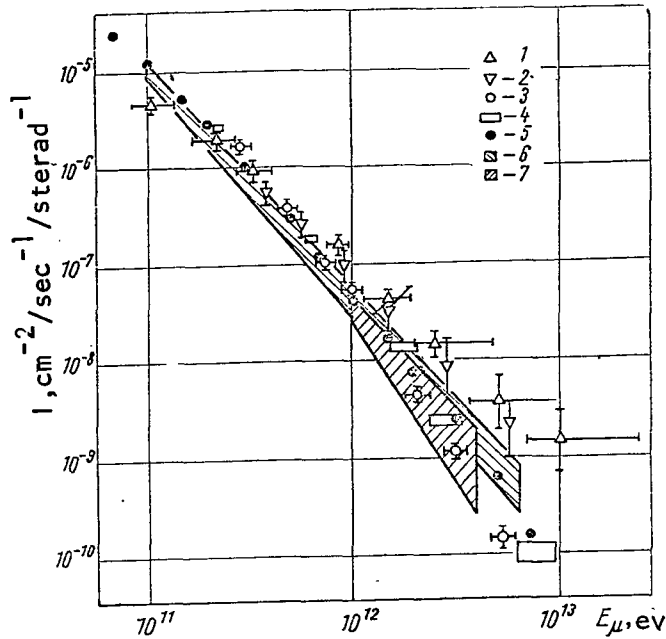


Figure 3. The Integral Energy Spectrum of Vertical Flux: 1, Data according to bursts (NIIYaF) [7]; 2, Data according to bursts (NIIYaF) [8]; 3, Data according to absorption (India) [9]; 4, Data according to the spectrum of γ -ray photons (Bristol) [10]; 5, Analysis data of the Wolfendale group [11]; 6, Data according to bursts (Krasil'nikov) [12]; 7, Data according to bursts (Japan) [13].

investigation of the γ -ray photon spectrum [10], which were published by the authors in 1962, most strongly contradict the index of $\gamma_v = 2.4$ in this energy range. There have since been no reports on new calculations of the muon energy spectrum in this group. However, the results of their further experiments [14, 15] indicates that γ_v decreases. /25

Besides the papers considered, there are still several similar investigations conducted at various altitudes using a different technique [16, 17, 18]. As has been noted already, the energy spectrum of muons depends not only on the γ -ray photon spectrum, but also on the models of the nuclear interactions taken into account. Thus, the calculated muon spectrum in paper [16] agreed very well with data obtained at Durham on the magnetic spectrometer, which also agree with $\gamma_v = 2.3$ as indicated above. The most complete analysis of all available experiments on the investigation of the energy spectra of γ -ray photons at different altitudes was carried out in [19]. The energy spectrum of muons was calculated on two hypothesis of the production channels of π^0 -mesons, responsible for generation of γ -photons in the atmosphere: 1) directly in nuclear interactions and 2) as a result of K-meson decay. The spectra obtained are presented in Figure 5. During direct production of π^0 -mesons $\gamma_v =$ /26

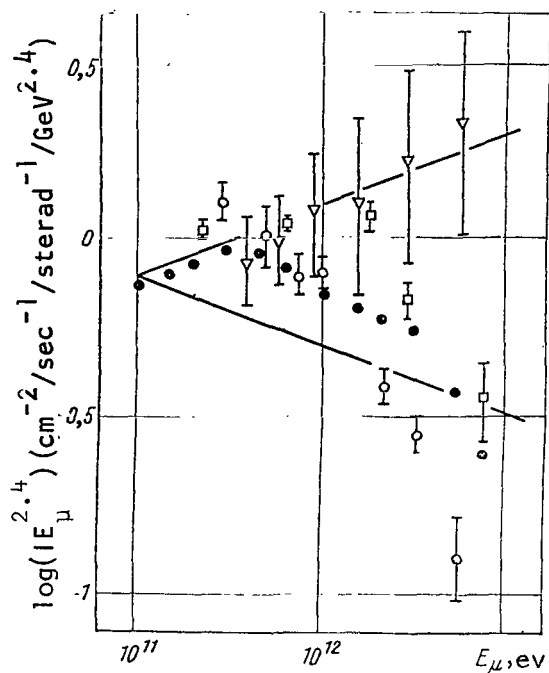


Figure 4. The Integral Energy Spectrum at Coordinates E_μ and $IE_\mu^{2.4}$. The notations are the same as in Figure 3. The straight lines correspond to $\gamma_V = 2.2$ and 2.6 .

Thus, analysis of available data on the study of the integral energy spectrum of muons indicates a more probable value of $\gamma_V = 2.4 \pm 0.2$ at least to energies of $\sim 2 \cdot 10^{12}$ ev.

The value of $\gamma_V = 2.4$ differs somewhat from $\gamma_V = 2.3$ obtained during analysis of the data of magnetic measurements. Although this difference is negligible, it does have an explanation. We assumed that the muon spectrum may be described by a step function with a constant index (1). The relation $\gamma_{\text{dif}} - \gamma_{\text{integr}} = 1$ is valid in this case. However, analysis of the muon energy spectrum over a wide energy range indicates that the index of γ increases as energy increases. In this case $\gamma_{\text{dif}} - \gamma_{\text{integr}} < 1$.

$= 2.6$, and $\gamma_V = 2.2$ when there is 100%-generation of π^0 -mesons via K-mesons. Experiments on the study of cosmic muon polarization yield an estimate of $(40 \pm 20)\%$ for fractions of K-mesons. If this value does not vary substantially as energy increases, then $\gamma_V = 2.4$ - 2.5 . If no assumptions are made about the ratio of π - and K-mesons, then $\gamma_V = 2.4 \pm 0.2$.

Two comments may be made about papers [7] and [8]--first, the burst spectrum was measured in them over a wide range of zenith angles and was not recalculated to the vertical spectrum of muons; secondly, even the data presented within the ranges of experimental errors do not contradict the muon spectrum with $\gamma_V = 2.4$ (see Figure 3).

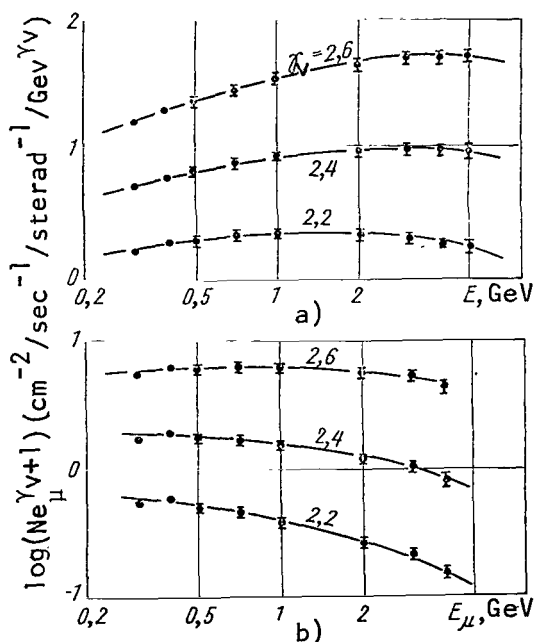


Figure 5. The Energy Spectra of Muons Obtained from Photon Spectra at High Altitudes: During formation of π^0 -Mesons as a Result of K-Meson Decay (a) and During Direct Production of π^0 -Mesons in Nuclear Interactions (b).

Thus, if the energy spectrum in a vertical direction may be described by a step function, the constants in formula (1) for $10^{11} \lesssim E_\mu \lesssim 2 \cdot 10^{12}$ ev will be the following: $I_{ov} = (1.2 \pm 0.2) \cdot 10^{-5} \text{ cm}^{-2}/\text{sec}^{-1}/\text{sterad}^{-1}$ and $\gamma_v = 2.4 \pm 0.1$. Moreover, E_μ in formula (1) is measured in units of 10^{11} ev. The values of the index of γ_v and absolute intensity I_{ov} were determined from the aggregate of all the papers considered.

4. The Energy Spectrum of Cosmic Muons at Large Zenith Angles

Until recently the vertical muon flux was mainly studied, because the horizontal flux is approximately 1,000 times less than the vertical. Intensity measurements of the horizontal flux carried out in papers [20, 21] yielded the following values: $2.4 \cdot 10^{-5} \text{ cm}^{-2}/\text{sec}^{-1}/\text{sterad}^{-1}$ for a north-south direction and $1.9 \cdot 10^{-5} \text{ cm}^{-2}/\text{sec}^{-1}/\text{sterad}^{-1}$ for an east-west direction. (The intensity of the vertical flux is of the order of $10^{-2} \text{ cm}^{-2}/\text{sec}^{-1}/\text{sterad}^{-1}$.)

Several papers have been completed in recent years on the measurement of the energy spectra of muons at large zenith angles ($\theta \gtrsim 60^\circ$). Table 2 presents a summary of available experimental data on the study of muon fluxes with energies to 10^{11} ev at different zenith angles.

Table 2

Year	Zenith Angle, deg	Energy range, GeV	Reference
1954	30 and 60	0,3÷60	[22]
1961	68	2÷70	[23]
1961	65÷85	1÷100	[24]
1963	80	1,5÷40	[25]
1963	77,5÷90	5÷100	[26]
1965	30, 45 and 60	0,7÷50	[27]
1965	86,5	1÷30	[27]

Analysis of the results of the renumerated experiments confirmed the expected increase of the fraction of high energy muons as the zenith angle increases. The characteristics of energy spectra change (to 10^{11} ev) depending on the zenith angle agree with the hypothesis of muon generation as a result of $\pi \rightarrow \mu$ -decay. /28

Several theoretical papers were completed during this time, devoted to calculation of the energy spectra of superhigh energy muons at different zenith angles. The generation of muons in the atmosphere as a result of π -meson decay was first studied by Barrett, et al in 1952 [28]. They obtained an analytical expression for the energy and angular dependence of muon flux at different zenith angles on the assumption of a plane atmosphere. In 1956 Jakeman [20] calculated the energy spectrum in the range of $10^9 - 10^{13}$ ev for $\theta = 90^\circ$, using the hypothesis of $\pi \rightarrow \mu$ -decay.

The most complete calculation of angular distributions of muons of different energies was conducted in 1960 by G. T. Zatsepin and V. A. Kuz'min [29] for muon energies of 10^{11} - 10^{14} ev over the entire range of zenith angles for two generation mechanisms (π - and K-decay). They were the first to show that the greatest difference between these two generation mechanisms is observed in the energy range of 10^{11} - 10^{12} ev.

In 1961 Allen and Apostolakis [24] calculated the energy spectra in the range of 10^9 - 10^{12} ev for different angles within the range of 60° - 90° . They were the first to consider the effect of scattering for energies less than 10^{11} ev, which causes a substantial increase of the low-energy muon flux at large zenith angles.

The latter paper on calculation of the angular distribution of ultrahigh energy muons was completed by Maeda in 1964 [30]. Actually, he repeated the calculations of G. T. Zatsepin and V. A. Kuz'min, reducing the lower energy limit to $4 \cdot 10^{10}$ ev. Moreover, he carried out calculations for other depths of the atmosphere--750 g/cm² and 500 g/cm² (the height of mountains). Maeda's calculations confirmed the conclusion made in paper [29] that the greatest difference of the two mechanisms of muon generation is observed in the range of 10^{11} - 10^{12} ev. However, although the curves obtained by him are close to those of paper [29], the difference of angular distributions of the two generation mechanisms was somewhat less.

The first paper on the experimental study of muons with energies greater than 10^{11} ev at large zenith angles was conducted by F. R. Arutyunyan, et al [31]. They investigated the transitional interference of muon emission of the horizontal flux of cosmic rays in the energy range of $7 \cdot 10^{11}$ - $6 \cdot 10^{12}$ ev. The experiment was conducted at an altitude of 1000 meters above sea level. The authors reported 77 events which were interpreted as the result of the interference emission of muons. The spectrum of the muons in the range of $7 \cdot 10^{11}$ - $6 \cdot 10^{12}$ ev was estimated on the basis of the calculated efficiency of recording muons of different energies. We should refer to the spectrum obtained rather carefully, because the physical phenomenon, with whose fault it was measured was observed for the first time by the authors. Their results should rather be taken as the experimental discovery of interference emission, confirmation of the existence of which is the agreement of the number of events recorded with that calculated from the anticipated spectrum of the horizontal flux, on the basis of the hypothesis of $\pi \rightarrow \mu$ -decay. This is just how the authors interpreted the results in their first report [32].

/29

Two papers devoted to the study of the energy spectrum of muons at large zenith angles were heard in 1965 at the IX International Conference on Cosmic Rays in London. In the first paper [33] completed by the authors of this article, the energy spectrum of muons was studied by cascade showers recorded with the help of an ionization calorimeter [34]. In this paper, the cascade showers were recorded at three points, which made it possible to make a reliable determination of their energy. Sampling of the showers according to the projection of the zenith angle excluded the ambiguity related to the angular distribution of muons. The energy spectrum of cascade showers was

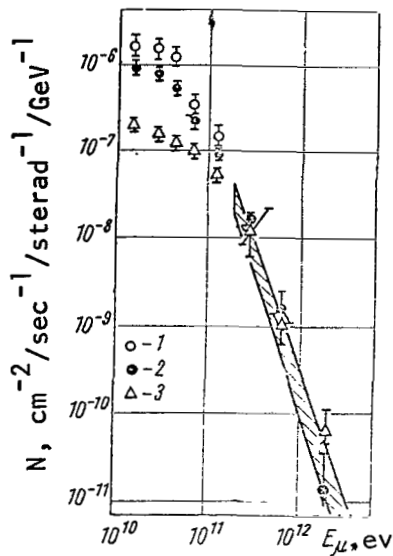


Figure 6. The Differential Energy Spectrum of Cosmic Muons at Large Zenith Angles. The experimental points from paper [35] are: 1, range of angles 82.5-85°; 2, range of angles 85-87.5°; 3, range of angles 87.5-90°. The shaded area depicts the results of paper [33].

recalculated into the muon spectrum. The value of index γ_h of the horizontal spectrum in formula (1) for a range of zenith angles of 55-90° was equal to 2.1 ± 0.15 , if we consider the muon flux to be isotropic, and 2.0 ± 0.15 , if we take into consideration the angular distribution of muons on the basis of the hypothesis of π - or K-decay (energy range of $2 \cdot 10^{11}$ - $3 \cdot 10^{12}$ ev).

The second paper [35] was completed by the group at Durham University on a magnetic spectrometer. The energy spectrum in this paper was measured for three ranges of angles--82.5-85, 85-87.5 and 87.5-90° in the energy range of 10^{10} - 10^{12} ev. Figure 6 presents the results of both papers. It is obvious from the diagram that the papers agree quite well within the limits of experiment errors.

/30

5. Angular Distribution and the Generation Mechanism of Cosmic Muons

We shall use the results of paper [33], in which the statistics are substantially greater than in [35], to calculate the angular distribution. (For $E_\mu \geq 5 \cdot 10^{11}$ by 15 times).

In a general case the differential energy spectrum at an angle of θ may be written in the form

$$N(\theta, E_\mu) = N_v(E_\mu) \cdot p(\theta, E_\mu), \quad (2)$$

where $N_v(E_\mu)$ is the spectrum along the vertical, and $p(\theta, E_\mu)$ is the function of angular distribution dependent on the generation mechanism.

Setting the function $p(\theta, E_\mu)$, we can convert from $N(\theta, E_\mu)$ to $N_v(E_\mu)$.

Such a conversion was made in paper [36] for three possible generation mechanisms-- $\pi \rightarrow \mu$ -decay, $K \rightarrow \mu$ -decay and the direct generation of muons in nuclear interactions. In the latter case $p(\theta, E_\mu) = 1$ [37]. The values of the function of $p(\theta, E_\mu)$ for the cases of $\pi \rightarrow \mu$ and $K \rightarrow \mu$ -decays were taken from paper [29]. The energy dependence $N_v(E_\mu)$ was taken in the form of (1). Closest agreement with experimental data in the energy range of $2 \cdot 10^{11}$ - $3 \cdot 10^{12}$ ev was obtained:

1) for direct generation--when $\gamma_v = 2.1 \pm 0.15$;

2) for $\pi \rightarrow \mu$ -decay--when $\gamma_v = 2.35 \pm 0.15$;

3) for $K \rightarrow \mu$ -decay--when $\gamma_v = 2.4 \pm 0.15$.

The conversion result for cases of π - and K -decays is given in Figure 1.

Comparing the values obtained with the index of the vertical spectrum $\gamma_v = 2.4 \pm 0.1$ (see Section 2), we can conclude that the angular distribution of ultrahigh energy cosmic muons agrees well with that anticipated of the decay processes of π - and K -mesons and does not agree with the isotropy which occurs as a result of direct muon generation and nuclear interactions.

Not all the experiments in the study of the vertical spectrum are equivalent for the conclusion obtained. In the experiments on bursts, the muons propagate as a rule over a wide range of zenith angles; therefore, the angular distribution must be set when converting to the vertical spectrum. Thus, theoretical angular distributions from $\pi \rightarrow \mu$ -decay were used in papers [12] and [13] when calculating the vertical spectrum. Therefore, determination of the mechanism of muon generation would logically be contradictory only on the basis of these experiments. A similar situation occurs when converting the γ -ray photon spectrum to the muon spectrum. The interaction model is also first selected here, and then the muon spectrum is calculated. /31

Actually, the conclusion made is based only on two types of experiments--magnetic measurement and investigations of the absorption curve in the ground, although the latter are also dependent on the angular distribution of muons. This dependence makes it possible to verify the conclusion obtained. The data of [9] and [38] which differ most from each other are described satisfactorily by the vertical spectrum with $\gamma_v = 2.4$ and by an angular muon distribution from π - and K -decays. The results of these papers agree with those for $\gamma_v = 2.6$ and 2.0 , respectively for isotropic angular distribution.

Let us in conclusion dwell on the results of paper [39]. The authors studied muon showers at zenith angles of $\theta > 75^\circ$ in order to study extensive air showers on the apparatus. Because the apparatus was not designed to study these events, a certain ambiguity of the results obtained was determined by two features--separation of the muon showers and estimation of the zenith angle. The authors processed their experimental results by two different methods and obtained $\gamma_h = 1.75$ (I method of processing) and $\gamma_h = 2.0$ (II method of processing) for an energy spectrum in the range of angles $75-90^\circ$ when $E_\mu \gtrsim 10^{11}$ ev. Assuming that, on the average $\gamma_h = 1.8-1.9$, we reach the conclusion that the results of this paper are also in agreement with the data of [33] and [35], because the energy spectrum becomes more sloping as the zenith angle increases. The latter assertion was confirmed experimentally in paper [35] (See Figure 6).

Thus, the basic conclusion which can be made from analysis of the data on the study of the energy spectrum of vertical and horizontal muon fluxes consists of the fact that ultrahigh energy cosmic muons (at least to $2 \cdot 10^{12}$ ev) are generated mainly during the decay processes of π - and K -mesons. The portion of direct muon generation and nuclear interactions cannot be great.

REFERENCES

1. Holmes, J. E. R., B. G. Owen and A. L. Rodgers, *Proc. Phys. Soc.*, Vol. 78, p. 505, 1961.
2. Ashton, F. et al, *Nature*, Vol. 185, p. 364, 1960.
3. Hayman, P. J. and A. W. Wolfendale, *Proc. Phys. Soc.*, Vol. 80, p. 710, 1962.
4. Bull, R. M., W. F. Nash and B. C. Rastin, *Nuovo cimento*, Vol. 40, p. 365, 1965.
5. Osborne, J. L., S. S. Said and A. W. Wolfendale, *Proc. Phys. Soc.*, Vol. 86, p. 93, 1965.
6. Hayman, P. J., N. S. Palmer and A. W. Wolfendale, *Proc. Roy. Soc.*, Vol. A275, p. 391, 1963.
7. Dmitriyev, V. A. and G. P. Khristiansen, *Zh. Eksperim. i Teor. Fiz.*, Vol. 44, p. 405, 1963.
8. Vernov, S. N. et al, *Proc. IX Internat. Conf. on Cosmic Rays*, London, Vol. 2, p. 952, 1965.
9. Miyake, S. et al, *Nuovo cimento*, Vol. 32, pp. 1505-1524, 1964.
10. Duthie, J. et al, *Nuovo cimento*, Vol. 24, p. 122, 1962.
11. Osborne, J. L. et al, *Proc. Phys. Soc.*, Vol. 84, p. 911, 1964.
12. Krasil'nikov, D. D., *Izv. AN SSSR. Ser. Fiz.*, Vol. 28, p. 1854, 1964.
13. Higashi, S. et al, *Nuovo cimento*, Vol. 32, p. 1, 1964.
14. Fowler, P. H., *Proc. VIII Internat. Conf. on Cosmic Rays*, Jaipur, Vol. 5, p. 182, 1963.
15. Boulton, J. et al, *Nuovo cimento*, Vol. 40, p. 385, 1965.
16. Baradzey, L. T. et al, From the collected works, *Kosmicheskiye Luchi* [Cosmic Rays], Issue 26, p. 224, *FIAM im. P. N. Lebedev*, p. 224, 1964.
17. Fuimoto, Y., *Proc. VIII Internat. Conf. on Cosmic Rays*, Jaipur, Vol. 5, p. 326, 1963.
18. Kidd, J. M., *Nuovo cimento*, Vol. 27, p. 57, 1963.
19. Osborne, J. L. and A. W. Wolfendale, *Proc. Fiz. Soc.*, Vol. 84, p. 901, 1964.
20. Jakeman, D., *Canad. J. Phys.*, Vol. 34, p. 432, 1956.
21. Wilson, B. G., *Canad. J. Phys.*, Vol. 37, p. 19, 1959.
22. Moroney, J. R. and J. K. Parry, *Austral. J. Phys.*, Vol. 7, p. 423, 1954.
23. Pak, W. et al, *Phys. Rev.*, Vol. 121, p. 905, 1961.
24. Allen, J. E. and A. J. Apostolakis, *Proc. Roy. Soc.*, Vol. 265, p. 117, 1961.
25. Ashton, F. and A. W. Wolfendale, *Proc. Phys. Soc.*, Vol. 81, p. 593, 1963.
26. Ashton, F. et al, *Proc. VIII Internat. Conf. on Cosmic Rays*, Jaipur, Vol. 6, p. 72, 1963.
27. Judge, H. J. R. and W. F. Nash, *Nuovo cimento*, Vol. 35, pp. 999, 1025, 1965.
28. Barrett, P. H. et al, *Rev. Mod. Phys.*, Vol. 24, p. 133, 1952.
29. Zatsepin, G. T. and V. A. Kuz'min, *Zh. Eksperim. i Teor. Fiz.*, Vol. 39, p. 1677, 1960.
30. Maeda, K. J., *Geophys. Res.*, Vol. 69, p. 1725, 1964.
31. Arutyunyan, F. R., K. A. Raspiryan and A. G. Oganessian, *Izv. AN SSSR. Ser. Fiz.*, Vol. 29, p. 1769, 1965.
32. Arutyunyan, F. R., K. A. Raspiryan and A. G. Oganessian, *Izv. AN SSSR. Ser. Fiz.*, Vol. 28, p. 1864, 1964.

33. Borog, V. V. et al, *Proc. IX Internat. Conf. on Cosmic Rays*, London, Vol. 2, p. 962, 1965.
34. Borog, V. V. et al, In the collection, *Fizika Elementarnykh Chastits*, [Physics of Elementary Particles], Atomizdat Press, Moscow, Vol. 59, 1966.
35. MacKeown, P. K. et al, *Proc. IX Internat. Conf. on Cosmic Rays*, London, Vol. 2, p. 964, 1965.
36. Borog, V. V. et al, *Yadernaya Fizika*, Vol. 3, p. 783, 1966.
37. Alekseyev, I. S. and G. T. Zatespin, *Trudy VI Mezhdunarodnoy Konferentsii Po Kosmoscheskim*, [Proceedings of the VI International Conference on Cosmic Rays], Vol. 1, p. 326, AN SSSR Press, Moscow, 1960.
38. Payn, Zh., R. Zh. Devisson and K. B. Greyzen, *Trudy VI Mezhdunarodnoy Konferentsii Po Kosmoscheskim*, [Proceedings of the VI International Conference on Cosmic Rays], Vol.1, p. 293, AN SSSR Press, Moscow, 1960.
39. Goryunov, N. N. and G. T. Zatespin, *Zh. Eksperim. i Teor. Fiz.*, Vol. 39, p. 271, 1960.

ELASTIC π^+ -p-SCATTERING AT A π^+ -MESON ENERGY AT 2.06 GeV

S. P. Kruchinin and K. N. Mukhin

ABSTRACT. This article investigates elastic π^+ -p-p-scattering at a π^+ -meson energy of 2.06 GeV. The paper compares results of previous papers which measured the differential cross-sections of elastic π^+ -p-scattering at pulses of 2.0 and 2.5 GeV/c over a range of angles $\theta < 20^\circ$. This paper presents the differential cross-section of elastic scattering of π^+ -mesons with an energy of 2.06 GeV in protons over the entire range of angles. The deduction method was used to obtain the cross-section in the range of angles $\theta < 20^\circ$.

1. Introduction

Experimental data on elastic π^+ -p-p-scattering (jointly) over the entire range of angles was previously [1] obtained with a sufficiently high degree of accuracy from material of experimental irradiation of a propane bubble chamber with a pulse magnetic field [2] by a mixed beam of positively charged particles (π^+ was 47%, p was 47.5%, K^+ was 3%, and μ^+ was 2.5%) with a pulse of 2.2 GeV/c. Use of the kinematic criterion made it possible to separate proton and ion scattering for scattering angles in a laboratory system of axes $\theta > 20^\circ$. Kinematic separation of π -p- and p-p-events is not possible at $\theta < 20^\circ$. Therefore, additional independent information on the process of the differential cross-section of π^+ -p- or p-p-scattering at $\theta < 20^\circ$ is required in order to obtain $\sigma_{\pi^+p}(\theta)$ or $\sigma_{pp}(\theta)$ in this range of angles.

When paper [1] was completed in 1963-1964, the only source of additional information (of an indirect character besides) was the paper of Cook et al [3], in which the differential cross-sections of elastic π^+ -p-scattering were measured at pulses of 2.0 and 2.5 GeV/c. Because the range of angles of $\theta < 20^\circ$ lies almost entirely in the zone of diffraction scattering, both cross-sections behave identically at lower $\theta < 20^\circ$. In this regard the results of paper [3] in the range of angles $\theta < 20^\circ$ may be reliably interpolated for intermediate values of the pulses. Such interpolation was carried out in paper [1] for a pulse of 2.2 GeV/c. This interpolation made it possible to obtain the missing data on $\sigma_{\pi^+p}(\theta)$ in the range of angles $\theta < 20^\circ$ and to isolate the differential cross-section of elastic p-p-scattering at energy of 1.45 GeV using the deduction method.

Moreover, in order to verify the deduction method in the range of angles $20^\circ < \theta < 30^\circ$ a comparison was made of the results obtained by this method and by separation by the kinematic criterion. The comparison showed good agreement of both methods (the number of protons counted in the indicated range of angles by each method was equal to 66 and 64, respectively; the value obtained by the deduction method was presented in [1]). Thus, the differential cross-section of elastic p-p-scattering over the entire range of angles was obtained. /34

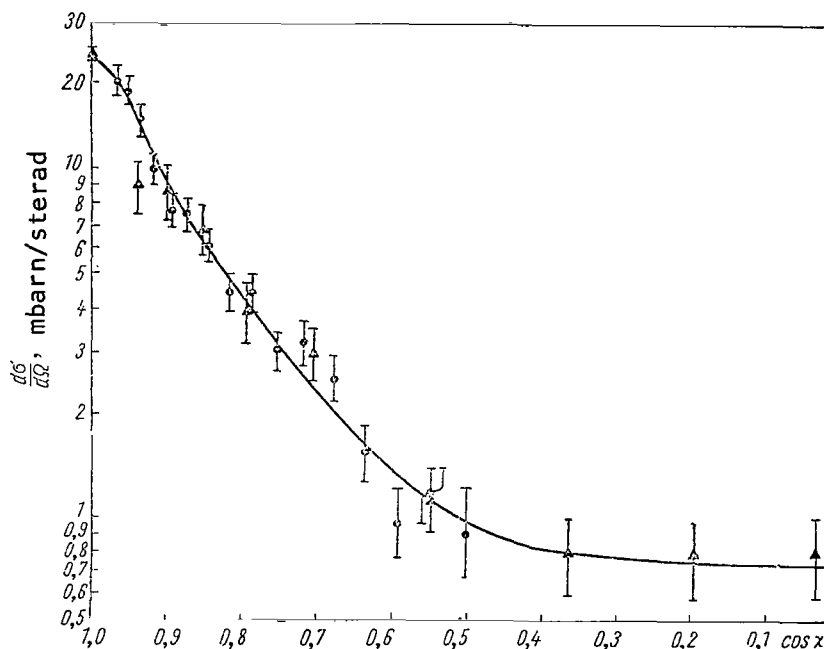


Figure 1.

It has now become possible to compare the results of [1] with the measurements of the cross-section of elastic p-p-scattering carried out by Eisner et al [4] for protons with a near energy of $T = 1.48$ GeV. Paper [4] presents the curve of the differential cross-section over the range of angles $6^\circ < \theta < 23^\circ$. The close agreement of [1] and [4] displayed in the similar process of the differential cross-sections (Figure 1; the triangles are the results of [1] and the dots---[4]). The proximity of integral cross-sections ($\sigma_{pp}^{el} = 22.2 \pm 3.4$ mbarn [1] and $\sigma_{pp}^{el} = 19.86 \pm {}^{+0.73}_{-0.64}$ mbarn [4]), and also in the practical coincidence of the parameters of the optical model ($R = 0.94 \pm 0.05$, $(1 - a) = 0.85 \pm 0.09$ and $R = 0.91$ ($1 - a) = 0.864$, [1] and [4], respectively) indicates internal agreement and reliability of the deduction method used in [1]. Hence, it follows that the interpolation of the cross-section $\sigma_{\pi^+p}(\theta)$ used in [1] and [4] pulse $p = 2.2$ GeV/c in the range of angles $\theta < 20^\circ$, is close to the actual path of cross-section in this range of angles. However, as before there are no experimental data on the differential cross-

/35

sections of elastic π^+ -p-scattering over the entire range of angles at a π^+ -meson energy of $T \approx 2$ GeV. Interest in such data is presently growing continuously because of the possible relation of differential cross-section behavior with pion-nucleon resonances [5, 9] and with the development and correlation of the optical model [6, 7, 8]. The behavior of $\sigma_{\pi^+p}^{el}(\theta)$ at $T \approx 2$ GeV obtained from direct experimental data is therefore of interest.

2. Results

This article presents the differential cross-section of elastic π^+ -meson scattering with an energy of 2.06 GeV ($P_{\pi^+} = 2.2$ GeV/c) in protons over the entire range of angles. The data of [1] isolated with the help of the kinematic criterion were used for angles of $\theta > 20^\circ$. The deduction method, using (without interpolation) the results of [1] and [4], was applied to obtain the cross-section in the range of angles of $\theta < 20^\circ$. Figure 2 presents the dependence of differential cross-section $d\sigma/d\Omega$ on the co-signs of the scattering angle $\cos \chi$ (the cross-section and angle are given in the center of mass system). The experimental data are also presented in Table 1. The cross-section at an angle of 0° ($\cos \chi = 1$) was calculated as

$$\frac{d\sigma}{d\Omega}(0^\circ) = |f(0^\circ)|^2 = |\operatorname{Re} f(0^\circ)|^2 + |\operatorname{Im} f(0^\circ)|^2 = |\operatorname{Im} f(0^\circ)|^2(1 + \alpha^2), \quad (1)$$

where

$$\alpha = \frac{\operatorname{Re} f(0^\circ)}{\operatorname{Im} f(0^\circ)}.$$

The imaginary part of the forward scattering amplitude $\operatorname{Im} f(0^\circ)$ may be found by the optical theorem

$$\operatorname{Im} f(0^\circ) = \frac{k\sigma_{\text{tot}}}{4\pi}, \quad (2)$$

where k is the wave vector in the center of mass system and σ_{tot} is the total cross-section of interaction of π^+ -mesons with protons at an energy of $T = 2.06$ GeV; according to the data of [11] $\sigma_{\text{tot}} = (29.7 \pm 0.3)$ mbarn. /36

Unfortunately, there is no single experiment in the energy range of 1-3 GeV for π^+ -mesons to measure the relation of the real part of elastic scattering amplitude to the imaginary part. Therefore, the value of α for our energy range was taken from the theoretical curve of V. S. Barashenkov [10] ($\alpha = -0.28$). Substitution of the discovered values of α and σ_{tot} in two formulas (1) and (2) leads to a value of $d\sigma/d\Omega(0^\circ) = 13.2$ mbarn/sterad. The paper of H  hler et al [12] presents the value of $d\sigma/d\Omega(0^\circ)$ at an energy of 2.06 GeV equal to 12.98 mbarn/sterad, and it follows from Cronin's paper [13]

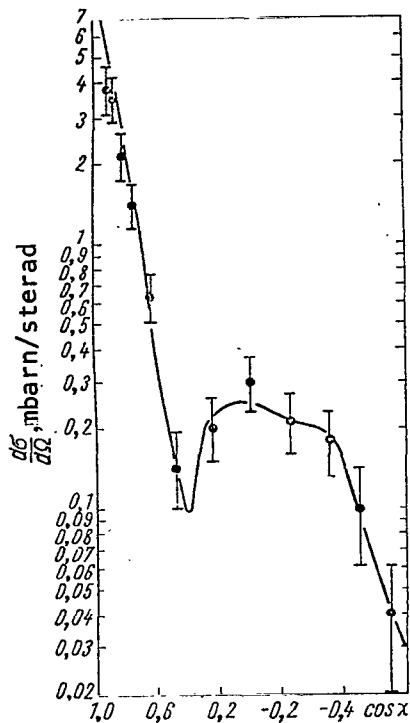


Figure 2

3. Discussion of Results

It is interesting to compare the data obtained in this paper with the results of [3]. The cross-sections behaved similarly, as was to be expected, in the range of $0.6 < \cos \chi < 1$ (the range of diffraction scattering). However, further behavior of the cross-sections differs sharply at different values of the initial pulse of impinging π^+ -mesons. A maximum is observed at $\cos \chi = -0.35$ for a pulse of 1.5 GeV/c in the differential cross-section of π^+ -p-scattering. This maximum ($\cos \chi = -0.4$) is substantially lower (1.14 and 0.35 mbarn/sterad, respectively) for a 2.0 GeV/c pulse.

that the cross-section at an angle of 0° at the same energy is equal to 13.44 mbarn/sterad. All three results are in close agreement among themselves.

The integral cross-section of elastic scattering was equal to $\sigma_{\pi^+p}^{el} = 10.0^{+1.5}_{-1.7}$ mbarn, compared with 10.6 ± 1.5 and 6.9 ± 1.0 mbarn at energies of 1.96 and 2.36 GeV, respectively.

The differential cross-section obtained was expanded into a power series of $\cos \chi$:

$$\frac{d\sigma}{d\Omega}(\cos \chi) = \sum_{n=0}^6 C_n (\cos \chi)^n.$$

The expansion coefficients of C_n for a pulse of 2.2 GeV/c and also for pulses of 1.5 and 2 GeV/c [3] are given in Table 2.

Table 1

$\cos \chi$	$\frac{d\sigma}{d\Omega} \left[\frac{\text{mbarn}}{\text{sterad}} \right]$	$\cos \chi$	$\frac{d\sigma}{d\Omega} \left[\frac{\text{mbarn}}{\text{sterad}} \right]$
1,00	$13,2 \pm 1,3$	0,25	$0,20 \pm 0,05$
0,915	$3,77 \pm 0,76$	0,00	$0,30 \pm 0,07$
0,875	$3,42 \pm 0,63$	-0,25	$0,21 \pm 0,05$
0,825	$2,16 \pm 0,44$	-0,50	$0,18 \pm 0,05$
0,75	$1,39 \pm 0,27$	-0,70	$0,10 \pm 0,04$
0,625	$0,63 \pm 0,13$	-0,90	$0,04 \pm 0,02$
0,475	$0,14 \pm 0,05$	—	—

Table 2

C_n	$P_{lab}, \text{GeV/c}$		
	1,5	2,0	2,2
C_0	$0,47 \pm 0,07$	$0,22 \pm 0,03$	$0,25 \pm 0,07$
C_1	$-1,03 \pm 0,31$	$0,52 \pm 0,16$	$0,13 \pm 0,25$
C_2	$3,37 \pm 0,93$	$1,41 \pm 0,46$	$-0,49 \pm 1,06$
C_3	$-0,12 \pm 1,42$	$-3,79 \pm 0,73$	$-2,29 \pm 0,25$
C_4	$-13,97 \pm 3,05$	$-6,18 \pm 1,53$	$-0,65 \pm 3,56$
C_5	$5,55 \pm 1,52$	$7,97 \pm 0,92$	$6,57 \pm 1,58$
C_6	$16,69 \pm 2,67$	$9,68 \pm 1,36$	$5,53 \pm 3,15$

A maximum at $\cos \chi = 0$ was observed in this paper ($P_{\pi^+} = 2.2$ GeV/c). The value of this maximum is comparable with that of the maximum at a 2.0 GeV/c pulse (0.30 and 0.35 mbarn/sterad, respectively). Apparently the cross-section generally has no clearly defined maximums at a large pulse ($P_{\pi} = 2.5$ GeV/c).

Following the example of [9], a dependence was constructed of the coefficients of expanding $\sum_{n=0}^6 C_n(\cos \chi)^n$ from the pulse of the impinging pion.

Figure 3 presents the dependencies which indicate the change of the coefficients of C_n from the pulse in the energy range of 0.5-2.06 GeV [9, 3 and this paper]. It is obvious from the diagram that the coefficient of C_6 has a maximum at a pulse of $P_{\pi} \approx 1.55$ GeV/c. The given value of the pulse corresponds to the total energy in the center of mass system $E_t^* \approx 1.95$ GeV, which is close to the effective mass of known pion-nucleon resonance $N_{3/2}$ (1924). The maximum in the coefficient of C_6 indicates that the f -wave ($l = 3$) makes an important contribution to scattering at a given pulse value ($P_{\pi} = 1.55$ GeV/c). This is found in accordance with the known spin and parity ($7^+/2$) of a given resonance.

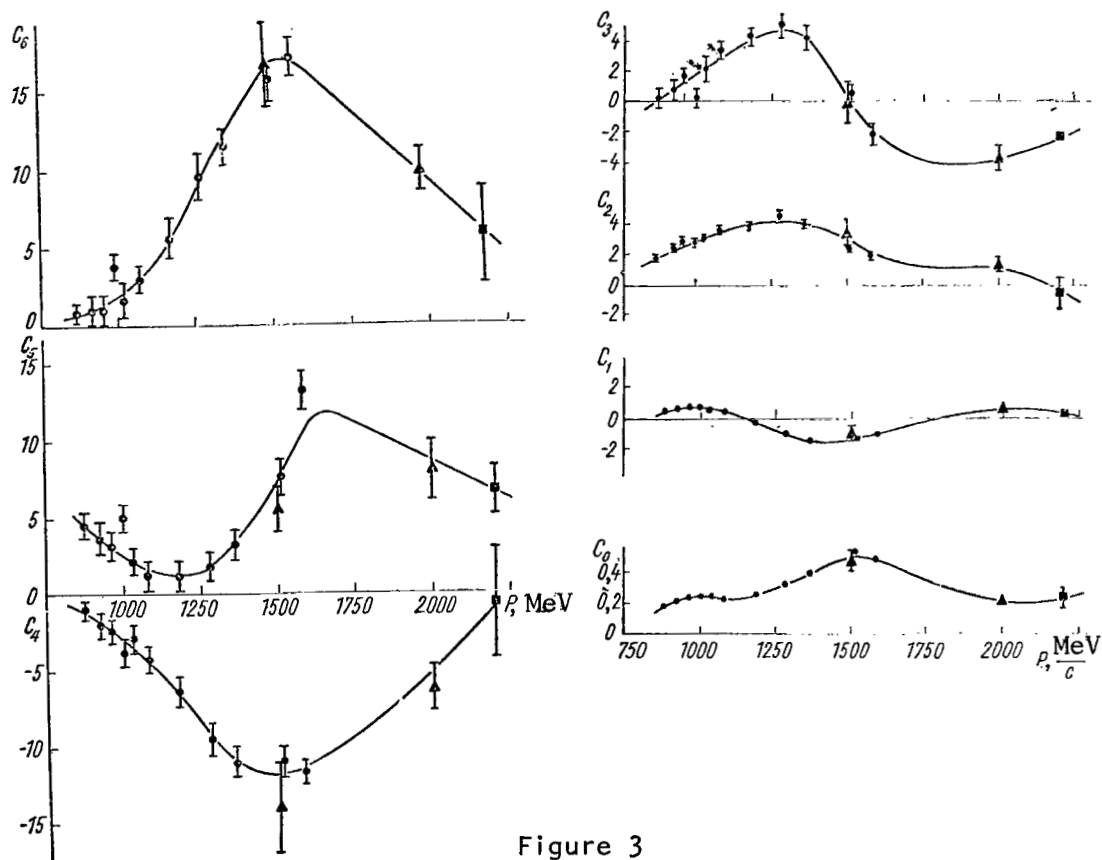


Figure 3

REFERENCES

1. Kruchinin, S. P. et al, *Yadernaya Fizika*, Vol. 1, p. 317, 1965.
2. Mukhin, K. N. et al, *Intern. Conf. on High-Energy Acceler. and Instrum. CERN*, Geneva, p. 514, 1959.
3. Cook, V. et al, *Phys. Rev.*, Vol. 130, p. 762, 1963.
4. Eisner, A. M. et al, *Phys. Rev.*, Vol. 138B, p. 670, 1965.
5. Damouth, D. E., L. W. Jones and M. L. Perl, *Phys. Rev. Lett.*, Vol. 11, p. 287, 1963.
6. Simmons, L. M., *Phys. Rev. Lett.*, Vol. 12, p. 229, 1964.
7. Barut, A. O. and W. S. Au, *Phys. Rev. Lett.*, Vol. 13, p. 489, 1964.
8. Perl, M. L. and M. C. Corey, *Phys. Rev.*, Vol. 136B, p. 787, 1964.
9. D'yuk, R., *Voprosy Fizika Elementarnykh Chastits*. [Problems of the Physics of Elementary Particles], Vol. 5, p. 638, *AN ArmSSR Press*, Ervan, 1966.
10. Barashenkov, V. S., *Phys. Lett.*, Vol. 19, p. 699, 1966.
11. Diddens, A. N. et al, *Phys. Rev. Lett.*, Vol. 10, p. 262, 1963.
12. Hohler, G. et al, *Z. Physik*, Vol. 180, p. 430, 1964.
13. Cronin, J. W., *Phys. Rev.*, Vol. 118, p. 824, 1960.

THE MASS SPECTRUM OF SYSTEMS OF STRANGE PARTICLES GENERATED BY
THE INTERACTION OF π -MESONS WITH LIGHT NUCLEI

V. S. Demidov, V. G. Kirillov-Ugryumov, A. K. Ponosov,
V. P. Protasov and F. M. Sergeyev

ABSTRACT. This paper is devoted to the study of the mass spectrum of systems of strange particles generated by the interaction of π -mesons with light nuclei. The paper investigates the mass spectrum of a system of two neutral strange particles $K^0-\Lambda^0$ and $K^0-\bar{K}^0$ produced by collisions of p^+ -mesons with light nuclei (C, Cl and F). The experiment used a 105-cm bubble chamber filled with a mixture of freon-12 and freon-13. The chamber was irradiated by a beam of negative π -mesons with an average pulse of 3.86 ± 0.04 GeV/c. The authors do not feel that the results are conclusive because of insufficient statistics.

Study of resonance interactions of K-mesons with K-mesons and hyperons is in the initial stages. This assertion first of all relates to K-meson-hyperon resonances, although a number of experiments at several values of initial energy have already been conducted [1-4]. /40

Resonance states with effective masses at energies at the order of 1700 and 1800 MeV have been discovered in different papers for a $K^0-\Lambda^0$ system. However, discernible, sometimes principal discrepancies have been observed between the results of different experiments. One of the reasons for this lies in the rather sparse statistical material of the majority of papers; a possible reason may also be the effect of interactions in final states [1]. Resonances in a $K^0-\bar{K}^0$ system may also not be considered exhaustively studied. On the other hand, we feel that the study of strange particle production (and their resonances) and nuclei is of special interest, because this can add useful information on the properties of nuclei.

This paper investigated the mass spectrum of systems consisting of two neutral strange particles $K^0-\Lambda^0$ and $K^0-\bar{K}^0$ produced by collisions of π^- -mesons with light nuclei (C, Cl, F). The experiment used the 105-centimeter bubble chamber of MIFI [5] which was filled with a mixture of freon-12 and freon-13. The chamber was irradiated by a beam of negative π -mesons with an average pulse of (3.86 ± 0.04) GeV/c of the proton synchrotron of the Institute of Theoretical Physics (ITEP) (Figure 1). A pressure limitation operational mode was used. /41

The chamber was generally photographed with a stereo camera having two objectives of the "Gidrorussar-4" type on standard aerial photographic film

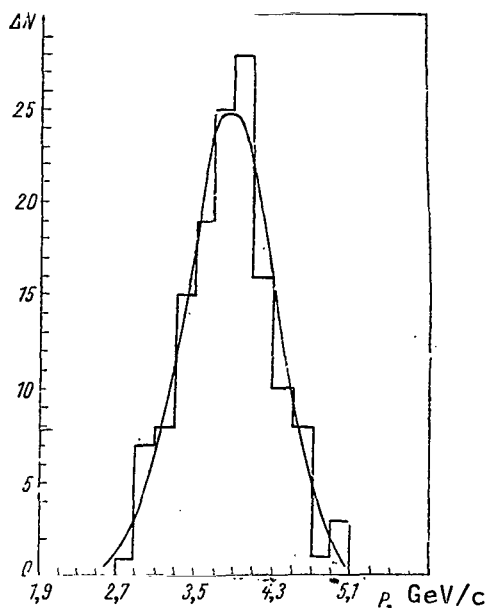


Figure 1. Distribution of the Primary Beam of Pulse P Measured in the Center of the Chamber. The chamber was exposed to a magnetic field of 16.7 kilogauss. The smooth curve is the normal distribution with parameters of $\bar{P} = 3.86 \text{ GeV/c}$ and $\sigma = 0.45 \text{ GeV/c}$.

80 mm wide and with a sensitivity of 1200 units GOST. The measurements were carried out on a UIM-21 microscope and were duplicated by measurements with the help of a stereo projector. A total of 35,000 photographs exposed without a magnetic field have been processed at present. The geometric program was calculated by the M-20 electronic computer.

Reduction of the spatial position of the events studied during stereo photography through several refracting media with consideration of objective distortion is a complicated problem and one which requires special research [6-8].

In our case the specifics of the experiment, determined to a significant degree by the fact that angles were used mainly for identification of the quantitative characteristics, permitted us to use a rather simple method of analytical reduction with the required accuracy.

If we consider the straight lines in the space of the objective subjects as the geometrical location of points of intersection of certain formative planes, then linear surfaces will correspond to these planes in the space of images [4]. The correspondence between the latter and formative planes is quite massive. However, under certain conditions we can place the planes and the space of images in clear conformity to the formative planes in the subject space. Moreover, the position of one or the other is determined completely by the photo projections of the straight lines. It is easy to see that in order to do this we must fulfill the conditions

$$\frac{r_i}{r_{i+1}} \sim 1 \text{ and } \frac{\gamma_i}{\gamma_{i+1}} \sim 1,$$

where r_i is the distance from the optical axis to the i -th point being measured, and γ is the angle of the projected line with the optical axis. We can show with the help of simple geometric calculations that when measuring the axes of two near points of a straight line the planes passing through the projections of these points and the points lying on the optical axes of the objectives at distances of $Z_{1,2} = f/n F_{1,2}(\gamma)$ (for the first and second objectives, respectively) become formative planes.

Here, f is the main rear focus of the objective, n is the refractive index of the operating liquid and $F(\gamma)$ is the coefficient depending both on the direction to the point measured and on the longitudinal spherical aberration of the entrance pupil.

The straight line in the space is determined by the intersection of two formative planes, its directing coefficients being

$$\left. \begin{aligned} m &= \frac{f}{n} [C_1 B_2 F_2(\gamma) - C_2 B_1 F_1(\gamma)]; \\ n &= \frac{f}{n} [C_1 F_2(\gamma) - C_2 F_1(\gamma)]; \\ p &= \frac{f^2}{n^2} F_1(\gamma) \cdot F_2(\gamma) [B_2 - B_1], \end{aligned} \right\} \quad (1)$$

where $B_{1,2}$ and $C_{1,2}$ are the coefficients of equations of projecting a straight line onto the photographic plane ($x + By + C = 0$) for the first and second objectives, respectively.

If, as this has been observed in our case (see the Table), the distortion function $F(\gamma)$ hardly changes by the volume photographed [$F_1(\gamma) \approx F_2(\gamma) \approx F(\gamma)$], then the expressions of (1) are simplified:

$$\left. \begin{aligned} m &= \frac{f}{n} F(\gamma) [C_1 B_2 - C_2 B_1] = K_1 [C_1 B_2 - C_2 B_1]; \\ n &= \frac{f}{n} F(\gamma) [C_1 - C_2] = K_2 [C_1 - C_2]; \\ p &= \frac{f^2}{n^2} F^2(\gamma) [B_2 - B_1] = K_3 [B_2 - B_1]. \end{aligned} \right\} \quad (2)$$

We determined the multipliers K_1 , K_2 , and K_3 by photographing a body-centered reference lattice installed in the chamber (this also permits us to automatically calculate film contraction).

The accuracy of reducing the space picture by the method selected is rather high as can be seen from the table.

For processing, we selected stars formed by primary π^- -mesons and correlated with two characteristic V^0 -events of each ($K^0 \rightarrow \pi^+ + \pi^-$ and $\Lambda^0 \rightarrow p + \pi^-$ decays) (Figure 2). Identification of strange particles was accomplished according to the divergence angle of the products of their decay and paths. Complete paths were determined for the secondary particles remaining in the chamber, and the lower energy boundary was estimated for the tracks emerging along the recording length. The characteristics of stopping (a π^- -meson star,

/43

$\pi^+ \rightarrow \mu^+ \rightarrow e^+$ -decay, etc.) was calculated when identified. Qualitative analysis of relative ionization and multiple scattering were also used.

Viewing Angles of the Objectives		Angle in the Chamber	Calculated Value of the Angle, ϕ_{cal}
β_1	β_2		
For a Plane Parallel to the Photographic Plane			
24°45'	15°48'	4°24'	4°25'
		8°08'	8°14'
		12°32'	12°36'
		45°00'	44°48'
		63°24'	63°13'
		90°00'	89°27'
22°20'	14°09'	4°24'	4°22'
		8°08'	8°16'
		12°27'	12°23'
		45°00'	44°57'
		63°24'	63°39'
20°19'	12°47'	4°24'	4°27'
		8°08'	8°14'
		12°32'	12°39'
		45°00'	44°30'
		63°24'	62°46'
For a Plane Perpendicular to the Photographic Plane			
24°45'	15°48'	4°24'	4°12'
		8°08'	8°18'
		12°32'	12°32'
		33°42'	33°31'
		56°18'	55°54'
		90°00'	89°24'
19°38'	19°38'	4°24'	4°40'
		12°32'	12°27'
		33°42'	33°19'
		45°00'	45°15'
		63°24'	63°26'
		90°00'	89°54'

The portion of V^0 -events selected are secondary two-pronged stars, formed by neutrons from a parent star. We checked the coplanarity of the V^0 -event with a primary star in order to eliminate the neutron background. The coplanarity requirement of the production point of a strange particle and its decay plane ensues from the requirements of pulse reservation. Because of coplanarity, we used the angle between the straight line determining the direction of motion of the strange particle and the plane of its decay. It turned out that the overwhelming number of events is within the limits of the angle of non-coplanarity $\phi = 2^\circ$. Events with an angle $\phi \leq 1.5^\circ$ were left for subsequent analysis.

One hundred forty one events in the material studied were identified as production of a $K^0\text{-}\Lambda^0$ -pair and 68 events--as production of $K^0\text{-}\bar{K}^0$.

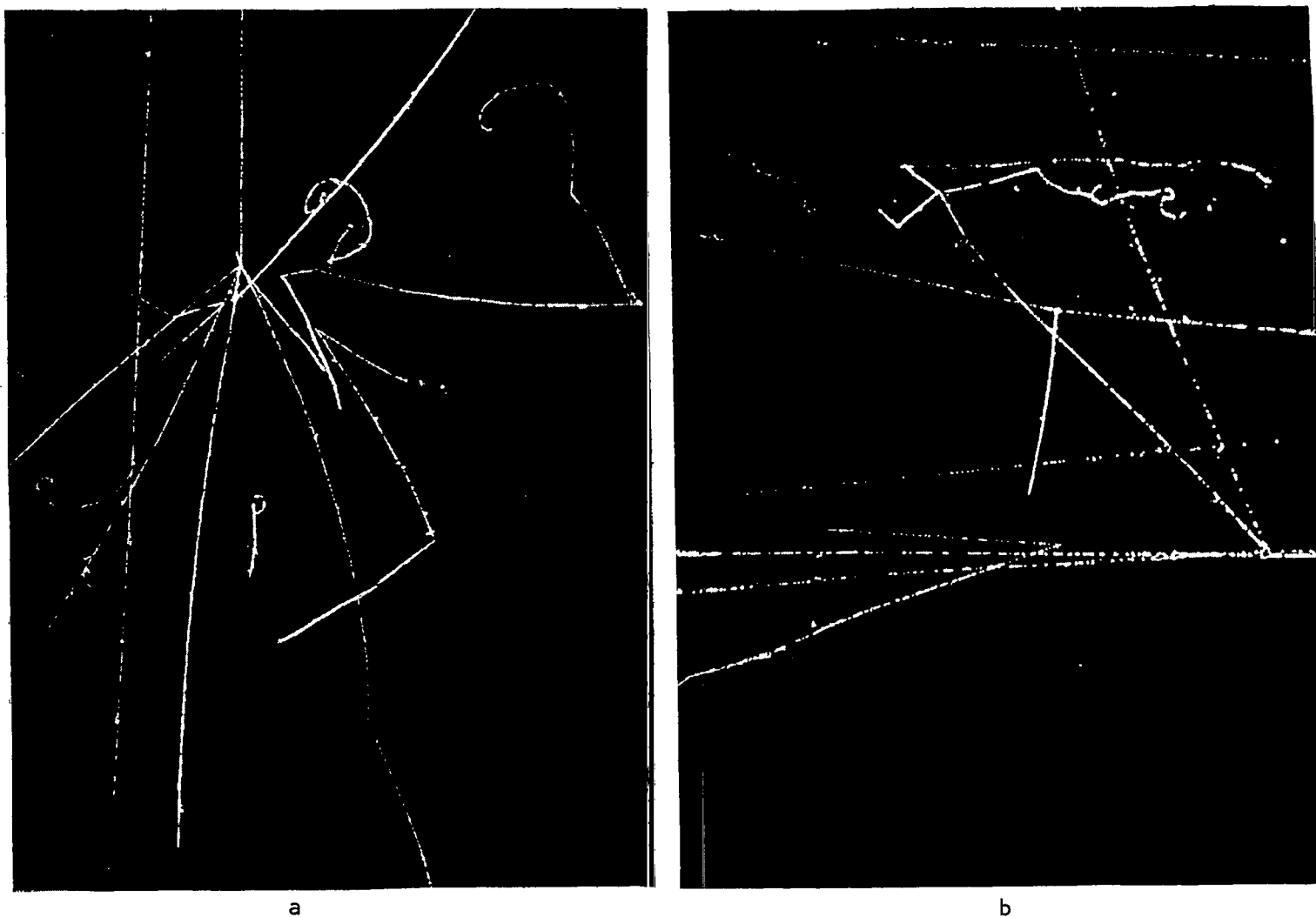


Figure 2. A Characteristic Case of the Joint Production of a Λ^0 -Hyperon and a K^0 -Meson (a) Recorded by the MIFI Chamber Upon Irradiation in a Magnetic Field of 16.7 kilogauss, and of the Joint Production of K^0 - and K^+ -Meson (b)

Distribution of the effective mass M_{eff} of a $K^0-\Lambda^0$ system is presented in Figure 3. Figure 4 gives the distribution of M_{eff} of a $K^0-\bar{K}^0$ pair.

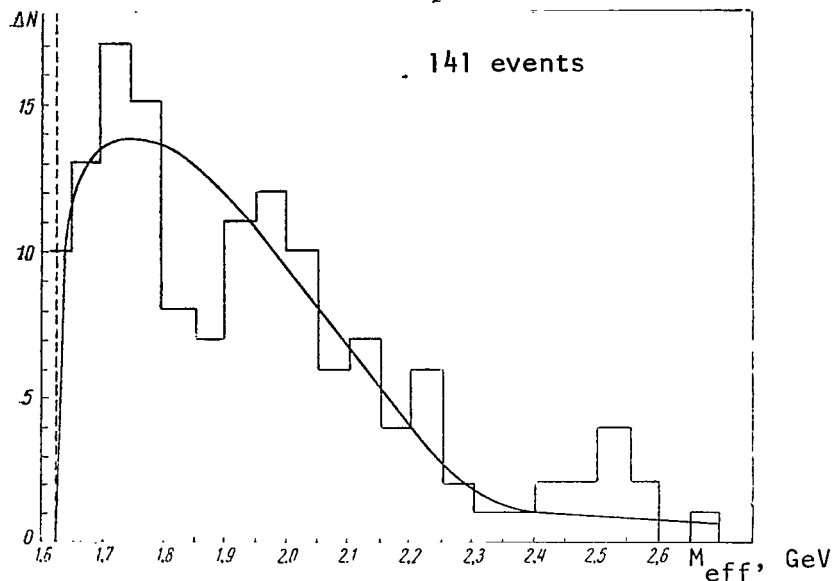


Figure 3. Distribution of Effective Mass for a $K^0 = \Lambda^0$ System. The smooth curve was calculated by the "random stars" method.

The statistical distribution of 250 $K^0-\Lambda^0$ -events was calculated for comparison by the "random stars" method. The standard for the total number of events was 141. Both double and single V^0 -events were used in the "phase curve".

A certain increase of the number of recorded events above the phase curve is observed on the histogram (Figure 3) in the range of effective masses of a system of $K^0-\Lambda^0 \sim 1.65 < M_{\text{eff}} < \sim 1.8$ GeV. An irregularity is also noticed in the range of the values from 1.85 to ~ 2 GeV (the average is ~ 1.95 GeV).

The anomaly near $M_{\text{eff}} \sim 1.7$ GeV may be explained by the decay of $K^0-\Lambda^0$ into a pair of known resonants $N_{1(3)}^*$ ($M = 1.688$ GeV). Regarding the peak corresponding to the average value $M_{\text{eff}} = 1.95$ GeV, the resonance is not yet known in a π -N system with such a mass and corresponding value of isotropic span.

The peak and the distribution of effective masses of a $K^0-\Lambda^0$ -system with an average value of ~ 1.700 GeV was noted for π^-p -interactions with primary energies of ~ 3 and 3.86 GeV [2, 3]. The possible existence of resonance at values of $M_{\text{eff}} \sim 1.9-2.0$ GeV was also pointed out in [2]. However, the statistics in these papers are not large.

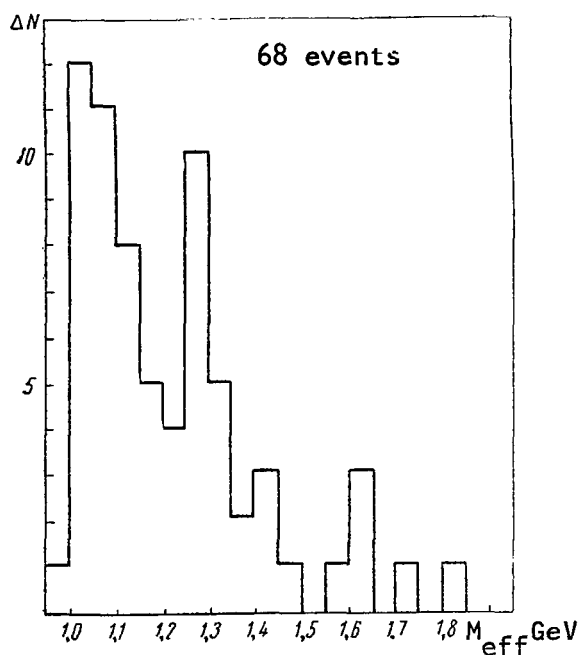


Figure 4. Distribution of Effective Mass for a $K^0\text{-}\bar{K}^0$ System.

would also be interesting to compare the results of experiments for different primary energies. The maximum phase distribution should be shifted to the side of large values of M_{eff} as energy increases, at the same time as the peculiarities in the mass spectrum caused by resonances maintain their position.

We noted a grouping of events near the average value of $M_{\text{eff}} \sim 1.1 \text{ GeV}$ and $M_{\text{eff}} \sim 1.28 \text{ GeV}$, which are stable during variation of subdivisions according to the ranges of effective masses, in the distribution of effective mass of a $K^0\text{-}\bar{K}^0$ system. The primary grouping corresponds to the known near-threshold peculiarities ($M_{\text{eff}} = 1.02\text{-}1.10 \text{ GeV}$), and the second grouping corresponds to the resonance with a mass of $\sim 1280 \text{ MeV}$ recently discovered in [9]; the latter may be considered as a manifestation of the decay of an A_2 or f^0 -meson according to the pattern $A_2 f^0 \rightarrow K^0 + \bar{K}^0$. However, further research is required in this area.

The irregularities indicated in the distributions obtained for effective mass of a $K^0\text{-}\bar{K}^0$ -system indicates that a satisfactory solution was achieved in our experiment, but, as in the case of a $K^0\text{-}\Lambda^0$ system, inadequate statistics do not permit us to make any final conclusions.

In conclusion we thank the administration of ITEP for giving us the opportunity to conduct the experiment.

A distribution of M_{eff} of 355 $\Lambda^0\text{-}K^0$ pairs was attained in [10], for π^-p -interactions at an energy of 7.91 GeV. Ejections were distinctly observed in the distribution at a value of $M_{\text{eff}} \sim 1.65$, $M_{\text{eff}} \sim 1.85$ and $M_{\text{eff}} \sim 1.925 \text{ GeV}$. It is however necessary to note that no irregularities were discovered in the mass spectrum of the $K^0\text{-}\Lambda^0$ system in the well-provided statistics of [4], where the interaction of π^- -mesons with nuclei was studied at a π -meson energy of 2.8 GeV.

Despite the peculiarities noted above of the mass spectrum of a $K^0\text{-}\Lambda^0$ system obtained by us and coinciding with the results of a number of papers, the low statistics (141 events) does not permit us to make any final conclusions. We feel that, in addition to an increase of statistics, detailed study of the phase distributions for production in nuclei is in order. It

/48

We are grateful to M. G. Goronov and V. I. Vemekhin for their great assistance in the work.

REFERENCES

1. Barashenkov, V. S., *Secheniya Bzaimodeystviy Elementarnykh Chastits*, [Cross Sections of Interactions of Elementary Particles], Nauka Press, Moscow, 1966.
2. Wangler, T. P. et al, *Phys. Rev.*, Vol. 137B, p. 414, 1965.
3. Bannik, B. P. et al, *Trudy XII Mezhdunarodnoy Konferentsii Po Fizika Vysokith Energiy. Dubna 1964*, [Proceedings of the Twelfth International Conference on High Energy Physics. Dubna 1964], Vol.1, Atomizdat Press, p. 682, Moscow, 1966.
4. Baramin, V. V. et al, *Yadernaya Fizika*, Vol. 3, p. 342, 1966.
5. Alikhanyan, A. I. et al, From the collection, *Fizika Elementarnykh Chastits* [Physics of Elementary Particles], p. 76, Atomizdat Press, p. 76, 1966.
6. Aleksandrov, Yu. A. et al, *Puzyr'kovyye Kamery*, [Bubble Chamber], Atomizdat Press, Moscow, 1963.
7. Buzdavina, N. A. et al, *Preprint No. 2095 of OIYaY*, Dubna, 1965.
8. Ivanchenko, I. M. et al, *Preprint No. 2889 of OIYaY*, Dubna, 1966.
9. Barmin, V. V. et al, *Trudy XII Mezhdunarodnoy Konferentsii Po Fizika Vysokith Energiy. Dubna 1964*, [Proceedings on the Twelfth International Conference on High Energy Physics. Dubna 1964], Vol. 1, p. 433, Atomizdat Press, Moscow, 1966.
10. Ehrlich, R. et al, *Preprint Univers. of Pennsylvania*, Philadelphia, Pa., 1966.

THE THEORY OF COMPLEX MOMENTS AND RESONANCE NUCLEAR REACTIONS

V. V. Grushin and Yu. P. Nikitin

ABSTRACT. This article investigates the SAU (inherent asymmetry of nuclear level) effects which occur during resonance interaction of spinless particles as well as particles having spins of 0 and 1/2, within the limits of the Khuri concept which has many advantages when compared with the Regge concept. The article presents a step-by-step calculation of Coulomb interaction which must be taken into consideration during resonance scattering of charged particles. The developed theory is then applied to resonance scattering of α -particles and protons in a C^{12} nucleus. The path of the Regge pole trajectories was established when compared with the experiment. It is shown that the Khuri method leads to results hardly differing in the case of the scattering of α -particles in a C^{12} nucleus from the results of the papers cited.

1. Introduction

Resonance nuclear reactions in the low energy range have until recently been analyzed theoretically on the basis of the well-known Breit-Wigner formula. The resonance character of a nuclear reaction in the Breit and Wigner theory is determined by the field of the reaction amplitude in the complex energy plane close to that approaching the real energy axis. Assuming a sufficient remoteness of other such fields from the real energy axis, we can limit ourselves to a single-pole Breit-Wigner amplitude when describing a resonance reaction. The angular distribution of secondary particles in this case will be determined completely and, for example, will be the square of a Legendre polynomial of the l -th order for spinless particles, where l is the orbital moment of the particles involved in a resonance nuclear reaction. Deviations are usually observed in practice from the simple Breit-Wigner type and it becomes necessary to supplement the Breit-Wigner amplitude by correction components which represent scattering in states with a non-resonance value of orbital moment l . Moreover, if the value of $kR \gg 1$ (k is the pulse of the impinging particles in the center of mass system, and R is the radius of the interaction), the number of significant non-resonance partial amplitudes is sufficiently large, of the order of kR . In order to parameterize the amplitude of the resonance reaction, we must conduct a rather cumbersome phase analysis with a large number of varying phases ($\sim kR$). The results of such an analysis are often inconclusive and require additional data or hypothesis in order to determine the true collection of phases.

A substantially different approach to resonance nuclear reactions [1-4] based on the theory of Regge poles [5, 6] has been noted recently. Its main

idea is that the pole of the scattering amplitude in a complex plane of orbital moment l (a Regge pole), closely approaching the whole-number value of l , will lead to resonance in a nuclear reaction. Moreover, if other Regge poles are located at a distance from the real axis of l , their contribution to the amplitude of the reaction is exponentially small [1], and we may limit ourselves /50 to consideration of only a single resonating pole.

Thus, the real moment of resonance state in the theory of Regge poles is complex, and although the difference of the resonance moment from the whole-number value is small, it can lead to a substantial difference of scattering amplitude from the simple Breit-Wigner type. In particular, as indicated in [1], the angular distribution of the secondary particles generated in a resonance nuclear reaction of the type $a + A \rightarrow b + B$ has a characteristic asymmetry, i.e., it differs from the predicted Breit-Wigner theory. This asymmetry was called the inherent asymmetry of the nuclear level [SAU] [1].

In order to explain such asymmetry in the generally accepted theory of resonance nuclear reactions, it would be necessary to attract a large number of non-resonance phases. This gives rise to the very important question of the possibility of observing in experiment the SAU effect and of the self-consistence of the theory of complex moments. As the analysis of the data on resonance elastic scattering of α -particles in nuclei of C^{12} showed [1-3], the theory of Regge poles permits us to describe the experimental angular distribution of secondary particles quite satisfactorily with the help of two parameters, (the real and imaginary parts of the position of the resonating Regge pole). The authors of [1, 2, 3] having inducted analysis of the data by two different methods, the first group found the parameters of the Regge pole on the basis of phase analysis [7], and the second group--on the basis of experimental angular distribution. The trajectories of the Regge pole found in such a manner, which cause resonance with quantum numbers of 1^+ (the P-state with positive parity), were almost coincident. The results of [1, 2, 3], which are practically the first serious attempt to work out and justify by comparison through experiment the new approach to resonance nuclear reactions, are quite encouraging.

Further theoretical and experimental studies in this area will, in our opinion, be of significant interest from the point of developing the Regge-pole approach to resonance nuclear reactions and for establishing actual limits for its application. The advantages of such an approach are obvious--there is the tempting possibility to sharply decrease the number of parameters describing resonance scattering. If different resonance nuclear reactions are determined by the same Regge pole, the angular distributions of secondary particles should coincide, i.e., it becomes possible to predict on the basis of the data on a single process the possible characteristics of another process. It is easy to generalize the method for cases when two or more close resonances occur [1]. /51

We are investigating in this article the basis of the theory of complex moments the SAU effects which occur during resonance interaction of both spinless particles and of particles with spins of 0 and $1/2$, within the limits of the Khuri concept [8], which has many advantages when compared with the Regge

concept [5, 6] used by the authors of [1-4]. The Khuri concept [8], in distinction from the Regge concept [5, 6], leads to correct analytical properties of scattering amplitude in the complex plane $z(z = \cos \vartheta, \vartheta$ is the scattering angle in the center of mass system) and to the exponential decrease of partial scattering amplitudes as the moment of l increases. This circumstance permits us to hope that the area of applicability of the method developed according to the variable ϑ function will be broader than that indicated in [1]. In the case of resonance interaction of particles with spins of 0 and 1/2, as indicated in [9], yet another interesting effect occurs in addition to the SAU effect, namely, polarization of secondary particles which is not present in a purely Breit-Wigner case. The theory of complex moments predicts the angular process of polarization.

This result permits us to carry out direct verification of the hypothesis of complex moments on the basis of experimental data and to establish the limits of its applicability. We present in the article step-by-step calculation of Coulomb interaction which must be taken into consideration during resonance scattering of charged particles. The theory developed is then applied to resonance scattering of α -particles and protons in a nucleus of C^{12} . The path of the trajectories of Regge poles is determined when compared with the experiment. It was shown that the Khuri method leads to results which differ slightly in the case of α -particle scattering in a C^{12} nucleus from the results from [1-3].

Upon analysis of the data on α -particle scattering in a C^{12} nucleus the position of the amplitude cross-section of the reaction in a complex plane of variable z was considered as a variable parameter. The value of this parameter found by analysis was quite close to that calculated theoretically. This result also proves the benefit of the concept being developed.

2. Scattering Amplitude of Spinless Particles in the Khuri Concept

It was shown in the non-relativistic theory of complex moments developed in the papers of Regge [5, 6] that scattering is a meromorphic function of orbital moment l in a half-plane $\text{Re} l > -1/2$. Applying in this case the Watson-Sommerfeld transformation [5, 6] to the usual expansion of scattering amplitude into a series by Legendre polynomials, Regge obtained the following concept for scattering amplitude $f(s, z)$ [$s = k^2$ is the square of the pulse in the center of mass system, and $z = \cos \vartheta$; ϑ is the scattering angle in the center of mass system]:

$$\begin{aligned} f(s, z) &= \frac{1}{k} \sum_l (2l+1) f_l(s) P_l(z) = \\ &= -\frac{i}{k} \int_{-i\infty}^{i\infty} \lambda P_{\lambda-1/2}(-z) \frac{f(\lambda, s)}{\cos \pi \lambda} d\lambda - \\ &\quad - \pi \sum_{n=1}^N \frac{r_n(s) P_{\lambda_n-1/2}(-z) \cdot 2i_n}{k \sin l_n \pi}, \end{aligned} \quad (1)$$

where $\lambda = l + 1/2$, $P_j(z)$ is a Legendre function of the first type, $l_n = \lambda_n - 1/2$ is the position of the n -th pole of the meromorphic function $f(\lambda, s)$ [the Regge pole] in the half-plane of a complex variable, λ and $r_n(s)$ is the deduction in the pole of partial amplitude $f(\lambda, s)$, and N is the number of poles of $f(\lambda, s)$ when $\text{Re } \lambda > 0$. The meromorphicity of $f(\lambda, s)$ was not proved for an arbitrary potential. However, it was indicated in Khuri's paper [8] that the concept of (1) occurs in a quite ordinary case when the interaction is described by superposition of Yukawa potentials, i.e.,

$$rV(r) = \int_m^\infty g(\mu) e^{-\mu r} d\mu, \quad (2)$$

where $V(r)$ is the interaction potential. The partial amplitude of $f(\lambda, s)$ in the half-plane $\text{Re } l > -1/2$ is meromorphic and has $|l| \rightarrow \infty$ in asymptotic behavior.

$$f(\lambda, s) \sim \frac{C(s)}{\sqrt{\lambda}} e^{-\lambda \xi}, \quad (3)$$

where $\cosh \xi = 1 + m^2/2s$, m is the lower limit of integration in formula (2).

We note that the polar members in formula (1) return to infinity when $z \rightarrow 0$ and consequently cannot be the real scattering amplitude over the entire range of angles of secondary particle escape [1]. Moreover, if expression (1) is continued analytically to non-physical complex values of z , each of the two members in expression (1) will have a cross-section beginning at $z = 1$. It is nevertheless known [12] that the cross-section in a z -plane at an amplitude of $f(s, z)$ begins at $z = \cosh \xi = 1 + m^2/2s$. However, it becomes possible to find another concept of $f(s, z)$ free of the disadvantages indicated above [8]. In order to do this we turn to the following integral concept of Legendre function which occurs in the range of $-1/2 < \text{Re } \lambda < 1/2$: /53

$$\frac{\pi \lambda P_{\lambda-1/2}}{\cos \pi \lambda} = \frac{1}{2^{3/2}} \int_{-\infty}^{\infty} \frac{e^{\lambda x} \text{sh } x \, dx}{(\text{ch } x - z)^{3/2}}. \quad (4)$$

The integral in (1) is selected according to the path of $\text{Re } \lambda = 0$ and consequently expression (4) may be substituted in it. In this case,

$$f(s, z) = \frac{1}{k \sqrt{2}} \int_{-\infty}^{\infty} \frac{B(x, s) \text{sh } x \, dx}{(\text{ch } x - z)^{3/2}} + 2\pi \sum_{n=1}^N \frac{r_n P_{\lambda_n-1/2}(-z)^{\lambda_n}}{k \cos \pi \lambda_n}, \quad (5)$$

where

$$B(x, s) = \frac{1}{2\pi i} \int_{-i\infty}^{+i\infty} d\lambda e^{\lambda x} f(\lambda, s). \quad (6)$$

When $x < \xi$, it is possible, by using (3) and the fact that the function of $f(\lambda, s)$ is meromorphic in the right half-plane, to express the integral of B by the poles of f located in the right half-plane of $\text{Re } \lambda > 0$. In order to do this, we present the function of B in the form

$$B \equiv B_L \vartheta(x - \xi) + B_R \vartheta(\xi - x). \quad (7)$$

Here $\vartheta(y)$ is a step function-- $\vartheta(y > 0) = 1$ and $\vartheta(y < 0) = 0$. Where $x < \xi$ the contour in (6) may be enclosed in the right-half-plane of λ . As a result

$$B(x, s) = B_R(x, s) = - \sum_{n=1}^N r_n(s) e^{\lambda_n x}, \quad x < \xi. \quad (8)$$

We will now write concept (6) as

$$\begin{aligned} f(s, z) = & \frac{1}{\sqrt{2} k} \int_{\xi}^{\infty} \frac{B_L \text{sh } x \, dx}{(\text{ch } x - z)^{3/2}} + \frac{1}{k} \times \\ & \times \sum_{n=1}^N r_n \left[-\frac{1}{\sqrt{2}} \int_{-\infty}^{\xi} + \frac{e^{\lambda_n x} \text{sh } x \, dx}{(\text{ch } x - z)^{3/2}} + \frac{2\pi \lambda_n P_{\lambda_n - 1/2}(-z)}{\cos \pi \lambda_n} \right]. \end{aligned} \quad (9)$$

We can prove [8] that the cross-section in the complex z -plane of the expression in brackets begins from point $z = 1 \text{ m}^2/2s$, as it should be for potentials of type (2). Since the meromorphicity of $f(\lambda, s)$ is not proved in a general case, we shall consider that the amplitude cross-section is determined in each specific case by analysis of the characteristics of scattering amplitude according to variable z on the basis of the simplest Feinman diagram [13]. If $f(\lambda, s)$ is meromorphic over the entire λ -plane, B_L is determined by left ($\text{Re } \lambda < 0$) characteristics of $f(\lambda, s)$. In this case

$$f(s, z) = \frac{1}{k} \sum_{n=1}^{\infty} R(s, z, \lambda_n) \quad (10)$$

where

$$\begin{aligned} R = r_n(s) \left[-\frac{1}{\sqrt{2}} \int_{-\infty}^{\xi} \frac{e^{\lambda_n x} \text{sh } x \, dx}{(\text{ch } x - z)^{3/2}} + \right. \\ \left. + \frac{2\pi \lambda_n P_{\lambda_n - 1/2}(-z)}{\cos \pi \lambda_n} \right], \quad \text{Re } \lambda_n > 0; \end{aligned} \quad (11)$$

$$R = \frac{r_n(s)}{\sqrt{2}} \int_{-\infty}^{\infty} \frac{e^{\lambda_n x} \operatorname{sh} x \, dx}{(\operatorname{ch} x - z)^{3/2}}, \quad \operatorname{Re} \lambda_n < 0. \quad (12)$$

Summation in (10) is carried out for all poles of partial amplitude $f(\lambda, s)$. Concept (9) is called the Khuri concept [8] and will be used henceforth. The Khuri concept in a relativistic case should be modified by calculating the left-handed cross-section of scattering amplitude in the complex plane λ . We shall henceforth limit ourselves to consideration of only a non-relativistic case and will discount the contribution of the left-handed cross-section having an order of relativistic correction.

3. Differential Scattering Cross-Section of Spinless Particles

Let us consider a case when one of the poles of partial amplitude $f(\lambda, s)$ approached near the real axis of the plane of λ to a semi-integral value (i.e., to an integral value of moment l). We shall introduce the notation

$$\lambda_i = l + \nu(s) + 1/2, \quad |\nu(s)| \ll 1, \quad (13)$$

where λ_i is the position of the pole approaching the semi-integral value. If the other poles $\lambda_n(s)$ are located in the complex plane at a distance from the real axis, the term in (11) corresponding to λ_i will be large in comparison with 55 the remaining terms¹, and may be limited only by the polar amplitude corresponding to the pole of λ_i which by virtue of (13) may be presented approximately in the form

$$f(s, z) = \frac{r_i}{k} \left[-\frac{2l+1}{\nu} P_l(z) - P_l(z) - (2l+1) R_l(z) - S_l(\xi, z) + o(\nu) \right]. \quad (14)$$

Here

$$S_l(\xi, z) = \frac{1}{\sqrt{2}} \int_{-\infty}^{\xi} \frac{e^{(l+1/2)x} \operatorname{sh} x}{(\operatorname{ch} x - z)^{3/2}} dx; \quad (15)$$

$$R_l(z) = (-)^l \left[\frac{\partial P_\lambda(-z)}{\partial \lambda} \right]_{\lambda=l}. \quad (16)$$

The functions of $R_l(z)$ were introduced in [1] where recurrent relations

¹ It is simple to ascertain from concepts (1) or (9) that the contribution of the poles far removed from the real axis are exponentially small according to the variable of λ_n [1].

and the concrete form of functions $R_l(z)$ are reduced for $l = 0, 1, 2, 3$ and 4. Since the main term in the amplitude of (14) has an order of $1/v$ according to the variable v , it is valid for us to calculate the remaining corrections (~ 1), because corrections from other polar members are exponentially small because of their remoteness from the real axis.

Let us clarify the transition from (14) into the Breit-Wigner formula.

For a narrow resonance $\left[\frac{\Gamma}{E_0} \ll 1, \Gamma \text{ the width and } E_0 \text{ is the location of resonance} \right] v(E) = \mathcal{N}(E_0) \left(E - E_0 + i \frac{\Gamma}{2} \right)$ is close to $E = E_0$, and the main term in (14) assumes the Breit-Wigner form

$$f(s, \lambda) = - \frac{(2l+1)}{k} \cdot \frac{\Gamma}{E - E_0 + i \frac{\Gamma}{2}} P_l(z), \quad (17)$$

where $\Gamma = \frac{r_l(E_l)}{\lambda_l'(E_l)}$. As was noted in [1], no other characteristic other than the poles could lead to the Breit-Wigner formulas. The Khuri scattering amplitude (14) possesses the correct analytical properties in the z -plane, remains finite during forward scattering and its partial amplitudes decrease exponentially as l increases, as it should be according to general physical concepts, /56
by virtue of the finiteness of the action radius of nuclear forces:

$$\begin{aligned} f_l(s, \lambda_l) &= \frac{1}{2} \int_{-1}^1 P_{\lambda-l/2}(z) R(s, z, \lambda_l) dz = \\ &= r_l \frac{e^{-(\lambda-\lambda_l)z}}{\lambda-\lambda_l}; \quad \lambda = l+1/2. \end{aligned} \quad (18)$$

Thus, the amplitude and the Khuri concept [8] satisfies the basic physical requirements necessary, which makes it possible to look forward to a description of resonance scattering over a wider range of angles of secondary particle escape than was noted in [1].

In the case when scattering amplitude may be presented in the form of (14), the differential scattering cross-section of spinless particles has the form

$$\frac{d\sigma}{d\Omega} = \frac{|r_l|^2}{k^2 |v|^2} [(2l+1)^2 P_l^2 + 2 \operatorname{Re} v \{ (2l+1) P_l^2 + (2l+1)^2 P_l \mathcal{R}_l \}] + o(v). \quad (19)$$

Here

$$\mathcal{R}_l = R_l + \frac{1}{2l+1} S_l. \quad (20)$$

In the case of $l = 0, 1, 2$, and 3 the functions of R_l have the form

$$\begin{aligned}
 \mathcal{R}_0 &= \ln \frac{\sqrt{e^{2\xi} - 2e^\xi z + 1} + e^\xi - z}{2} - \frac{2e^\xi}{\sqrt{e^{2\xi} - 2e^\xi z + 1}}, \\
 \mathcal{R}_1 &= z \ln \frac{\sqrt{e^{2\xi} - 2e^\xi z + 1} + e^\xi - z}{2} + z + \\
 &\quad + \frac{3 + e^{2\xi} - 6e^\xi z}{3\sqrt{e^{2\xi} - 2e^\xi z + 1}}; \\
 \mathcal{R}_2 &= P_2(z) \ln \frac{\sqrt{e^{2\xi} - 2e^\xi z + 1} + e^\xi - z}{2} + \frac{7}{4}(z^2 - 1) + \\
 &\quad + \frac{3}{2}z + \frac{e^{3\xi} + 5e^{2\xi} - 5e^\xi(4 + z^2) + 15z}{10\sqrt{e^{2\xi} - 2e^\xi z + 1}}; \\
 \mathcal{R}_3 &= P_3(z) \ln \frac{\sqrt{e^{2\xi} - 2e^\xi z + 1} + e^\xi - z}{2} + \frac{37}{12}z^3 + \frac{30}{18} \times \\
 &\quad \times z^2 - \frac{5}{4}z - \frac{8}{18} + \\
 &\quad + \frac{6e^{4\xi} + 21ze^{3\xi} + 21(5z^3 - 2)e^{2\xi} + 21z(30z^2 - 13)e^\xi + 21(15z^2 - 4)}{126\sqrt{e^{2\xi} - 2e^\xi z + 1}}.
 \end{aligned} \tag{21}$$

Figure 1 presents the graphs of the functions

$$\frac{d\sigma}{d\Omega_x} \cdot \frac{k^2 |v|^2}{|r_i|^2} \text{ and } \frac{d\sigma}{d\Omega_{\text{BW}}} \cdot \frac{k^2 |v|^2}{|r_i|^2}$$

for different values of l . Here $d\sigma/d\Omega_x$ is from (19) and $d\sigma/d\Omega_{\text{BW}}$ is the Breit-Wigner differential scattering cross-section. As can be seen, deviation from the Breit-Wigner cross-section may reach 20% (Rev was considered approximately equal to 0.02. This will be stipulated somewhat later.

4. Differential Scattering Cross-Section and Polarization of Particles with Spins of 0 and 1/2

Let us now consider a more complex case of scattering of particles with spins of 0 and 1/2. The amplitude of such a process may be presented in the form

$$F(E, \vartheta) = A(E, \vartheta) + \sigma n B(E, \vartheta), \tag{22}$$

where A and B are the scattering amplitudes with and without spin flip, respectively, and n is the single pseudovector perpendicular to the plane of reaction. It is assumed that the relative internal parity of the particles does not change during the course of the interaction. Scattering amplitudes A and B may usually be expanded into a series of partial amplitudes describing the interaction in states with a definite total moment j and a parity of $P = (-)^{P_0}$,

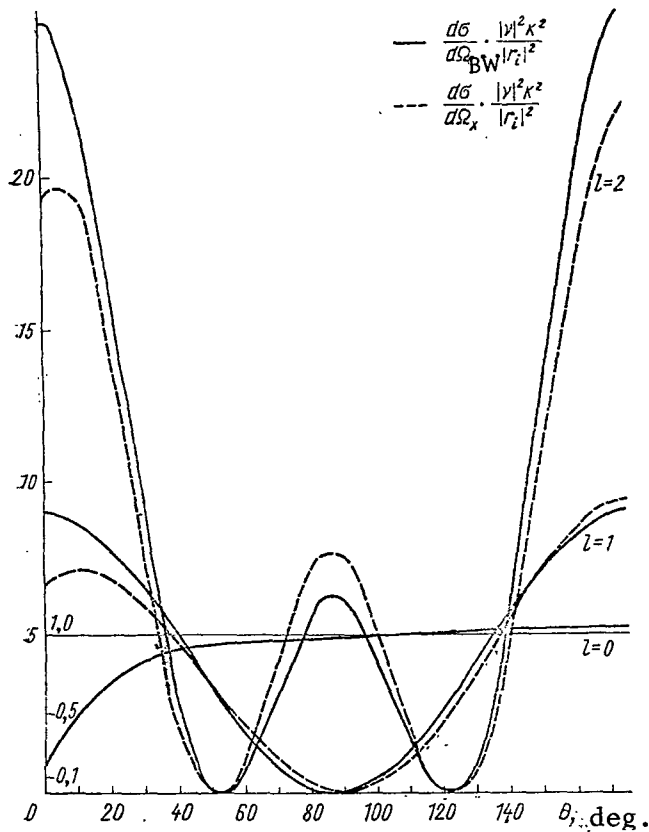


Figure 1. Angular Distributions of the Resonance Differential Scattering Cross-Sections in States with Orbital Moments of $l = 0, 1$, and 2 , Obtained by Breit-Wigner Formulas (the solid line) and by Formula (19) of this Paper (the broken line).

where l is the orbital moment and P_0 is the internal parity of the interacting particles,

$$\left. \begin{aligned} A(E, \vartheta) &= \frac{1}{k} \sum_{l=0}^{\infty} [(l+1) f_l^+(E) + l f_l^-(E)] P_l(\cos \vartheta); \\ B(E, \vartheta) &= \frac{-i}{k} \sum_{l=1}^{\infty} [f_l^+(E) - f_l^-(E)] P_l^1(\cos \vartheta). \end{aligned} \right\} \quad (23)$$

In the formulas (23) k is the pulse of the reaction and the center of mass system, $f_l^{\pm}(E)$ are the partial interaction amplitudes in states with a total moment $j = l \pm 1/2$ and a parity of $P = (-)^{j+1/2} P_0$, respectively, and E is the total energy in the center of mass system. In the case of elastic scattering

$f_l^{\pm}(E) = e^{i\delta_l^{\pm}} \sin \delta_l^{\pm}$, where δ_l^{\pm} are the phases of scattering in states with the

total moment $j = l \pm 1/2$. Fulfilling the Khuri transformation [8] described in Section 2, we can write amplitudes A and B in the form of the sum of the contributions from all poles of partial amplitudes:

$$\left. \begin{aligned} A &= \sum_n R_n^+ + \sum_r R_r^-; \\ B &= \sum_n S_n^+ + \sum_r S_r^-, \end{aligned} \right\} \quad (24)$$

where R_n^+ , r and S_n^+ , r are the so-called total polar members [8], corresponding to the n -th pole of partial amplitudes of f^+ and the r -th pole of f^- ,

$$\left. \begin{aligned} R_n^+ &= \frac{r_n}{k} \left[-\frac{1}{2\sqrt{2}} \left\{ \int_{-\infty}^{\xi} \frac{e^{\lambda_n x} \operatorname{sh} x}{(\operatorname{ch} x - z)^{3/2}} dx + \right. \right. \\ &\quad \left. \left. + \int_{-\infty}^{\xi} \frac{e^{\lambda_n x} dx}{(\operatorname{ch} x - z)^{1/2}} \right\} + \frac{\pi(\alpha_n + 1)}{\cos \pi \lambda_n} P_{\alpha_n}(-z) \right]; \\ R_r^- &= \frac{r_r}{k} \left[-\frac{1}{2\sqrt{2}} \left\{ \int_{-\infty}^{\xi} \frac{e^{\lambda_r x} \operatorname{sh} x}{(\operatorname{ch} x - z)^{3/2}} dx - \right. \right. \\ &\quad \left. \left. - \int_{-\infty}^{\xi} \frac{e^{\lambda_r x} dx}{(\operatorname{ch} x - z)^{1/2}} \right\} + \frac{\pi \alpha_r}{\cos \pi \lambda_r} P_{\alpha_r}(-z) \right]; \\ S_n^+ &= \frac{ir_n}{k} \left[\frac{\sqrt{1-z^2}}{2\sqrt{2}} \int_{-\infty}^{\xi} \frac{e^{\lambda_n x} dx}{(\operatorname{ch} x - z)^{1/2}} + \frac{\pi P_{\alpha_n}^1(-z)}{\sin \pi \alpha_r} \right] \\ S_r^- &= \frac{ir_r}{k} \left[\frac{\sqrt{1-z^2}}{2\sqrt{2}} \int_{-\infty}^{\xi} \frac{e^{\lambda_r x} dx}{(\operatorname{ch} x - z)^{1/2}} + \frac{\pi P_{\alpha_r}^1(-z)}{\sin \pi \alpha_r} \right] \end{aligned} \right\} \quad (25)$$

Here $\lambda_{n,r} = \alpha_{n,r} + 1/2$, $\alpha_{n,r}$ is the position of the pole f^{\pm} , and $r_{n,r}$ are the residues in poles of f^{\pm} , $z \equiv \cos \vartheta$. Assume that one of the poles of α_i^+ approached close to the real axis. Then, reasoning similarly to the foregoing, A and B may be put in the form

$$\left. \begin{aligned} A &= \frac{r_l}{k} \left[-\frac{l+1}{v} P_l - P_l - (l+1) R_l - (l+1) \times \right. \\ &\quad \left. \times S_l(\xi, z) + o(v) \right]; \\ B &= \frac{ir_l}{k} \left[\frac{P_l^1}{v} - R_l^1 + S_l^1(\xi, z) + o(v) \right]. \end{aligned} \right\} \quad (26)$$

Here

$$S_l = \frac{1}{(l+1)} \cdot \frac{1}{2\sqrt{2}} \left[\int_{-\infty}^{\xi} \frac{e^{(l+1/2)x} \operatorname{sh} x}{(\operatorname{ch} x - z)^{3/2}} dx + \right. \\ \left. + \int_{-\infty}^{\xi} \frac{e^{(l+1/2)x} dx}{(\operatorname{ch} x - z)^{1/2}} \right]; \\ S_l^1 = \frac{\sqrt{1-z^2}}{2\sqrt{2}} \int_{-\infty}^{\xi} \frac{e^{(l+1/2)x}}{(\operatorname{ch} x - z)^{3/2}} dx; \quad (27)$$

$$R_l^1 = (-)^{l+1} \frac{\partial P_a^1(-z)}{\partial a} \Big|_{a=l}. \quad (28)$$

The functions of R_l^1 are derived from $R_l(z)$ on the basis of the relation /60

$$R_l^1(z) = -\sin \vartheta \frac{dR_l(z)}{dz}, \quad (29)$$

of function

$$S_l = P_l \ln \frac{\sqrt{e^{2\xi} - 2e^\xi z + 1} + e^\xi - z}{2} + W_l, \quad (30)$$

where P_l is a Legendre polynomial, and W_l satisfies the recurrent relation

$$(l+1)W_{l+1} - z(2l+1)W_l + lW_{l-1} = z \frac{e^{(l+1/2)\xi}}{[2(\operatorname{ch} \xi - z)]^{1/2}} - \\ - \frac{(l+1)}{(l+2)} \cdot \frac{e^{(l+3/2)\xi}}{[2(\operatorname{ch} \xi - z)]^{1/2}}; \quad (31)$$

$$W_0 = -\frac{e^{\xi/2}}{[2(\operatorname{ch} \xi - z)]^{1/2}}; W_1 = \frac{e^{-\xi/2}(1 - e^{2\xi})}{[2(\operatorname{ch} \xi - z)]^{1/2}} - 1. \quad (32)$$

For narrow resonance, as before, the principal members in the amplitudes of (26) assume the Breit-Wigner form

$$A = -\frac{(l+1)}{k} \frac{\Gamma_+}{E_1 - E_0 + i \frac{\Gamma_+}{2}} P_l(z); \\ B = \frac{i}{k} \cdot \frac{\Gamma_+}{E - E_0 + i \frac{\Gamma_+}{2}} P_l^1(z). \quad (33)$$

The terms of R_l , R_l^1 , S_l , S_l^1 in (26) have no analogs in the common theory of resonance reactions. First, they lead to definite deviations in angular distributions when compared with the simple Breit-Wigner formula, and, secondly, the complexity of the angular moment of resonance level causes polarization to appear, while polarization according to the Breit-Wigner formulas of (33) is equal to zero and occurs only as a result of interference with non-resonance partial amplitudes.

The polar amplitudes of (26) remain finite when $z = 1$ (forward scattering), and their partial amplitudes behave as l increases in such a manner that a partial amplitude with a parity corresponding to resonance parity decreases exponentially as l increases, and a partial amplitude of opposite parity is equal to zero for all l . We can prove that

/61

$$f_l^+ = -r_l \frac{e^{(\alpha-l)\xi}}{\alpha-l} \rightarrow r_l \frac{e^{-l\xi}}{l}, \quad l \rightarrow \infty \quad (34)$$

$$f_l^- = 0,$$

i.e., the Regge poles with a definite parity cannot generate partial amplitudes of opposite parity. In connection with this we may note that phase analysis of πN -scattering in the range of $3/2$ - $3/2$ resonance carried out by V. G. Zinov et al [10] indicates that the phase $P_{1/2}$ near resonance does not exceed 2° , while the resonance $P_{3/2}$ -phase is of the order of 90° , and the $S_{3/2}$ -phase is of the order of 20° , which agrees qualitatively with the requirements of the Khuri model (it permits an exponential smallness of non-resonance phases having a parity opposite to resonance phase). We shall not concern ourselves in this paper with the problem of applying the Regge-pole approach to resonances in the relativistic range, but this problem is undoubtedly of interest [9]. We may note yet another property of polar amplitudes in the Khuri concept [8]. In the purely polar approach, as was indicated in [11], the relations of unitarity in the elastic range makes it possible to relate the residue in the Regge pole to the position of the pole $r_1 = i m v$. In the Khuri concept, as can be easily seen from (34), such a relation is observed with an accuracy to terms of the order of v^2

$$r_l = i m v + o(v^2). \quad (35)$$

If in (24) we ignore the contributions of all poles except the main one, the differential cross-section and polarization of particles occurring in a resonance reaction have the form (the particles are not polarized in the initial state)

$$\begin{aligned} \frac{ds}{d\Omega} = \frac{|r_l|^2}{K^2 |v|^2} \{ & (l+1)^2 (P_l)^2 + (P_l^1)^2 + 2 \operatorname{Re} v [(l+1) (P_l)^2 + \\ & + (l+1)^2 P_l \mathcal{R}_l + P_l^1 \mathcal{R}_l^1] \} + o(v^2); \end{aligned} \quad (36)$$

$$\begin{aligned} P &= n \left(\frac{dz}{d\Omega} \right)^{-1} \cdot 2 \operatorname{Re} (AB^*) = \\ &= n \cdot 2 \operatorname{Im} v \left\{ \frac{(l+1) (P_l \mathcal{R}_l^1 - \mathcal{R}_l P_l^1) - P_l P_l^1}{(l+1)^2 (P_l)^2 + (P_l^1)^2} \right\} + o(v^2). \end{aligned} \quad (37)$$

In (36) and (37) we introduce the notation

/62

$$R_l + S_l = \mathcal{R}_l; \quad (38)$$

$$R_l^1 + S_l^1 = \mathcal{R}_l^1. \quad (39)$$

In the simplest cases $l = 0$ and 1 in accordance with the results of [9] and (27)-(32)

$$\mathcal{R}_0 = \ln \frac{\sqrt{R} + \beta - z}{2} - \frac{e^{\xi/2}}{[2(\operatorname{ch} \xi - z)]^{1/2}}; \quad (40)$$

$$\mathcal{R}_0^1 = \sin \vartheta \frac{\sqrt{R} + \beta}{\sqrt{R}(\sqrt{R} + \beta - z)}; \quad (41)$$

$$\mathcal{R}_1 = z \ln \frac{\sqrt{R} + \beta - z}{2} + z + \frac{e^{-\xi/2} - e^{\xi/2}}{[2(\operatorname{ch} \xi - z)]^{1/2}}; \quad (42)$$

$$\begin{aligned} \mathcal{R}_1^1 &= -\sin \vartheta \left\{ \ln \frac{\sqrt{R} + \beta - z}{2} + z \frac{\sqrt{R} + \beta}{\sqrt{R}(\sqrt{R} + \beta - z)} + 1 + \right. \\ &\quad \left. + \frac{e^{-\xi/2}}{[2(\operatorname{ch} \xi - z)]^{1/2}} \right\} \end{aligned} \quad (43)$$

and (36) and (37) assume the form:

a) $l = 0$

$$\begin{aligned} \frac{d\sigma}{d\Omega} &= \frac{|r_l|^2}{k^2 |v|^2} \left[\left\{ 1 + \ln \frac{\sqrt{R} + \beta - z}{2} - \frac{e^{\xi/2}}{[2(\operatorname{ch} \xi - z)]^{1/2}} \right\} \times \right. \\ &\quad \left. \times 2 \operatorname{Re} v + 1 \right]; \end{aligned} \quad (44)$$

$$P' = 2n \operatorname{Im} v \cdot \sin \vartheta \frac{\sqrt{R} + \beta}{\sqrt{R}(\sqrt{R} + \beta - z)}; \quad (45)$$

b) $l = 1$

$$\frac{d\sigma}{d\Omega} = \frac{|r_l|^2}{k^2 |v|^2} \left\{ 1 - 3z^2 + 2\operatorname{Re} v \left[7z^2 - 1 + (5z^2 - 1) \ln \frac{\sqrt{R} + \beta - z}{2} + \right. \right. \\ \left. \left. + (z^2 - 1) \frac{e^{-\xi/2}}{[2(\operatorname{ch} \xi - z)]^{1/2}} + 4z \frac{e^{-\xi/2} - e^{\xi/2}}{[2(\operatorname{ch} \xi - z)]^{1/2}} - (1 - z^2) \times \right. \right. \\ \left. \left. \times \frac{(\sqrt{R} + \beta)z}{\sqrt{R}(\sqrt{R} + \beta - z)} \right] \right\}; \quad (46)$$

$$P' = 2n \operatorname{Im} v \cdot \sin \vartheta \frac{1}{1 - 3z^2} \left\{ 2(1 - z) \frac{e^{-\xi/2}}{[2(\operatorname{ch} \xi - z)]^{1/2}} - \right. \\ \left. - \frac{z^2(\sqrt{R} + \beta)}{\sqrt{R}(\sqrt{R} + \beta - z)} - \frac{e^{\xi/2}}{[2(\operatorname{ch} \xi - z)]^{1/2}} \right\}. \quad (47)$$

In (43)-(47) we introduce the notations

/63

$$R = \beta^2 - 2\beta z + 1, \text{ where } \beta = e^{\xi}. \quad (48)$$

Formulas (36) and (37) predict the deviations of angular distribution from the simple form

$$\frac{d\sigma}{d\Omega} \sim [(l+1)^2 (P_l)^2 + (P_l')^2]$$

and the polarization of P' from zero, which occurs in a purely Breit-Wigner case. Comparison of (36) and (37) with the experiment would make it possible to determine both the real and imaginary parts of the position of the Regge pole in the energy range within the resonance region, which in the case of spinless particles would not be possible without phase analysis if one of the interacting particles is neutral. Nevertheless we can obtain information about the imaginary and real parts of the position of the Regge pole without Coulomb interaction, analyzing the scattering phases as this is done for spinless particles in [1] and for particles with spins of 0 and 1/2 in [4]. Experimental measurement of the polarization of secondary particles could be done by the direct method of checking the single-pole mechanism of resonance reactions, since (37) predicts the angular path of polarization. The absolute value of polarization may be quite discernible, if the imaginary part of the position of the Regge pole is sufficiently high. If $\operatorname{Im} v \sim 0.1$, then, according to (37), polarization may attain several tens of percents. More fruitful possibilities occur if the primary particles are polarized. In this case the angular distribution of the particles may be written thusly

$$\frac{d\sigma}{d\Omega} = |A|^2 + |B|^2 + 2\operatorname{Re}(AB^*) nP = \\ = \frac{|r_l|^2}{k^2 |v|^2} [(l+1)^2 (P_l)^2 + (P_l')^2 + 2\operatorname{Re} v [(l+1)(P_l)^2 + (l+1)^2 \times \\ \times P_l \mathcal{R}_l + P_l' \mathcal{R}_l'] + 2\operatorname{Im} v [(l+1)(P_l \mathcal{R}_l' - P_l' \mathcal{R}_l) - P_l P_l'] \cdot nP]; \quad (49)$$

$$\begin{aligned}
\mathbf{P}' = & \left(\frac{d\tau}{d\Omega} \right)^{-1} \frac{|r_i|^2}{K^2 |r_i|^2} \{ [(l+1)^2 (P_l)^2 - (P_l^1)^2 + 2 \operatorname{Re} \nu [(l+1) (P_l)^2 + \\
& + (l+1)^2 \mathcal{R}_l P_l - P_l^1 \mathcal{R}_l^1] \cdot \mathbf{P} + 2 [(P_l^1)^2 + 2 \operatorname{Re} \nu P_l^1 \mathcal{R}_l^1] n(n\mathbf{P}) + \\
& + 2 [(l+1) P_l P_l^1 + \operatorname{Re} \nu (P_l P_l^1 + P_l^1 \mathcal{R}_l + P_l \mathcal{R}_l^1)] [n\mathbf{P}] + \\
& + 2 \operatorname{Im} \nu [(l+1) (P_l \mathcal{R}_l^1 - \mathcal{R}_l P_l^1) - P_l P_l^1] n \}.
\end{aligned} \quad (50)$$

5. Calculation of Coulomb Interaction at Scattering Resonance of Charged Particles

We can present the scattering amplitude of charged spinless particles in the form

$$f(E, z) = \frac{1}{2ik} \sum_{n=0}^{\infty} (2n+1) e^{i\sigma_n} P_n(z) = f^c + f^N, \quad (51)$$

where

$$f^c = \frac{1}{2ik} \sum_{n=0}^{\infty} (2n+1) e^{2i\sigma_n} P_n(z) = \frac{C(\eta)}{k(1-z)^{1+i\eta}}; \quad (52)$$

$$\eta = \frac{z_1 z_2 e^2}{h\nu} \text{ --- is the Coulomb parameter,}$$

$$e^{2i\sigma_n} = \Gamma(n+1+i\eta)/\Gamma(n+1-i\eta); \quad C(\eta) = -\eta 2^{i\eta} e^{2i\sigma_0}; \quad (53)$$

$$f^N = \frac{1}{k} \sum_{n=0}^{\infty} (2n+1) e^{2i\sigma_n} f_n^N P_n(z); \quad f_n^N = e^{i\delta_n} \sin \delta_n. \quad (53a)$$

Because the Coulomb partial amplitude is limited when $|\lambda| \rightarrow \infty$ and has no peculiarities in the right-half plane of λ when $E > 0$, resonances during scattering of charged particles are determined by the poles of E and nuclear amplitudes $f_n^N(E)$.

We know [2] that if the functions of $f_i(z)$ ($i = 1, 2, 3$) are expanded into series according to Legendre polynomials

$$f_i(z) = \sum_{n=0}^{\infty} (2n+1) a_n^{(i)} P_n(z) \quad (54)$$

such that $a_n^{(3)} = a_n^{(1)} a_n^{(2)}$, then

$$f_3(z) = f_3(n_1 n_2) = \frac{1}{4\pi} \int f_1(n_1 n) f_2(n_2 n) d\Omega_n, \quad (55)$$

where n_1 , n_2 , and n_3 are unit vectors, $d\Omega_n = \sin \vartheta d\vartheta d\phi$. Let us take as f_1 the function

$$\tilde{f}^N(E, z) = \sum_{n=0}^{\infty} (2n+1) f_n^N P_n(z), \quad (56)$$

which can be presented in the form of (11). Let us take the Coulomb amplitude f^C (52) as $f_2(z')$. Using relation (55), we write f^N as

/65

$$f^N = \sum_{n=1}^{\infty} \frac{1}{4\pi} \int R(s; n_1 n_2 \lambda_n) f^C(n_2, n) d\Omega_n, \quad (57)$$

where R is determined by (11).

In the case when the main role in the amplitude of f^N is played by the pole approaching the real axis, it may be written in the form

$$f^N = r_l \left[-\frac{2l+1}{v} P_l^C(z) - P_l^C(z) - (2l+1) R_l^C(z) - S_l^C(\xi, z) + o(v) \right] \quad (58)$$

Here

$$P_l^C = e^{i\vartheta l} P_l; R_l^C = (-1)^l e^{-2i\vartheta l} \left[\frac{\partial P_l^C(-z)}{\partial \lambda} \right] \Big|_{\lambda=l}; \quad (59)$$

$$P_\lambda^C(z) = \frac{ik}{2\pi} \int P_\lambda(n_1, n) f^C(n_2, n) d\Omega_n = \frac{iC(\eta)}{2\pi} \int_{-1}^1 dz' \int_0^{2\pi} \times \quad (60)$$

$$\times \frac{d\varphi}{(1-z')^{1+i\eta}} P_\lambda(z z' + [(1-z^2)(1-z'^2)]^{1/2} \cos \varphi);$$

$$S_\lambda^C = \frac{iC(\eta)}{2\sqrt{2}\pi} \int_{-1}^1 dz' \int_0^{2\pi} d\varphi \int_{-\infty}^{\xi} \times \quad (61)$$

$$\times \frac{e^{\lambda n^x \operatorname{sh} x dx}}{(1-z')^{1+i\eta} (\operatorname{ch} x - z z' [(1-z^2)(1-z'^2)]^{1/2} \cos \varphi)^{3/2}}.$$

The functions of $P_\lambda^C(z)$ and $S_\lambda^C(z)$ are not expressed in the form of a finite combination of elementary functions and require numerical integration. The differential cross-section of resonance scattering of charged particles has the form $d\sigma/d\Omega = |f^C + f^N|^2$ with f^N from (58). We may note that if the differential cross-section during scattering of the charged particles is determined only by the real part of the pole position, we can determine both the real and imaginary parts of the pole position by measuring the differential scattering cross-section of the charged particles.

It is obvious from what has been said that in the case of the scattering of charged particles having a spin, polar nuclear scattering amplitude of $f^N = A + \sigma nB$, where A and B are similar to those written in (26) with substitution of $P_l^c, -R_l^c, S_l^c, S_l^1, R_l^1$ and P_l^1 for $P_l^c, R_l^c, R_l^1, P_l^1, S_l^c, S_l^1, P_l^1$ and R_l^1 are related to R_l^c and P_l^c by relations similar to those of (29), and

$$S_l^1 = \frac{\sin \delta C(\eta)}{2\sqrt{2}} \int_{-1}^1 \frac{dz'}{(1-z')^{1+l\eta}} \int_0^{2\pi} d\varphi \times$$

$$\times \int_{-\infty}^{\xi} \frac{e^{(l+1/2)x} dx}{(\operatorname{ch} x - zz' [(1-z^2)(1-z'^2)]^{1/2} \cos \varphi)^{3/2}}. \quad (62)$$

The differential scattering cross-section and polarization of charged particles having a spin is given by the expression

$$\frac{d\sigma}{d\Omega} = |f^c + f^N|^2; \quad (63)$$

$$P' = \frac{2 \operatorname{Re} [(f^c + A) B^*]}{\frac{d\sigma}{d\Omega}} n. \quad (64)$$

When writing expressions (63)-(64) we assumed that we could ignore spin-orbital forces in a Coulomb amplitude in a non-relativistic case.

6. The Relationship of the Regge Pole Position with Phase Shifts

In those cases when a phase analysis is conducted of experimental data on a resonance nuclear reaction, it is feasible to use the relation of the Regge partial amplitude with the phase shifts derived from the experiment in order to find the trajectory of the resonating Regge pole and to verify the Regge character of the resonance.

In order to obtain these relations, we shall proceed on the basis of (18), (34) and (35). We obtain from these formulas with an accuracy to terms of the order of v^2 the relationship of the resonance scattering phase with the parameters of the Regge pole trajectory in the energy range close to resonance

$$\cotan \delta_{\text{res}} = -\frac{\operatorname{Re} v}{\operatorname{Im} v}. \quad (65)$$

For non-resonance phases with the same accuracy, we have

$$\cotan \delta_l = -\operatorname{Im} v \left(\frac{1}{n} - \frac{\operatorname{Re} v}{n^2} - \xi \right), \quad (66)$$

where $n = (l_{\text{res}} - l)$.

We can determine the trajectory of the resonating Regge pole with the help of (65) and (66) and by using the part of scattering phases known from experience. Knowing the parameters of the Regge pole ($\text{Im}\nu$ and $\text{Re}\nu$), we can now calculate the remaining scattering phases in the energy range close to resonance. /67 Comparison of the phases calculated with those found from phase analysis would permit us to directly verify the Regge character of the resonance being studied, as well as to establish real limits of applicability of the single-pole model. We note in conclusion that the phases considered here are the so-called "nuclear" phase shifts δ_{ℓ}^N , which do not contain the Coulomb interaction. Relations (65) and (66) are valid both in the case of interaction of spinless particles and in the case of the interaction of particles with spins of 0 and 1/2. As has been noted already, the single-pole approach in the Khuri concept does not permit calculation of the scattering phase in states with a parity opposite that of resonance. Such a possibility occurs only upon calculation of several poles having different parity.

7. Application of the Khuri Method to Resonance Scattering of α -Particles and Protons and C^{12} Nuclei

Let us apply the Khuri method [8] to resonance scattering of α -particles in C^{12} nuclei near a resonance of 1^+ . Experimental data on this reaction are contained in [7], where the first five nuclear scattering phases were determined (this renders calculation of the Coulomb interaction superfluous, because we can compare purely nuclear amplitudes).

Comparing the expressions for nuclear scattering amplitudes, resulting from phase analysis [12]

$$f_{\text{ph}} = \frac{1}{2ik} [(e^{2i\delta_0} - 1) + 3z(e^{2i\delta_1} - 1) + \frac{7}{2}(5z^3 - 3z)(e^{2i\delta_3} - 1)] \quad (67)$$

and from the Khuri method

$$f_x = \frac{1}{2ik} r_{1+} [(2l+1)P_l + \nu(2P_l + (2l+1)\mathcal{R}_l)] = \frac{1}{2ik} \times \\ \times r_{1+} \left[3z + \nu \left(3z \ln \frac{\sqrt{R} + \beta - z}{2} + \frac{3(\beta - r)}{\beta - 1} + 5z + \frac{\beta^2 - 6\beta + 3}{\sqrt{R}} \right) \right], \quad (68)$$

we can obtain the trajectories $\text{Re}\nu$ and $\text{Im}\nu$ of the Regge pole in the resonance region of 1^+ . Numerical results are presented in Figure 2. The figure also contains the results obtained for this case in [1, 3] with the use of polar amplitudes in the Regge form. Qualitative agreement between all papers is good, but correct calculation of the right cross-section of scattering amplitude in the plane z leads to the fact that the trajectory of the pole presses closely against the real axis and, subsequently, describes the process over a wider energy range.

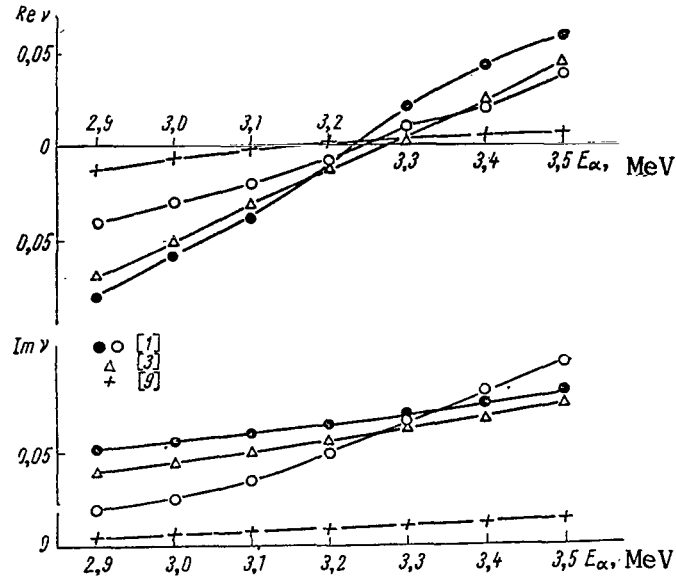


Figure 2. Trajectories of a Regge Pole Near a Resonance of 1^+ of a C^{12} Nucleus.

Expressions (67) and (68) were equated at different values of the cosign of scattering angle z , but at identical energy. We determined $Re\nu$, $Im\nu$ and ξ from the set of equations obtained in such a manner that the value $\sqrt{\frac{|f_{ph}|^2 - |f_x|^2}{|f_{ph}|^2}}$ /68

did not exceed 0.01. In order to check the correctness of the values of $Re\nu$, $Im\nu$, and ξ obtained, they were substituted into expression (68) and the amplitudes of (67) and (68) were compared for other values of z . It turned out that

the value of $\sqrt{\frac{|f_{ph}|^2 - |f_x|^2}{|f_{ph}|^2}}$ did not exceed 0.02, at any values of z . $Re\nu$ and

$Im\nu$ were found corresponding to energies of an α -particle from 2.9 to 3.5 MeV through 0.1 MeV. The value of ξ , which determined the beginning of the cross-section in the Z -plane of scattering amplitude, was equal to $\xi = 0.08$. On the other hand, we can determine the position of peculiarity on the basis of considering the triangular diagram of Figure 3. The method of determining the beginning of anomalous peculiarities caused by the triangular diagrams was worked out in [13]. In accordance with the results of this paper the value of ξ is expressed for Figure 3 by formula

$$\operatorname{ch} \xi = 1 + \frac{(M_{C^{12}} + M_\alpha) m_{B^{10}} m_d' (m_{B^{10}} + m_d - M_{C^{12}})}{2 (m_{B^{10}} + m_d) M_\alpha (E_{C^{12}} + E_\alpha^*)}, \quad (69)$$

where M and m are the masses of corresponding particles, and E is their energies. /69 We obtain a value $\xi = 0.10$ for the diagram of Figure 3 closely corresponding with that of the experiment.

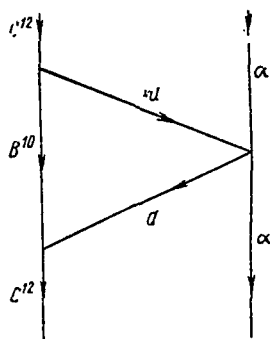


Figure 3. A Diagram Determining the Cross-Section Position of Scattering Amplitude of α -Particles in a C^{12} Nucleus in a Complex Z-Plane.

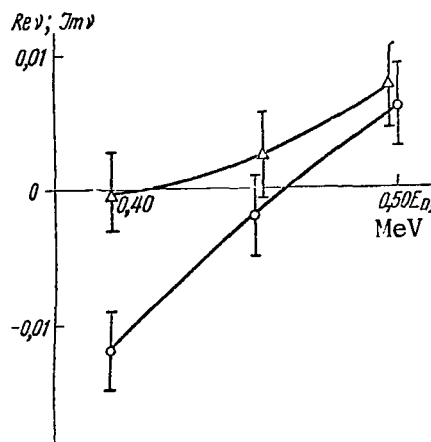


Figure 4. The Trajectory of a Regge Pole Near a Resonance of $1/2^+$ of a C^{12} Nucleus:

○ — $Re v$;
△ — $Im v$.

Besides analysis of elastic resonance scattering of α -particles in C^{12} nuclei, we also attempted to analyze the results of proton scattering in a C^{12} nucleus near a resonance of $1/2^+$.

Experimental data on this scattering are contained in [14], where the relations of scattering cross-section P in a C^{12} nucleus are determined according to a purely Coulomb interaction for scattering angles from 30 to 160° in a center of mass system near a resonance of $1/2^+$ with an accuracy to 0.02 . We calculated Coulomb interaction in this case because there was no phase analysis. $Re v$ and $Im v$ were determined by the methods similar to that described above with an accuracy to 0.005 for proton energies equal to 0.40 , 0.45 and 0.50 MeV. The trajectories of $Re v$ and $Im v$ obtained are given in Figure 4. The qualitative behavior of the trajectories is the same as in the previous case. Unfortunately, the possibility of experimental data in this case does not permit us a more detailed analysis and verification of the stability of $Re v$ and $Im v$ obtained by different methods.

8. Conclusion

Analysis of the amplitude of resonance nuclear scattering conducted in this article indicates that the theory of complex moments, even in its simplest single-pole form, may lay claim to a more complete description of resonance nuclear reactions than the simple Breit-Wigner model. Processing of the experimental data on resonance scattering of α -particles in C^{12} nuclei on the basis of the new method indicates that this process is fully described in practice by two parameters of $Re v$ and $Im v$ (instead of five phases in the phase analysis method). These parameters are stable, i.e., they are hardly dependent on the method of their determination. Moreover, variation of the parameter of ξ , which determines the position of amplitude cross-section in plane z , led to a

/70

value of ξ close to the theoretical value. All these results prove the usefulness of the method of complex moments. However, there are very few good experimental data at present. There are hardly any data on polarization of secondary particles in resonance nuclear reactions. We should like very much to obtain such data (along with data on the angular distributions of secondary particles), since these data make it possible to verify directly the applicability of the Regge pole concept to resonance nuclear reactions.

The authors are grateful to V. M. Galitskiy, E. I. Dolinskiy and V. S. Popov for discussion of problems touched on in this article.

REFERENCES

1. Popov, V. S. and E. I. Dolinskiy, *Zh. Eksperim. i Teor. Fiz.*, Vol. 46, p. 970, 1964.
2. Popov, V. S. and E. I. Dolinskiy, *Zh. Eksperim. i Teor. Fiz.*, Vol. 47, p. 697, 1964.
3. Pebolia, L. and G. A. Viano, *Nuovo cimento*, Vol. 26, p. 1426, 1962.
4. Regnier, J., *Nucl. Phys.*, Vol. 54, p. 225, 1964.
5. Regge, T., *Nuovo cimento*, Vol. 14, p. 951, 1959.
6. Regge, T., *Nuovo cimento*, Vol. 18, p. 957, 1959.
7. Jones, M. et al, *Nucl. Phys.*, Vol. 37, p. 1, 1963.
8. Khuri, N. N., *Phys. Rev.*, Vol. 130, p. 427, 1960.
9. Khuri, N. N. and B. M. Udgaonkar, *Phys. Rev. Lett.*, Vol. 10, p. 172, 1963.
10. Grushin, V. V. and Yu. P. Nikitin, *Yaderniya Fizika*, Vol. 5N, p. 1, 1967.
11. Ziniv, V. G. et al, *Zh. Eksperim. i Teor. Fiz.*, Vol. 38, p. 1407, 1960.
12. Gribov, V. N., "Lectures on the Quantum Field Theory", *Preprint of ITEP*, 1962.
13. Blankenbecler, R. et al, *Ann. Phys.*, Vol. 10, p. 62, 1960.
14. Blokhintsev, D. I., E. I. Dolinskiy and V. S. Popov, *Nucl. Phys.*, Vol. 40, p. 117, 1963.
15. Milne, E. A., *Phys. Rev.*, Vol. 93, p. 765, 1954.

A UNIVERSAL METHOD OF PROCESSING THE TRACKS OF ARBITRARY CURVATURE ON BUBBLE CHAMBER TRACKS

K. N. Mukhin, A. S. Romantseva, I. A. Svetlologov, M. M.
Sulkovskaya, S. A. Chuyeva and R. S. Shlyapnikov

ABSTRACT. This article presents a universal method of calculating the tracks of charged particles in bubble chambers. The data base for such calculations are the coordinates of a number of points of the track being studied, measured on special devices. The track is approximated by the segment of a helicoid, but such approximation is completely valid only when there are no energy losses by the charged particle. The problem is often further simplified by projecting the track onto a plane normal to the vector of magnetic field intensity, such projection being approximated by a Parabola. This approximation is sufficiently accurate only when considering the arcs of a circle small in comparison with the radius. The method proposed in this paper is suitable to determine the parameters of a track of variable and arbitrarily large curvature over the entire energy range and length measured.

1. Introduction

Calculating methods using an electronic computer (EVM) are presently used to determine the parameters of tracks of charged particles in tracking devices. The coordinates of a number of points of the track under study, measured on special devices, comprise the principal aggregate of data for such calculation. /71

The basis of most calculating methods is to find the space curve of a given type which approximates the track and which satisfies in the best manners the initial aggregate of the coordinates of points measured. Approximating the track by a segment of a helicoid is most often used for tracking devices placed in a uniform magnetic field. Such approximation is completely valid only when there are no energy losses of the charged particle. Additional simplification of the problem is often done in practical variants, which include the fact that projection of a track onto a plane normal to the vector of magnetic field intensity is approximated by Parabola. This additional approximation is valid with sufficient accuracy only when considering the arcs of a circle which are small when compared with the radius.

Use of the indicated approximations in bubble chambers with a light-weight filling and a weak magnetic field intensity is justified over a wide energy range of particles. However, the range of applicability of the indicated approximations is very limited for chambers with a heavy filling and a strong magnetic field intensity. A calculating technique which takes into consideration the particle energy losses in a substance is required to investigate particle tracks in this case. It is very desirable to preserve the universality of the method and its maximum calculating efficiency.

The method presented in this paper is suitable for determining the track parameters of variable and arbitrarily large curvature over the entire energy range and length measured.

2. The Principal Fundamentals of the Calculating Method

In order to investigate the possible ways of determining the track parameters of charged particles in a magnetic field when there are ionization losses, let us compare the motion which defines the trajectory of a particle in this case:

/72

$$\frac{dp}{dt} = \frac{1}{E} [pH] - \frac{dp}{ds} \cdot \frac{p}{E}. \quad (1)$$

Ionization deceleration is calculated by the term $dp/ds \cdot p/e$. When integrating this equation it is convenient to convert to the variable s as a parameter. Solution of the equation yields the following expression for the particle trajectory in Cartesian coordinates x , y , and z :

$$\left. \begin{aligned} x &= \sin \theta \int_0^s \left[\cos H \int_0^s \frac{ds}{p(s)} \right] ds; \\ y &= -\sin \theta \int_0^s \left[\sin H \int_0^s \frac{ds}{p(s)} \right] ds; \\ z &= s \cos \theta^2. \end{aligned} \right\} \quad (2)$$

It follows from expression (2) that the particle trajectory in a general case is a spatial spiral untwisted from the point where the particle stops and coiled at a constant angle onto the lines of force of the magnetic field. At known values of $p(s)$, H , θ , s , expression (2) makes it possible to calculate all the required track parameters at a given point.

In practice the segment of particle trajectory not containing its point of stopping is usually measured in a known field H . Thus, the problem of finding the parameters of a particle track results in determining the position of the trajectory segment measured on the common trajectory described by expression (2). The initial aggregate of the data in this case is that of the space coordinates of a sequential series of points measured on a given segment in a specific system of calculation.

/73

¹ Here and in further presentation the charge of the electron in all cases is assumed to be $e = 1$ and the speed of light $c = 1$.

² The simplest form of solution is presented--the origin of the coordinates is located at the point where the particle stops; $z \parallel H$; θ is the angle between the axis of z and the particle tangent to the trajectory and is an arbitrary initial parameter.

When investigating the aggregate of tracks which generate selected events, there is usually a physical hypothesis determining the form of the particles generating the tracks, and, thus, the form of the function of $p(s)$ is predetermined. We shall henceforth consider the form of function $p(s)$ to be known for different particles-- $p_1(s)$, $p_2(s)$ and $p_3(s)$.

It is not possible to find the optimum values of the parameters of s_1 , s_2 and θ directly by the method of least squares due to the complexity of expression (2). One of the possible ways of overcoming this difficulty is to simplify the relations of (2), i.e., by approximating the trajectory by these simpler curves (for example, by the Helicoid already mentioned). However, this method always limits the area of applicability of the calculating method. Another possible method is to find instead of s_1 , s_2 and θ auxiliary values (clearly related to s_1 , s_2 and θ) which can be determined by a simple method according to the initial aggregate of the data.

We selected the following as auxiliary parameters-- Δs is the length of the arc of the measured track; Σ is the area of the curvilinear segment formed in the plane X, Y by projection of the track arc and which subtends its cord; Δz is the projection of the track onto axis Z^1 . Selection of these parameters is determined by the fact that their values may be obtained simply and with a sufficient degree of accuracy from measuring the coordinates of the track points without resorting to any approximation which predetermines the form of the particle trajectory.

Using expression (2), we obtain the following relations linking the parameters Δs , Δz , and Σ with parameters s_1 , s_2 and θ :

$$\left. \begin{aligned} \Delta z &= \Delta s \cos \theta; \\ \Delta s &= s_2 - s_1; \\ \Sigma &= \frac{\sin^2 \theta}{2} \left\{ \int_{s_2}^{s_1} \left[\cos \left(H \int_0^s \frac{ds^*}{p} \right) \cdot \int_0^s \sin \left(H \int_0^s \frac{ds}{p} \right) ds - \right. \right. \\ &\quad \left. \left. - \sin \left(H \int_0^s \frac{ds}{p} \right) \int_0^s \cos \left(H \int_0^s \frac{ds}{p} \right) ds \right] ds + \int_0^{s_2} \cos \left(H \int_0^s \frac{ds}{p} \right) \times \right. \\ &\quad \times ds \int_0^{s_1} \sin \left(H \int_0^s \frac{ds}{p} \right) ds - \int_0^{s_1} \cos \left(H \int_0^s \frac{ds}{p} \right) ds \times \\ &\quad \left. \times \int_0^{s_2} \sin \left(H \int_0^s \frac{ds}{p} \right) ds \right\}. \end{aligned} \right\} \quad (3)$$

¹We shall henceforth call the proposed method the area method in connection with using the area of the segment Σ as one of the parameters.

The equations of (3) provide the best opportunity to determine the values of θ , s_1 and s_2 from known values of parameters Δs , Σ and Δz . However, due to the complexity of equation (3) it is possible to obtain a clear expression for the values of s_1 and s_2 only by making simplifying assumptions. /74

Let us examine in particular to which relations the calculating method leads when there are no ionization losses. In this case we should assume $p(s) = \text{const} = p_0$ in expression (3). Integrating expression (3) we obtain:

$$\left. \begin{aligned} \Delta z &= \Delta s \cos \theta; \\ \Delta s &= s_2 - s_1; \\ \Sigma &= \frac{1}{2} \cdot \frac{p_0}{H} \sin^2 \theta \left(\Delta s - \frac{p_0}{H} \sin \frac{H}{p_0} \Delta s \right). \end{aligned} \right\} \quad (4)$$

It is apparent from expression (4) that the right number of the equation which determines Σ is the area of the segment with radius $R = p_0 \sin \theta / H$ and an arc length of track projection $L = \Delta s \sin \theta$ onto the plane X, Y.

Assuming $L \ll R$, we can simplify the expression for Σ , expanding it into a series to the first nonzero term:

$$\Sigma = \frac{\sin^2 \theta H \Delta s^3}{12 p_0} \quad (5)$$

or by introducing the trajectory length of arc $L = \Delta s \sin \theta$, we obtain

$$\Sigma = \frac{H L^3}{12 p_0 \sin \theta}. \quad (6)$$

We can clearly define from expression (6) $p_0 \sin \theta$ as the projection of the pulse in the plane X, Y:

$$p_0 \sin \theta = \frac{H L^3}{12 \Sigma}. \quad (7)$$

Let us consider how the approximation (7) corresponds to the approximation of the track projection by a Probala which is used under the conditions indicated. It is assumed in this case that $p_0 \sin \theta = HR$, where R is determined by the equation of the Probala approximating the track; the Probala has the form $y = Ax^2$, where $R = 1/2A$ in a simpler case of symmetrical distribution. If we express the value of R by the length of the Probala arc L and the area of its segment, we obtain $p_0 \sin \theta = \frac{H L^3}{12 \Sigma_{\text{par}}}$. Thus, both methods of calculation in this case lead to equivalent results.

3. Determination of Parameters Δs , Σ , Δz by Track Point Coordinates x , y and z

We determined the value of Δs as the sum of the cord lengths which subtend successive pairs of points /75

$$\Delta s = \sum_i \delta s_i. \quad (8)$$

When Δs is determined in this manner, the segments of partial arcs of the space curve of the track are approximated by the cords. It is obvious that this approximation leads to an underestimation of the value of Δs in the absence of experimental errors.

Let us estimate the systematic error when determining Δs . The small segment of the arc between two successive points may be considered to be a plane curve with a constant radius of curvature R . In this case the difference of the arc length Δs_{g_i} and of the cord Δs_{x_i} is determined in the first approximation by the expression

$$\Delta s_{g_i} - \Delta s_{x_i} \approx \frac{\Delta s_{g_i}^3}{24R_i^2}. \quad (9)$$

Assuming $\Delta s_i = \Delta s/n$ (uniform dissection), we obtain the following expression for total systematic error of $\delta(\Delta s)$:

$$\delta(\Delta s) = \frac{\Delta s^3}{24n^3} \sum \frac{1}{R_i^2} = \frac{\Delta s^3}{24n^2} \frac{1}{R^2}. \quad (10)$$

The relative error in determining Δs , and $\epsilon(\Delta s)$ will be equal to

$$\epsilon(\Delta s) = \frac{\Delta s^2}{24n^2} \cdot \frac{1}{R^2}. \quad (11)$$

Assuming that an order of ten points is placed on the track during the measurement and that the value of the arc measured $\Delta s \sim R$, we can estimate the systematic error $\epsilon(\Delta s)$. In this case it comprises a value of the order of 0.05%. We need not concern ourselves with a similar error in determining Δs , because other reasons lead to significantly larger errors.

We determine the value of Σ as the area of a polygon with its apexes at the measured points. Arranging the x axis in the direction of the cord which subtends the end points, it is easy to calculate the area indicated:

$$\Sigma = \frac{1}{2} \sum_i (y_i + y_{i+1})(x_{i+1} - x_i). \quad (12)$$

This approximation also leads to a systematic error--underestimation of the area measured in relation to the true area. Let us estimate the error which occurs. Considering the small segments of track projection as arcs of the circle, we obtain a segment of error in the form

/76

$$\delta \Sigma_i = \frac{Lx_i^3}{12R_i}. \quad (13)$$

Assuming $Lx_i = L/n$ (uniform dissection), we obtain

$$\delta \Sigma = \frac{L^3}{12n^2} \frac{1}{R}. \quad (14)$$

The relative error in Σ in the case where the trajectory is the circumference, is

$$\varepsilon(\Sigma) = \frac{L^3}{12n^2R} \cdot \frac{2}{LR \left(1 - \frac{R}{L} \sin \frac{L}{R}\right)}. \quad (15)$$

Estimating the value of $\varepsilon(\Sigma)$ and assuming, as in the previous case, that $L \approx R$ at a number of dissections $n \sim 10$, we obtain the value of relative error $\varepsilon(\Sigma) \sim 1\%$. Such a systematic error when determining Σ may be ignored in most cases.

We determine the value of Δz_i as the difference of successive values of the coordinates $\Delta z_i = z_i - z_1$.

Using the values of Δz_i determined in this manner and Δs_i corresponding to them, we can find $\cos \theta$ from the first equation of (3) by the method of least squares.

The described determination of parameters Δs , Σ , Δz by the initial aggregate of the data is thus derived from simple calculating formulas. It is extremely important that this does not place any limits on the values of the arc of the curve measured and its curvature. Systematic errors in determining the parameters in this case may be kept within specified limits by intelligent selection of a number of points to be measured on the track. However, in practice the coordinates of the initial aggregate of the points are distorted due to inaccuracy of measurements, multiple scattering and other reasons. The

values of parameters Δs , Σ and Δz obtained by the formulas indicated above will contain additional errors. Investigation of these errors is given in Section 6.

4. Logical Arrangement of the Program

A program was compiled on an electronic computer in order to calculate the parameters of tracks according to the method of areas described above. The initial part of the program, which includes calculation of space coordinates of the track point, length of the track Δs , angle θ and area Σ_{meas} , are not of particular interest. The basic part of the program consists of finding the parameters of s_1 and s_2 . The method of successive approximations, which includes the following, is used to determine them.

/77

We find the calculated value of the area of Σ_{theor} from (3) by numerical integration for the given angle of θ on the assumption that the measured section of the track corresponds to the particle at rest with a path of Δs ($s_1 = 0$ and $s_2 = \Delta s$). The values of Σ_{meas} and Σ_{theor} are compared. Because the particle at rest with a path of Δs describes the trajectory with the greatest segment area, $\Sigma_{\text{meas}} \leq \Sigma_{\text{theor}}$ with an accuracy to errors when determining Σ_{meas} . If $\Sigma_{\text{meas}} = \Sigma_{\text{theor}}$, the event measured actually corresponds to the particle at rest. The initial pulse at point s_2 is determined by the dependence $p(s)$. Function $p(s)$ used to calculate Σ_{theor} and p is fed into the computer in the form of a table of values of $p(s)$ at a series of points s . The intermediate values required to calculate this function are located by logarithmic interpolation between two given points. If $\Sigma_{\text{meas}} < \Sigma_{\text{theor}}$, the limits of integrating s_1 and s_2 in (3) with the constant step δs change successively:

$$s_{1i} = i\delta s; \quad s_{2i} = \Delta s + i\delta s. \quad (16)$$

The process of calculation is continued until the equality of $\Sigma_{\text{meas}} = \Sigma_{\text{theor}}$ is achieved. The pulses p_1 and p_2 are located at the beginning and end of the track when the values of s_1 and s_2 are determined in such a manner.

The value of $\delta s = 0.2$ cm in the program written, the step of integrating in (3) is constant and is equal to 0.2 cm. The function of $p(s)$ was given in the range $p = 0-400$ MeV/c by the table of values at eight points. The program occupies about 200 cells of the operation storage of a 3-address computer.

5. Experimental Verification of the Method

Verification of the proposed method is accomplished in the track of stopped π^+ -mesons, because this makes it possible to clearly identify π^+ -mesons by their decay and to determine the path of the pulse to stopping. The dependence of pulse on the value of the path $p(s)$ for protons of π^- and μ -mesons was

calculated by the method proposed in [1]. A section of the curve $p(s)$ for protons was constructed simultaneously for control of calculation on the basis of experimental measurements of the paths of stopped proton output during elastic interactions [2]. Proton energies were calculated according to reaction kinematics. Figure 1 depicts the calculated curves of $p(s)$. The broken line represents the section of the experimental curve calculated by the method of least squares on the basis of the measured paths of proton output, indicated in Figure 1 by the points. The solid lines inside which lie the section of the experimental curve limit the area of error equal to a single standard deviation. The close agreement of the calculated and experimental curves is obvious.

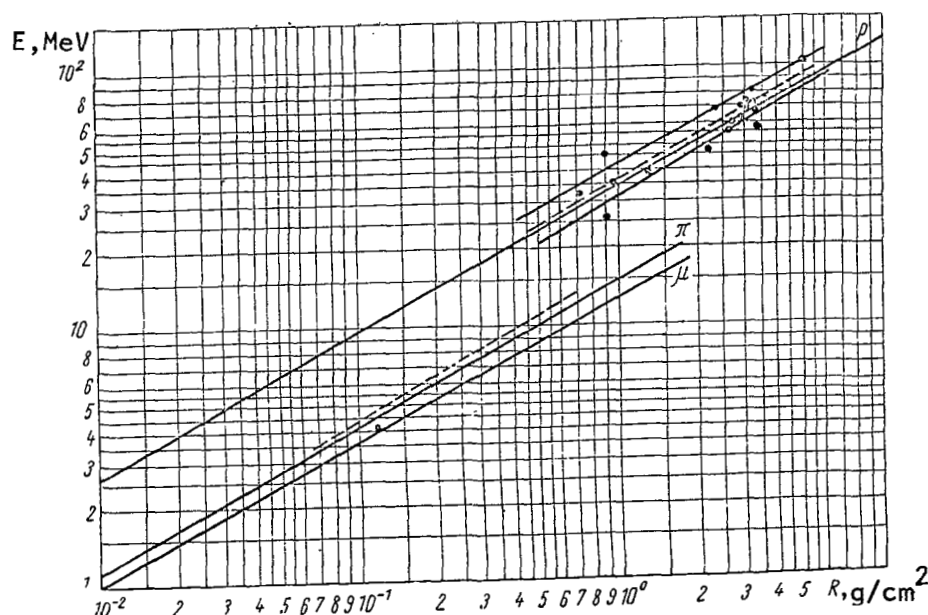


Figure 1.

For the selected cases of stopped π^+ -mesons, we calculated the pulse according to the described method of areas P_Σ , and also according to the method used earlier of approximating the trajectory by a parabola P_p . Such calculation was carried out for both the total path of P_Σ and for the part of the path (about one half) P_Σ , not including the stopping point. The values obtained were compared with that of pulse P_R which was determined from the value of the path. Figures 2 and 3 indicate the results of this comparison. It is obvious from the figures that the method used earlier gives an underestimated value of the pulse with a large value of spread relative to the pulse determined by the path.

The pulse found by the method of areas P_Σ (Figure 2) shows a much better agreement with the pulse of P_R . This indicates that the given method yields a

correct value of the pulse for tracks undergoing significant ionization deceleration. The least width of distribution represented in Figure 2 compared with that in Figure 3 indicates a lesser influence on the determined magnitude of the pulse of the factors which distort its value. Thus, use of the method of areas permits us to accurately determine the basic characteristics of the track.

/80

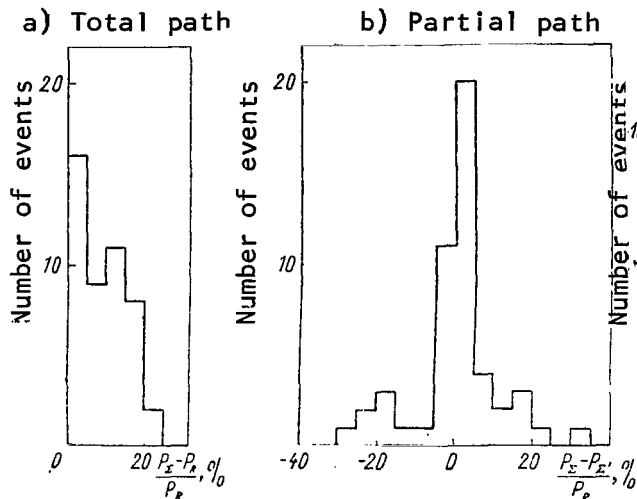


Figure 2.

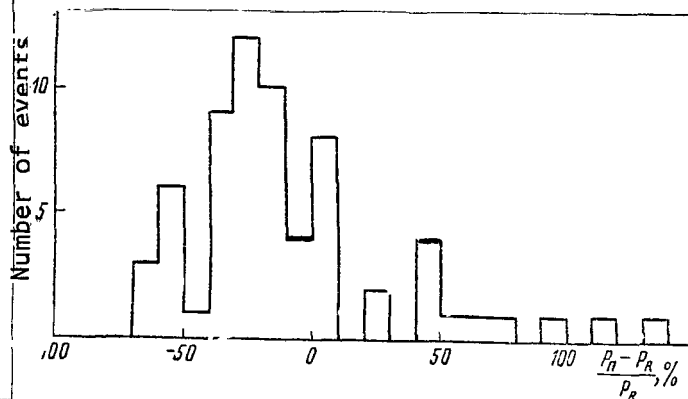


Figure 3.

6. Estimating Measurement Accuracy by the Method of Areas

The distribution presented in Figure 2 indicates a high average accuracy of finding the pulse. However, it is very important to determine the effect of separate factors on the accuracy of this pulse.

In general form the pulse determined by the method of areas is a function of several variables:

$$P_z = f[H, \sum_{\text{meas}} \Delta s, \theta, p(s)],$$

where H is the magnetic field intensity, \sum_{meas} is the measured area of the segment, Δs is the length of the track, θ is the angle formed by the tangent of the track with axis Z , and $p(s)$ is the curve of the pulse path.

Calculations were made in which the indicated parameters were subjected to numerical variation in order to study the effect of these factors on the value of pulse P_z .

The parameters of H and $p(s)$ are one of the basic parameters of calculation; moreover, their values are fed into the program beforehand. However, in practice the accuracy of determining these parameters is limited, which leads to errors in finding the pulse.

The pulse of the selected events for four values of H was calculated in order to determine the value of the error which occurs due to the inaccurate value of magnetic field intensity. Figure 4 shows the results of the calculation. Magnetic field intensity is plotted on the axis of the abscissas, and the value of relative deviation of pulse P_Σ from its value $P_{\Sigma 0}$ when $H = 10$ kilogauss is plotted on the axis of the ordinates.

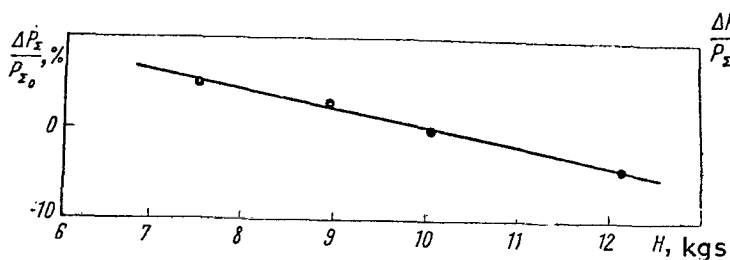


Figure 4

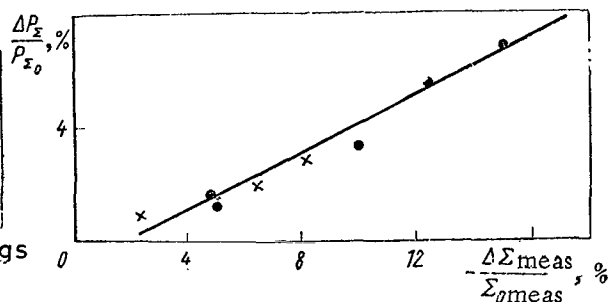


Figure 6

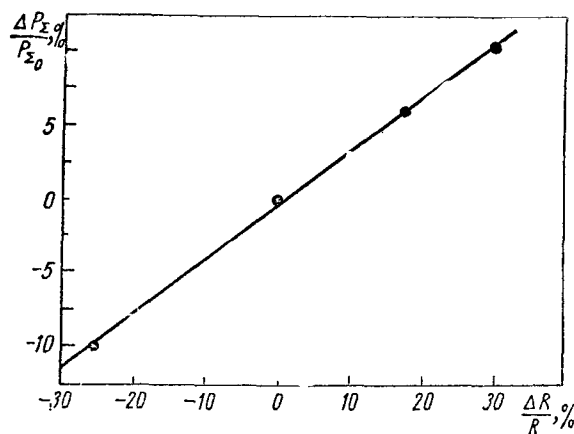


Figure 5

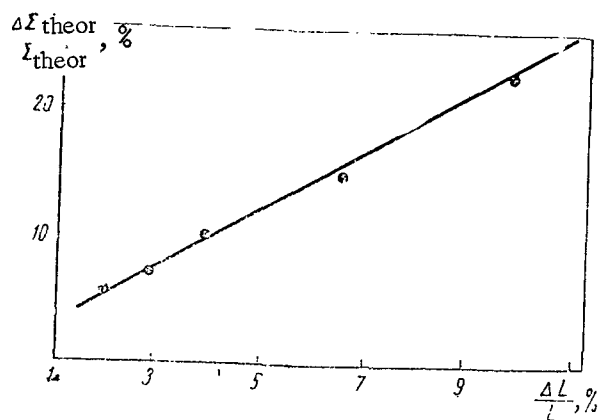


Figure 7

It is obvious from the figure that the dependence of relative error in pulse $\Delta P_\Sigma/P_{\Sigma 0}$ on the value of field H is practically linear. In the range of magnetic field intensity studied $\Delta P_\Sigma/P_{\Sigma 0}$ comprises approximately 2.5% at a 10% deviation of magnetic field intensity from the nominal value.

Figure 5 shows the dependence of mean relative error in a pulse generated when curve $p(s)$ being used differs from the real curve. The calculated curve

and the pulse corresponding to it were taken as the nominal curve and pulse P_{Σ_0} . Variation of the path-pulse curve was included in the displacement of

/82

the nominal curve relative to its initial position. The relative change of the path $\Delta R/R$ at a given pulse plotted on the axis of the abscissas was employed as the extent of displacement. The dependence in this case is also practically linear. The value of $\Delta P_{\Sigma}/P_{\Sigma_0}$ comprises $\sim 2.5\%$ when $\Delta R/R \sim 10\%$.

Errors on determining the parameters of Σ_{meas} , Δs , θ occur because of inaccuracies in measuring the coordinates and because of multiple scattering which distorts the trajectory of the particle. The effect of variations in Σ_{meas} on the value of P_{Σ} is illustrated by Figure 6. Relative variation of pulse $\Delta P_{\Sigma}/P_{\Sigma_0}$, which occurs when there is variation of the area of Σ_0 near its nominal value, is plotted on the axis of the ordinants in Figure 6. It is obvious from the figure that variation of the area by 3% leads to an error of $\sim 1\%$.

Errors in determining Δs and θ cause a variation of values of the area of Σ_{theor} being considered. The error introduced into Σ_{theor} by not knowing angle θ may be easily found directly from expression (3), which yields the following dependence for this error:

$$\frac{\Delta \Sigma}{\Sigma} = 2 \cot \theta \Delta \theta.$$

In order to determine the effect of variations of length on the determination of Σ_{theor} , we made calculations in which the value of Δs was varied similar to that for Σ_{meas} (Figure 6). The result is given in Figure 7.

The effect of errors occurring when measuring the coordinates was studied separately by repeated multiple measurements of selected events. Distribution of relative deviations of individual measurements P_i from the mean value of \bar{P} are shown in Figure 8.

Summarizing all the reasons studied above for the occurrence of errors, we can estimate the mean error characteristic for the tracks of π^+ -mesons studied

($\Delta s \sim 10$ cm; $\frac{\Delta H}{H} \sim 10\%$; $\frac{\Delta R}{R} \sim 5\%$; $\sin \theta \approx 0.95$). On the basis of this we should expect a value of $\Delta P_{\Sigma}/P_R \sim 5\%$. The half-width of distribution in Figure 2 should also be $\sim 5\%$ in accordance with this value of $\Delta P_{\Sigma}/P_R$.

/83

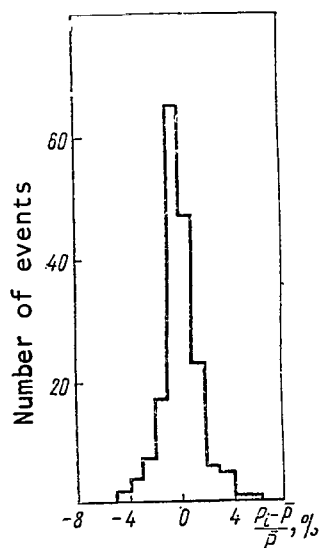


Figure 8.

Actually, the trajectory distortion as a result of multiple scattering was not considered in the preceding study. If all the spread observed is explained by this effect, then it is easy to determine that the fraction of additional error will be $\sim 13\%$.

REFERENCES

1. Sternheimer, R. M., *Phys. Rev.*, Vol. 115, p. 137, 1959.
2. Kruchinin, S. P. et al, *Yaderniya Fizika*, Vol. 1, p. 317, 1965.

A METHOD OF REGISTERING THE ENERGY OF CHARGED PARTICLES WITH A PROPORTIONAL LIGHT COUNTER

V. G. Varlamov, B. A. Dolgoshein and A. M. Rogozhin

ABSTRACT. This article describes a proportional light counter used to record the energy of charged particles. The gas scintillation counter utilizes a Po^{210} α -source and the inside of the counter is filled with an inert gas mixture. The energy of the charged particles is determined by the magnitude of scintillation caused by the ionization losses of these particles.

When charged particles pass through a space filled with (xenon) or some other inert gas (helium, argon, krypton), scintillation occurs, the brightness of which is proportional to the ionization losses of the charged particles. The different characteristics of this process have been thoroughly studied [1]. After an ionized particle has passed through a gas, a track of positive ions and free electrons remains, the lifetime of which is approximately several milliseconds in pure inert gases. If a post electrical field is created in a given volume of gas after a particle has passed through, the electrons of primary ionization will generate avalanches, the path of which will not bend on the spot where the particles pass through. /84.

Therefore, one should expect some proportionality between the value of primary ionization and the flash of light generated in the avalanche by the effect of the electrical field.

Figure 1 depicts a block-diagram of the device. The housing of the gas scintillation counter is made of a polyfluoroethylene resin tube 100 mm in diameter, having two metal flanges which form a plane condenser. An α -source of Po^{210} ($E_{\alpha} = 5.15$ MeV) is attached to the upper electrode. The lower electrode has a window 100 mm in diameter, covered by a metal grid with a spacing of 5 mm. The distance between the electrodes is 50 mm. The field generated in the space may be considered to be homogeneous at distances from the lower electrode of the order of the grid spacing. Metal discs 200 mm in diameter are mounted on the flanges to improve the homogeneity of the field within the space of the counter. A glass through which the inside of the counter is scanned by a photomultiplier is mounted under the grid. A layer of quarter-phenyl $50 \mu\text{g}/\text{cm}^2$, which serves to shift the scintillation spectrum into the area of sensitivity of the FEU photo cathode, is sprayed in a vacuum onto the

inner surface of the glass and onto the upper electrode. Pulses from the photomultiplier anode are fed through the cathode repeater into the discriminator and directly into the AI-100 multichannel amplitude analyzer, which controls the external pulse. The output pulse of the discriminator triggers the high-voltage generator, the negative pulse of which is fed onto the upper electrode of the gas counter. /85

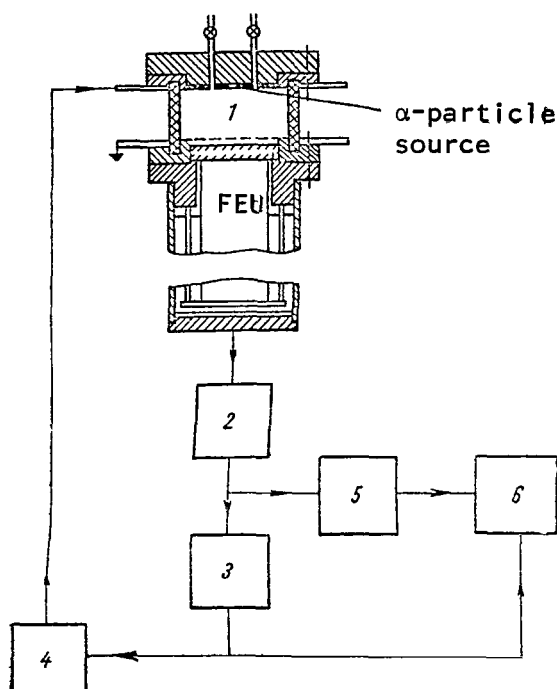


Figure 1. Block Diagram of the Device:
1, Gas counter; 2, Cathode repeater; 3, Discriminator; 4, High-voltage pulse generator; 5, Delay of 0.5 μ sec; 6, AI-100 amplitude analyzer.

The parameters of the negative pulse are: τ front = 10 nsec; exponential decay of τ = 1 μ sec; and amplitude = 2-16 kv. This output pulse is fed from the discriminator with a 0.5 μ sec delay to control the AI-100 so that only pulses generated by the electrical field are analyzed.

Operating measurements were accomplished by filling the counter with a mixture of Xe (at a pressure of 350 mm of Hg) and He^3 (at a pressure of 240 mm of Hg) gases. The counter was exposed to thermal neutrons. Two typical ionizations were observed: I--from α -particles with an energy of $E_\alpha = 5.15$ MeV, and II--from a $n + \text{He}^3 \rightarrow \text{H}^3 + p$ reaction, the products of which have a total ionization of $E_n = 0.76$ MeV.

The primary scintillation pulses trigger the high-voltage generator. The discriminator threshold is selected so that the photomultiplier noise pulses are cut out. /87

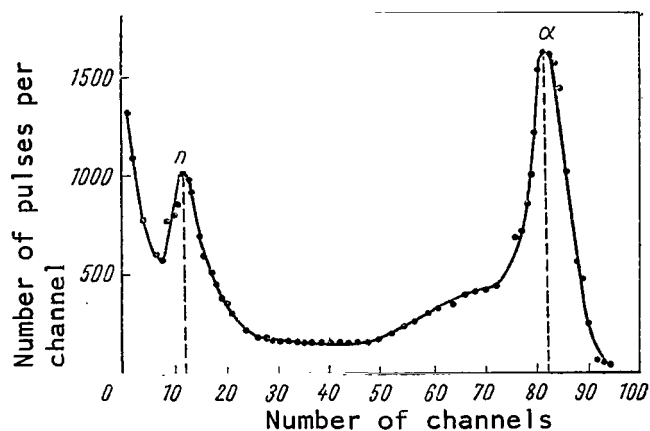


Figure 2. Amplitude Distribution of Secondary Flashes.

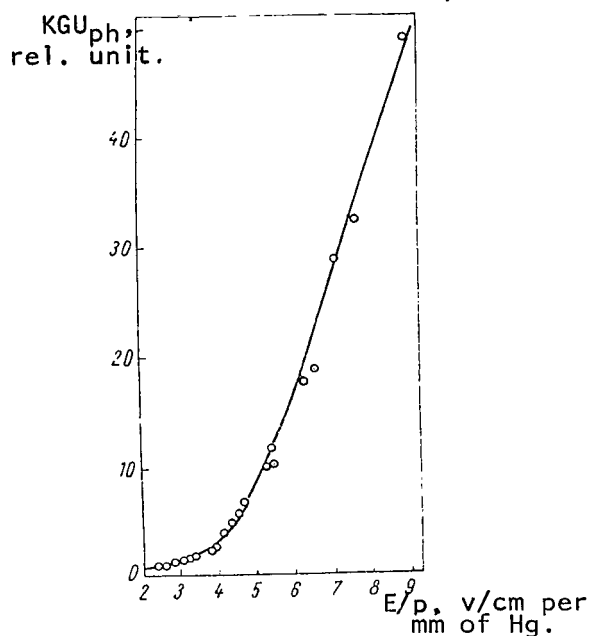


Figure 3. Dependence of Photon Gas Amplification Factor (KGU_{ph}) on the Ratio of Electric Field Intensity to Pressure.

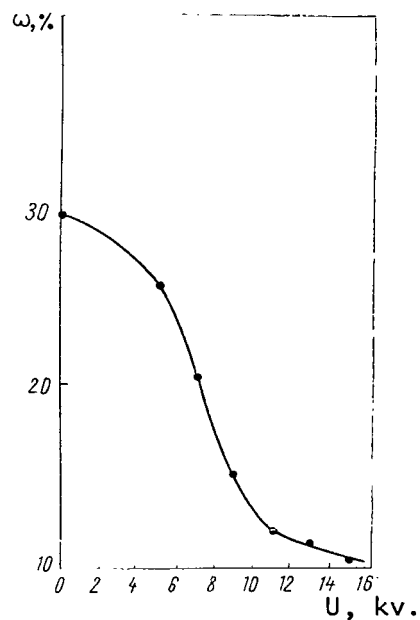


Figure 4. Dependence of Resolution on High-Voltage Pulse Amplitude.

The obtained amplitude spectrum of secondary scintillations generated by the electrical field are given in Figure 2. The amplitude of the high-voltage pulse is 14 kv. Two peaks are visible on the spectrogram, the maximum values of which are in the twelfth and eighty-second channels, respectively, which corresponds to the ratio $E_{\alpha}:E_n = 5.15:0.76 = 6.78:1$ (The ratio $82:12 = 6.8:1$). This indicates the proportionality between the light flash generated in the light avalanche and the ionization inside the gas counter.

The dependence of the value of the secondary flash on the electric field amplitude was studied in the same chamber field only with xenon. The results are presented in Figure 3. The amplitude of the secondary flash exceeds the primary flash by approximately 50 times in pure xenon when $E/p \sim 10$ v/cm·mm of Hg.

The resolution of the given counter ω may be presented in the form

$\omega = \sqrt{\omega_a^2 + \omega_c^2}$, where ω_a is determined by the fluctuation of the number of photons at the same value of ionization losses, and ω_c is determined by the inhomogeneity of light collection by the counter, by the inherent resolution of the photomultiplier, and by the inherent width of the α -source line. Since light output during secondary scintillation is K times greater, resolution of the counter is $\omega = \sqrt{\frac{\omega_a^2}{K} + \omega_c^2}$.

Figure 4 presents the dependence of counter resolution on high-voltage pulse amplitude.

The use of secondary scintillation caused by the electric field makes it possible to improve the energy resolution of the gas counter due to an increase of light output.

REFERENCES

1. Baldin, S. A. et al, *Atomnaya Energiya*, No. 10, 1957.

MODELING PROCESSES WITH GENERATION OF NEUTRAL PARTICLES IN NON-HYDROGEN BUBBLE CHAMBERS

K. N. Mukhin and I. A. Svetlologov

ABSTRACT. This paper is devoted to selection of a method of identifying particles and reactions in a propane bubble chamber. Reaction processes with generation of two charged and several neutral particles, the decays of which generate a typical V-branch in the chamber are modeled by the Monte-Carlo method. The configuration of the chamber, the composition and momentum spread of the initial beam, fermi nucleon motion, and also experimental measurement errors are considered. Moreover, "pseudo-reaction" is analyzed kinematically, i.e., its physical parameters are determined, and are then compared with true values obtained from modeling this reaction, and the possibility of identifying it is thus verified. Calculations were made for a 10-liter propane bubble chamber exposed to a beam of positively charged particles with a pulse of 2.25 GeV/c.

1. Introduction

When processing photographs obtained in hydrogen bubble chambers, if these are good-quality photographs, and the initial moment spread of the beam particles is small, single-value results may be almost always obtained by using kinematic analysis for events occurring in the chamber. However, if the chamber is filled with some kind of heavy liquid, as for example, propane, freon, or xenon, the presence of fermi motion of nucleons in the filled nuclei significantly complicates kinematic analysis. /88

This paper is devoted to selecting a method of identifying particles and their reactions in a propane bubble chamber. The Monte-Carlo method is used to model the reaction processes with generation of two charged and several neutral particles, the decays of which generate a typical V-branch in the chamber. The configuration of the chamber, composition and momentum spread of the initial beam, fermi motion of nucleons, and also experimental measurement errors are taken into consideration. Moreover, "pseudo reaction" is analyzed kinematically, i.e., its physical parameters are determined, which are then compared with true values obtained from modeling this reaction, and thus, the possibility of identifying it is ascertained. Calculations were made for a 10-liter propane bubble chamber, exposed to a beam of positively charged particles with a pulse of 2.25 GeV/c [1].

2. Modeling the Reactions

The beam of primary particles entering the chamber consists of protons, π^+ -mesons and K^+ -mesons. Initial pulse distribution measured experimentally

was approximated by an expression similar to that used to select¹ the initial pulse with an average value of $P_0 = 2.25$ GeV/c, and a distribution half-width of $\Delta P_0 = 0.17$ GeV/c. The selection procedure consists of the following:

1. The initial values of the coordinates of the entering particle (x_0 , y_0 , and z_0) were selected according to the chamber configuration.
2. The type of primary particle is selected on the basis of the quantitative ratio of beam composition. Knowing the effective interaction cross-section of a given particle for a 2.25 GeV/c pulse, its path to interaction L is determined.
3. If the interaction occurred in the chamber, the pulse of the primary particle P_0 is selected on the basis of initial moment distribution.
4. The question of which proton of the target (free or valent to the nucleus) participates in the reaction is determined according to the chemical formula of propane (C_3H_8).
5. The total pulse of particles participating in the reaction P'_0 for a free proton is determined only by the pulse of the initial particle.

Errors obtained from kinematic analysis are caused by measurement errors in the half-width of initial particle distribution. The total pulse varies in absolute value and in direction when it interacts with a proton moving in a nucleus. In order to determine P'_0 in this case, we must assign the value of the fermi-pulse of proton P_p and its direction in the space, i.e., the angle θ_p between the direction of the initial particle pulse and that of the fermi-pulse and an angle χ'_0 between plane (x, y) and plane $(P_0 P_p)$ (Figure 1). The value of P_p is selected on the basis of the nucleon distribution of the pulses for the degenerated fermi-gas [2]. Assuming that the angular distribution of nucleons and the nucleus is isotropic, angles θ_p and χ'_0 are selected and the total pulse of the interacting particles is thus found. The direction cosines of vector P_0 ($\cos \alpha$, $\cos \beta$, and $\cos \gamma$) may be obtained by using the expressions for them from [3].

6. The type of reaction is selected according to the characteristics of two charged particles and the V-branch from decay of a neutral particle. A whole series of three-body reactions, in which Λ , Σ^0 and π^0 will be the neutral particles, may be yielded by π^+ -mesons. A recharging reaction of $K^+p \rightarrow K^0\pi^+p$ and a non-elastic scattering reaction of $K^+p \rightarrow K^+p\pi^0$ are possible for K^+ -mesons. A single three-body reaction of $pp \rightarrow pp\pi^0$ takes place for protons.

¹ Here and henceforth the word "to select" determines the lottery procedure by the Monte-Carlo method.

In addition to these three-body reactions, multiple body reactions are possible, in which several neutral π^0 -mesons are generated along with the charged particles. These processes may imitate the processes of the type being studied if only a single V-branch is observed for any reason. Therefore, the n-body reaction is analyzed. A definite probability is attributed to each of these reactions and thus one of them is selected.

/90

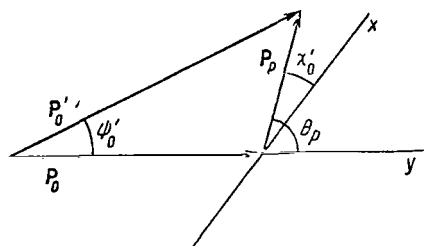


Figure 1.

$$E_{i1} = E_i - E_1; P'_{01} = P'_0 - P_1,$$

where $E_i = E_0 + E_t$, E_0 is the energy of the impinging particle, and E_t is the energy of the target proton. When this operation is repeated n times, an accumulation of the pulses and energies of all particles generated in the reaction is obtained. Thus, a track pattern of the modeled event may be plotted from these data.

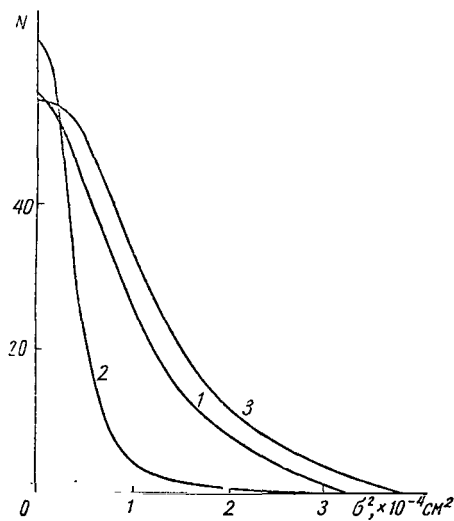


Figure 2.

7. Using the energy distribution of one of the particles of a n-body reaction in the center of mass system, calculated within the limits of statistical theory [4], and also assuming the isotropy of angular distribution, the energy E_1 and the escape angle of this particle are selected. We accomplish the transition to an n-1-body reaction with a new total energy and a pulse of:

8. The introduction of experimental measurement errors into the modeled tracks is based on the use of certain distributions obtained experimentally for tracks actually measured. The number of points N on a track of suitable length was selected in a given case by using the distribution of the number of points for different track length. The lengths of all $(N - 1)$ -intervals of a track were selected by lot from the experimental distribution of interval lengths between points for tracks with small and large paths and the values of coordinates (x, y, z) for all points were calculated. The coordinates were further "smeared" to the values of error $(\pm \Delta x, \pm \Delta y, \pm \Delta z)$ obtained from experimental distributions of error for each coordinate separately. These distributions were plotted according to multiple measurements of the coordinates of a single fixed point of a track.

9. Pseudo-tracks with introduced errors were further processed by the standard method worked out for real events, which leads to the following. A track in plane (x, y) is approximated by a Probala and its direction cosigns

and value σ^2 , characterizing the degree of measurement accuracy and representing the mean square deviation of the track points from the approximated Prohala, are determined. Figure 2 depicts the σ^2 distribution for measurement errors (curve 2) obtained by the method described above. The σ^2 distribution for tracks actually measured (curve 1) is significantly wider. The non-conformity of these distributions may be explained by the inaccuracy of estimating errors of spread for measurements of the coordinates of a fixed track point, because this method does not take into consideration multiple particle scattering. Conformity of calculated and experimental distribution may be achieved by variation of error distributions toward the side of their increase. Curve 3 represents an analogous distribution, but with errors twice as large as in curve 2.

Thus, the method described makes it possible to develop pseudo-events which conform to familiar reactions with known kinematic characteristics, in which true measurement accuracy is correctly considered. Knowing the reaction parameters described by pseudo-events, we can estimate the degree of reliability of the method considered below for solving the reverse problem--identification of reactions by the method of kinematic analysis of events.

3. Method of Identification and Conclusions

The pseudo-events obtained by the method described above are reactions with two charged and one or several neutral particles, of which one is "visible". Our problem is to select from all these reactions such three-body reactions in which a K^0 -meson or Λ -hyperon is the neutral particle reactions. All remaining reactions will be the background. These are reactions with more than three particles--three-body reactions--in which the V-branch is an electron-positron pair of a converted γ -quantum, and also three-body reactions in which the Λ -hyperon has been erroneously identified as a K^0 -meson, and vice versa. It is easy to eliminate the background determined by the γ -quanta, if we examine the aperture angle of the V-branch. In fact, we know that the aperture angle of the electron-positron branch is subject to the condition $\theta \sim mc^2/E$, where E is the γ -quantum energy, and m is the mass of the electron. Thus, the aperture angle distribution in the case of γ -quanta conversion is concentrated within a narrow range of small angles. Figure 3 (curve 3) shows such a distribution obtained experimentally by measuring real electron-positron pairs. Curves 1 and 2 represent similar distributions for Λ -hyperons and K^0 -mesons, respectively, obtained from the pseudo-events developed. It is obvious that if we limit ourselves to a V-branch aperture angle of $\phi > 10^\circ$, almost all the γ -background is eliminated, and the mixture of Λ -hyperons and K^0 -mesons is infinitesimal in the range of $\phi < 10^\circ$. Random selection of γ -quantum conversion was not done for these reasons.

Let us now determine the criterion for separating Λ - and K^0 -particles and selection of three-body reactions from the non-three-body background. Let us assume that the reaction being studied is a three-body reaction, and let us expand the total reaction pulse P'_0 by components to the coordinate axis. The direction cosines of the initial particle and of the three particles--

the products of the reaction--are known; therefore the pulses P_1 , P_2 and P_3 of these particles are determined from the set of three linear equations obtained. The pulse P'_3 of the neutral particle may be obtained independently, using angles ϕ_1 and ϕ_2 , which comprise the decay particles in the flight direction of the neutral particle, and it may be compared with pulse P'_3 , obtained previously from the solution of the set of equations. The formulas for determining P'_3 are given in [5]:

$$M/P'_3 = \frac{(\sin \phi_1 \cdot \sin \phi_2)^{1/2}}{\cos^{1/2}(\phi_1 + \phi_2)},$$

where

$$\cot \phi_1 = \frac{1 - \alpha^* + \epsilon^*}{2} \cot \varphi_1 - \frac{1 + \alpha^* - \epsilon^*}{2} \cot \varphi_2;$$

$$\cot \phi_2 = \frac{1 + \alpha^* + \epsilon^*}{2} \cot \varphi_2 - \frac{1 - \alpha^* - \epsilon^*}{2} \cot \varphi_1;$$

$$\alpha^* = \frac{m_1^2 - m_2^2}{M^2};$$

$$\epsilon^* = \frac{\widetilde{P}_3}{M};$$

m_1 and m_2 are the masses of the particles generated, p is their pulse in the system of rest of the decayed particle, and M is the mass of the decayed particle. Thus, by assigning to M the mass of the K^0 - and Λ -particles, we find two values of P'_3 , respectively, for two types of decay. In order to compare pulses P_3 and P'_3 , the relation

$$\Delta = \frac{1/P_3 - 1/P'_3}{1/P_3}$$

is constructed and the two distributions of these values are constructed from the total statistics of the pseudo-reactions obtained.

One of them conforms to the decay pattern of K^0 -mesons, and the other--to the decay pattern of Λ -hyperons (Figure 4, a and b, histograms I). The histograms of II in Figure 4, a and b refer to so-called true events, i.e., real three-body reactions, in which the neutral particle corresponds to the decay pattern being considered. We shall select the criterion of Δ , analyzing the course of the relationship of the number of background events to the number of true events N_b/N_{tr} for several initial ranges of Δ . These graphs are presented in Figure 5, a and b by curves I for K^0 - and Λ -particles, respectively. The

/93

/94

number of background events decreases significantly, if we discard those cases in which Δ conforms to both decay patterns. This is obvious from Figure 5, which depicts the ratios of N_b/N_t after rejection of the events where Δ corresponds according to the following criteria: II-- $\Delta K^0 < 0.05$, and $\Delta_\Lambda < 0.15$; III-- $\Delta K^0 < 0.1$, and $\Delta_\Lambda < 0.15$; IV-- $\Delta K^0 < 0.15$, and $\Delta_\Lambda < 0.15$.

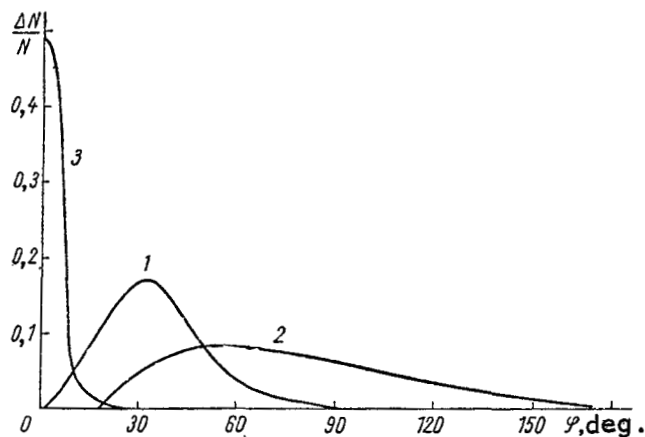


Figure 3.

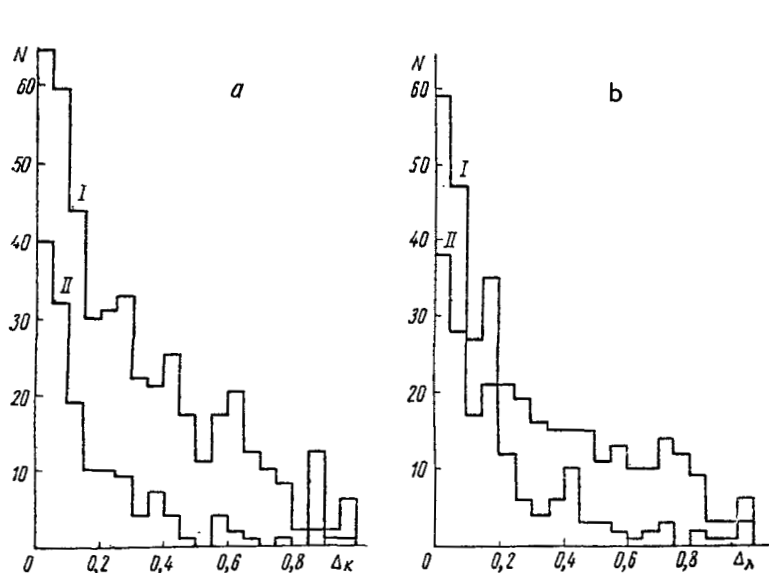


Figure 4.

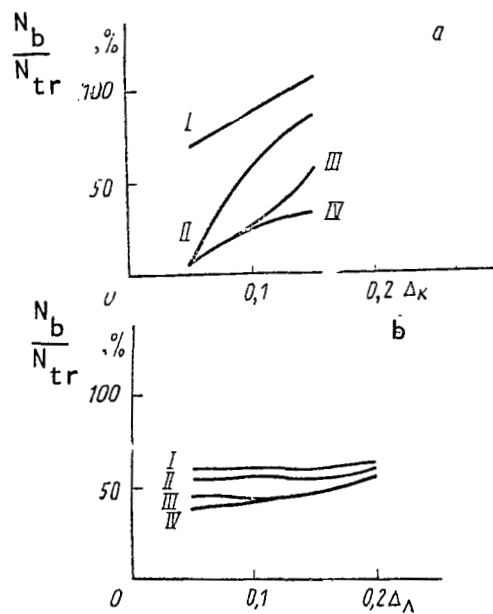


Figure 5.

It is not necessary to assign a large value to the absolute value of the background, because it is very complicated to calculate the entire background which may exist in real events. We are interested in understanding the path of background curves in reactions with K^0 - and Λ -particles, and also in determining how the relationship of the background to the effect changes when experimental opportunities are improved. Figures 6, a and b present the

distributions of Δ for background reactions for the decay patterns of K^0 and Λ , respectively. The curves of I represent non-selection of events according to Δ criterion, and II--selection according to the criterion $\Delta_K^0 < 0.15$, and $\Delta_\Lambda < 0.15$.

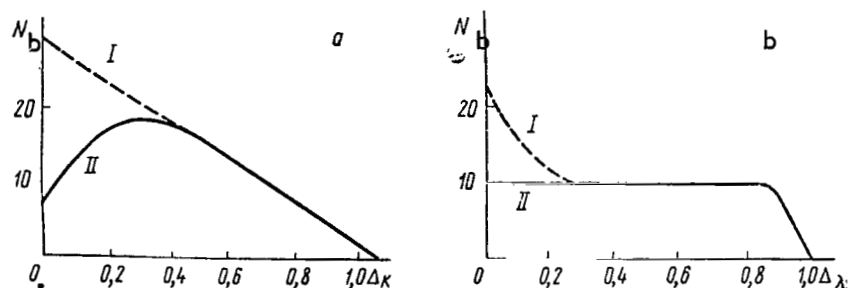


Figure 6.

Thus, if the criteria of II are selected as those of Δ , we can separate $\sim 25\%$ K^0 -mesons and $\sim 85\%$ Λ -hyperons from the available experimental material. The relationship of background to effect in this case comprises 22% for K^0 -mesons and 52% for Λ -hyperons.

Decreasing the spread of initial pulses, and also improving the quality of photographs, and hence measurement accuracy, results in improvement of identification. This is obvious from the table where N_K^0 and N_Λ are the percentages of K^0 - and Λ -particles selected from the total statistics. D_K^0 and D_Λ is the authenticity of K^0 and Λ selected, and percentages.

Table

Criterion	N_{K^0}	D_{K^0}	N_Λ	D_Λ
1	25	78	85	48
2	42	83	70	65
3	50	81	75	68
4	30	92	72	70

The following criteria are considered in the table presented:

1. The half-width of initial momentum spread $\Delta P_0 = 0.17$ GeV/c, $\Delta_K^0 < 0.05$, and $\Delta_\Lambda < 0.15$.

2. $\Delta P_0 = 0.05$ GeV/c, $\Delta_K^0 < 0.05$, and $\Delta_\Lambda < 0.15$.

3. $\Delta P_0 = 0.05$ GeV/c, $\Delta_K^0 < 0.10$, and $\Delta_\Lambda < 0.15$; but the measurement errors are two times less than in cases 1 and 2.

4. The proposals are the same as in case 3, only $\Delta_K^0 < 0.025$, and $\Delta_\Lambda < 0.15$.

Thus, kinematic analysis of events obtained from photographs in chambers with a heavy-liquid filler makes it possible to identify neutral particles even when there is no magnetic field. When there is a magnetic field, additional independent information appears, consideration of which makes it possible to increase identification reliability jointly with the analysis conducted.

In conclusion the authors express their thanks to R. S. Shlypnikov and S. P. Kruchinin for discussion of the results, and also S. A. Chuyeva, A. S. Ormantseva and M. M. Sulkovskaya for their help in preparing the paper.

REFERENCES

1. Mukhin, K. N. et al, *Proc. of Intern. Conf. on High Energy Accelerators and Instrumentation*, p. 514, CERN, 1959.
2. Barkov, L. M. and B. A. Nikol'skiy, *Uspekhi Fiz. Nauk*, Vol. 61, No. 3, 1957.
3. Buslenko, N. P. et al, *Metod Statisticheskikh Ispytaniy* [A Method of Statistical Tests], *Fitmatgiz Press*, Moscow, 1962.
4. Maksimenko, B. M. and I. L. Rozenhal', *Zh. Eksperim. i Teor. Fiz.*, Vol. 32, No. 4, 1957.
5. Podolanski, J. and R. Armenteros, *Philos. Mag.*, Vol. 45, No. 13, 1958.

GENERATION OF HIGH-ENERGY MUONS DURING INTERACTION OF COSMIC RAY NUCLEI WITH NUCLEI OF AIR

Yu. D. Kotov

ABSTRACT. This paper investigates the pattern of muon generation during the decay of pions which occurs as a result of the interaction of cosmic ray nuclei with those of air. The paper considers the interaction of high-energy protons with nuclei of air during which pions are generated due to the decay of an isobar occurring during the interaction.

This paper investigates a muon generation pattern during decay of pions occurring as a result of the interaction of cosmic ray nuclei with nuclei of air.

/97

Pions are generated during interaction of high-energy protons with nuclei of air principally by two processes [1, 2]--first, a pion which carries away a significant fraction ($\sim 25\%$) of the energy of the primary nucleon is produced from the decay of an isobar occurring during the interaction; secondly, during multiple pion production (in particularly, decay of fire-balls). The spectrum is determined mainly by the pions occurring during isobar decay because of the decreasing energy spectrum.

The mechanism of pion generation as a result of the interaction of a high-energy nucleus (≥ 100 GeV) with a nucleus of air has been barely studied up to the present; however, there are indications [3] that the interaction of heavy nuclei with photoemulsion nuclei may be considered as the sum of independent nucleon-nucleon interactions. We shall further assume that the interaction of an impinging nucleus with a nucleus of air generates $0.8 A$ isobars, where A is the atomic weight of the impinging nucleus, and the pion of isobar decay carries away 25% of the energy arriving at the nucleon of the impinging nucleus. We shall consider that charged pions comprise $2/3$ of all pions.

Let us find the number of n_π pions having an energy from E_π to $E + dE_\pi$ generated as a result of isobar decay of the first process of nuclei interaction. According to [4], let us assume that the energy spectra of different charged groups are similar and let us write them in the form

$$I_A(\varepsilon) d\varepsilon = P_A \varepsilon^{-(\gamma+1)} d\varepsilon$$

where $I_A(\epsilon)d\epsilon$ is the number of nuclei with an atomic weight A and an energy arriving at a single nucleon in the range from ϵ to $\epsilon + d\epsilon$. Then

$$n_\pi(E_\pi) = \beta \alpha^\gamma m E_\pi^{-(\gamma+1)} dE_\pi \sum_A P_A, \quad (1)$$

where α is the amount of energy carried away by the fast pion; m is the probability of the generation of an isobar carried to a single nucleon of the impinging nucleus; and β is the fraction of charged pions among all those generated as a result of isobar decay.

/98

When charged pions pass through the atmosphere, they may decay or interact with nuclei of air. Let us write the probability $W(E_\mu, k)$ of muon generation having an energy of E_μ due to pion decay on the assumption that the path of pion interaction is equal to the path of nucleon interaction:

$$W(E_\mu, k) = \int_0^{x_0} k u_\pi e^{-(k-1)y} y^{u_\pi} dy \int_y^{x_0} e^{-z} z^{-(u_\pi+1)} dz, \quad (2)$$

where $u_\pi = \lambda M_\pi / E_\pi \tau_\pi c$ (E_π is the energy of the decaying pion; M_π is the mass of the pion; $\lambda = 8000$ m; τ_π is the lifetime of the pion; k is the ratio of the path of nucleon interaction to that of the interaction of a nucleus in air; and x_0 is the depth of observation in the atmosphere measured in units of the path of nucleon interaction. At sea level $x_0 \gg 1$ and therefore (2) may be written in the form

$$\begin{aligned} W(E_\mu, k) &= k u_\pi \int_0^\infty y^{u_\pi} e^{-(k-1)y} dy \int_y^\infty e^{-z} z^{-(u_\pi+1)} dz = \\ &= k u_\pi \int_0^\infty y^{u_\pi} e^{-y(k-1)} \Gamma(-u_\pi, y) dy = \\ &= \frac{u_\pi}{u_\pi+1} {}_2F_1\left(1, 1, u_\pi+2, \frac{k-1}{k}\right), \end{aligned} \quad (3)$$

where $\Gamma(-u_\pi, y)$ is an incomplete Γ -function; and ${}_2F_1(1, 1, u_\pi+2, k-1/k)$ is a hypergeometric function.

Using (1) and (3) and assuming that $E_\pi = 1.3 \bar{E}_\mu$, we obtain the differential energy spectrum of muons generated by the interaction of cosmic ray nuclei with nuclei of air:

$$N(E_\mu) dE_\mu = \frac{(\alpha/1, 3)^\gamma \beta m E_\mu^{-(\gamma+1)} dE_\mu}{1 + E_\mu/84} \sum_A A P_A {}_2F_1\left(1, 1, \frac{84}{E_\mu} + 2, \frac{k-1}{k}\right).$$

The relationship between P_A for different charged groups is taken from [4] with $\gamma = 1.7$ and the value of P_A is taken from [5], the results of which are presented in Figure 1. The values of k obtained in this manner are presented in Table 1.

Table 1

Group	\bar{A}	κ	$P_A, \text{cm}^{-2}/\text{sec}^{-1}/\text{sterad}^{-1} \times$ $\times \text{GeV/nucleon}$	$\bar{A}P_A$
α	4	1,67	$1,05 \cdot 10^{-1}$	$4,2 \cdot 10^{-1}$
L	10	2,38	$2,40 \cdot 10^{-3}$	$2,4 \cdot 10^{-2}$
M	14	2,65	$6,40 \cdot 10^{-3}$	$9,0 \cdot 10^{-2}$
H	31	3,82	$2,13 \cdot 10^{-3}$	$6,6 \cdot 10^{-2}$

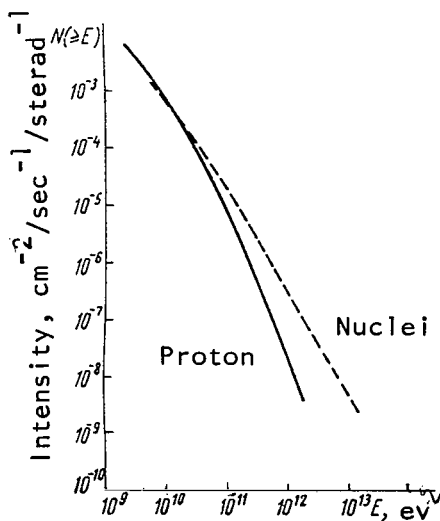


Figure 1. The Integral Spectrum of Primary Protons and Nuclei [5].

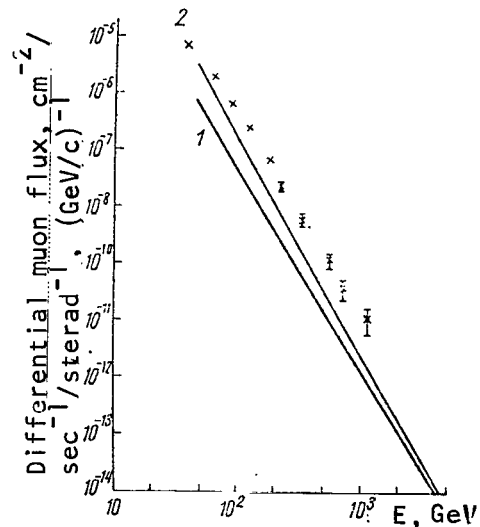


Figure 2. The Differential Spectrum of Muons Created by Primary Nuclei (1), and the Spectrum of Muons Created by Both Nuclei and Protons (2):
x is the spectrum obtained experimentally [6].

Table 1 also shows values of k , during calculation of which for the cross-section of the interaction of the nucleus with air we used the formula

$$\sigma = \pi(R_1 + R_2 - 1,7 \cdot 10^{-13})^2 \text{ cm}^2,$$

where R_1 and R_2 are the radii of colliding nuclei equal to $R = 1,45 \cdot 10^{-13} A^{1/3}$ /99
cm. We assumed γ in the calculations to be equal to 1.7 for all groups of nuclei over the entire energy range. We obtained an analytical expression ${}_2F_1$ as functions of k for different values of E_μ . These expressions are given in Table 2. The calculated differential spectrum of muons generated by interaction of cosmic ray nuclei are also given in Figure 2. This figure also depicts the spectrum of muons generated by the interaction of primary protons with nuclei of air. The spectrum of protons was taken from [5] for the calculations, and the values of the interaction constant are the same as for the nuclei.

Table 2

$u_{\pi \rightarrow 0}$	${}_2F_1\left(1, 1, 2, \frac{k-1}{k}\right) \rightarrow \frac{k}{k-1} \ln k$
$u_{\pi = \frac{1}{2}}$	${}_2F_1\left(1, 1, \frac{5}{2}, \frac{k-1}{k}\right) = \frac{3k}{k-1} \times$ $\times \left[1 - \frac{1}{\sqrt{k-1}} \arctan \sqrt{k-1}\right]$
$u_{\pi = 1}$	${}_2F_1\left(1, 1, 3, \frac{k-1}{k}\right) = \frac{2k}{k-1} \left[1 - \frac{\ln k}{k-1}\right]$
$u_{\pi = 2}$	${}_2F_1\left(1, 1, 4, \frac{k-1}{k}\right) = \frac{3k}{(k-1)^3} \times$ $\times \left[\frac{(k-1)^2}{2} - (k-1) + \ln k\right]$

Comparing the calculated spectrum with that obtained experimentally, we /100
should point out that only the first process of interaction was considered. When further processes are investigated, we must consider both the coefficient of inelasticity during nucleus-nucleus interaction and the probabilities of fragmentation. Analysis indicate that calculation of subsequent processes leads to an increase of calculated intensity by approximately 30%.

Analysis of the data obtained indicates that high-energy muons (> 100 GeV) are generated mainly due to decay of pions produced during interactions of primary cosmic ray nuclei with nuclei of air. However, a discrepancy between the anticipated muon spectrum and that observed experimentally [6] occurs in the case of the interaction constants selected and the energy spectrum of primary radiation used.

In conclusion, the author expresses sincere thanks to N. L. Grigorov for constant interest and valuable discussions.

REFERENCES

1. Dobrotin, N. A. et al, *XII Mezhdunarodnaya Konferentsiya Po Fizika Vysokikh Energiy. Dubna 1964* [XII International Conference on High-Energy Physics. Dubna 1964], Vol. 1, p. 335, Atomizdat Press, Moscow, 1966.
2. Peak, L. S. and R. L. S. Woolcott, *Nuovo cimento*, Vol. XLII, No. 4, p. 856, 1966.
3. Abraham, F. et al, *XII Mezhdunarodnaya Konferentsiya Po Fizika Vysokikh Energiy. Dubna 1964* [XII International Conference on High-Energy Physics. Dubna 1964], Vol. 1, p. 163, Atomizdat, Moscow, 1966.
4. Ginzburg, V. L. and S. I. Syrovatskiy, *Proiskhozhdeniye Kosmicheskikh Luchey* [The Origin of Cosmic Rays], p. 44, AN USSR Academy of Sciences, Moscow, 1963.
5. Grigorov, N. L. et al, *Izv. AN SSSR. Ser. Fiz.*, No. 31, 1967.
6. Brooke, G. et al, *J. Phys. Soc. Japan*, Vol. 17, Supplem., A111, p. 311, 1962.

COSMIC γ -RADIATION

A. M. Gal'per and B. I. Luchkov

ABSTRACT. This paper is concerned with the measurement of cosmic X-ray and γ -ray photon fluxes originating in our own galaxy and in the metagalaxy. The paper describes experiments carried out on balloons and satellites and also the equipment used to conduct the experiments. A survey is presented which summarizes the results of recent experiments and discusses the methodology and techniques of the experiments.

1. Introduction

Two new trends--X-ray and γ -astronomy are developing rapidly at present along with optical and radio astronomy. The first reports have been received on X-ray and γ -photon fluxes in the universe. Local sources of X-rays have been discovered and a number of experiments have been conducted in the search for discrete sources of γ -photons. These experiments were possible as a result of the rapid development in recent years of the technique of raising scientific equipment (balloons, rockets, satellites) to high altitudes, because it has not been possible to conduct similar experiments near the surface of the earth because of absorption of strong electromagnetic radiation by the earth's atmosphere.

/101

Measurement of cosmic X-ray and γ -photon fluxes will contribute to solution of many important problems of modern astrophysics, i.e., for example, the origin and propagation of cosmic rays in our galaxy and in the Metagalaxy, the presence or absence of anti-matter in the universe, the density distribution of matter in the galaxy, the origin of cosmic radio, X-ray, and γ -radiation and many others. It is not excluded that observation of X-ray and γ -radiation of the universe may lead to discovery of completely new aspects of the earth, and to new opinions of the universe.

Special theoretical papers and surveys [1-11] are devoted to problems of X-ray and γ -astronomy. Part of them contain a survey of experimental results obtained in X-ray astronomy [6, 9, 11], and others discuss the first results

of measuring cosmic γ -photon fluxes [6, 7, 8]. Many experimental papers, in which interesting results have been obtained, have since been completed on measurement of cosmic γ -photons. The experimental technique has been improved substantially. This survey summarizes the results of recent experiments and discusses the methodology and techniques of the experiments. The survey is concerned with measurement of cosmic γ -photon fluxes with an energy of $E_\gamma \approx 50$ -1000 MeV. Reports of low-energy cosmic γ -photons (0.1-10 MeV) are contained in [6], and the results of measuring ultrahigh-energy γ -photons (10^{11} - 10^{12} eV) can be found in [12-14].

/102

2. Fundamental Processes of Cosmic γ -Photon Generation

γ -Photons in cosmic space are generated as a result of the interaction of charged particles of cosmic rays with interstellar matter and photons. The fundamental processes which cause generation of γ -photons are: production and decay of π^0 -mesons in nuclear collisions, braking radiation of relativistic electrons, scattering of light photons in relativistic electrons, the reverse Compton effect and radiation of electrons in a magnetic field ("synchrotron radiation") "Pion", braking, Compton and "synchrotron" γ -photons are distinguished by the process of generation.

a) Pion γ -Photons

Pion γ -photons are generated during decay of neutral π -mesons ($\pi^0 \rightarrow 2\gamma$), which are produced during n-elastic collisions of the protons and nuclei, comprising cosmic rays, with interstellar gas. The pion γ -photon flux and also the cross-section of π^0 -meson generation (according to the data of research on accelerators) may be calculated, if the composition, intensity and energy spectrum of the proton-nuclear component of cosmic rays is known. The energy of γ -photons generated during decay of π^0 -meson is equal to ~ 70 MeV in the

π^0 -meson rest system and $\frac{70\sqrt{1-\beta}}{1+\beta} \leq E_\gamma \leq \frac{70\sqrt{1+\beta}}{1-\beta}$ in the laboratory system,

where β is the velocity of the π^0 -meson.

b) Braking γ -Photons

The relativistic electrons of cosmic rays passing through the interstellar medium create braking electromagnetic radiation with a discontinuous spectrum, the greater energy (shortwave) part of which is γ -photons. The presence of electrons in cosmic rays was confirmed by a number of experimental papers of recent years (see, for example, [17, 18]), in which the electron component of primary cosmic radiation near the earth was measured. High-energy electron fluxes also exist in many cosmic objects of galactic and metagalactic nature (the Crab Nebula in the constellation Taurus, the radio galaxy Cygnus-A, Cassiopeia-A and others), which has been discovered by the powerful radio-emission of these objects [15, 16, 17].

/103

c) Compton γ -Photons

γ -Photons also occur in cosmic space during scattering of light photons in relativistic electrons. In this process, called the reverse Compton-effect, the electron transmits part of its energy to the photon. The intensity of the Compton γ -photon flux depends on the flux of relativistic electrons and on the density of radiant energy, which in cosmic space consists of light and heat photons emitted by stars, and of photons of the isotropic thermal radiation of the universe (Relic radiation [19]).

d) Synchrotron γ -Photons

Synchrotron (magnetic braking) radiation is emitted by high-energy electrons when they move in a magnetic field. Synchrotron radiation occurs in cosmic objects, in which there are large relativistic electron fluxes and magnetic fields exceeding the value of the mean galactic magnetic field (10^{-5} - 10^{-6} oersteds). The greater part of non-thermal radioemission [15] and radiation of the brighter radio sources in our sky is explained by the synchrotron mechanism. The short-wave "tail" of synchrotron radiation, having a discontinuous energy spectrum like ordinary braking radiation, falls within the energy range of γ -photons.

3. Galactic and Metagalactic γ -Radiation

The γ -photons observed near the earth may be of galactic or metagalactic origin. Their intensity is determined by the intensity of cosmic rays and by the density of the matter in our galaxy and in the entire universe (the metagalaxy).

The flux of γ -photons arriving at the earth in a certain direction depends on the amount of matter distributed along the path of the flux. Because matter in the galaxy is distributed anisotropically relative to the earth, there should exist anisotropy of the flux of galactic γ -photons--the maximum flux is observed in a direction toward the center of the galaxy; a flux will be much smaller in value if it arrives from a direction opposite the center of the galaxy (the anti-center); the minimum flux of γ -photons will arrive along the path of the galactic poles (Figure 1). Table 1 presents calculated values taken from [6] of γ -photon fluxes with energies of $E_{\gamma} \geq 50$ MeV and $E_{\gamma} \geq 1000$ MeV, which arrive at the earth from three separate directions in the galaxy (from the center, from the anti-center and from the pole). Values of γ -photons generated during different processes (pion, braking and Compton γ -photons) and also total fluxes are given separately. It was assumed when calculating the fluxes given in Table 1 that the intensity of cosmic rays is uniform everywhere in the galaxy and is equal to the intensity in the environs of the earth. As follows from Table 1, the anisotropy of the galactic flux is quite high and varies with the energy of γ -photons. The ratios of total fluxes arriving from the center, from the anti-center and from the pole of the galaxy are equal-- $I_c : I_{ac} : I_{pole} = 24:5:1$; for $E_{\gamma} \geq 50$ MeV; and $I_c : I_{ac} : I_{pole} = 9:2:1$ for $E_{\gamma} \geq 1000$ MeV.

/104

/105

The anticipated γ -photon fluxes produced beyond our galaxy are given in the last column of Table 1. Calculation of these fluxes is more difficult than that of galactic fluxes because of the uncertainty with which the density of matter and the intensity of cosmic radiation in the metagalaxy are presently known. Therefore, unknown parameters characterizing the ratio of cosmic radiation intensity (ξ_{cr}) and electrons (ξ_e) in the metagalaxy and galaxy are introduced into the expression for the flux. It is obvious that the flux of metagalactic γ -photons is isotropic.

The total flux of cosmic γ -photons produced within the galaxy will be measured during the experimental study. The galactic and metagalactic fluxes may be determined separately and the parameters of ξ_{cr} and ξ_e , particularly, may be calculated by separating its isotropic and anisotropic parts. The study of cosmic γ -photons may nevertheless yield information about cosmic rays and electrons in the metagalaxy, and also much valuable information for astrophysics about the density of the matter and the intensity of cosmic radiation in different parts of the galaxy.

/106

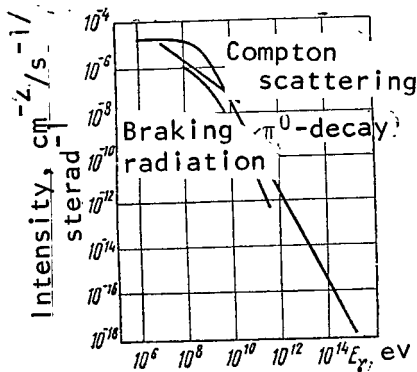


Figure 2. The Integral Energy Spectrum of Galactic γ -Photons.

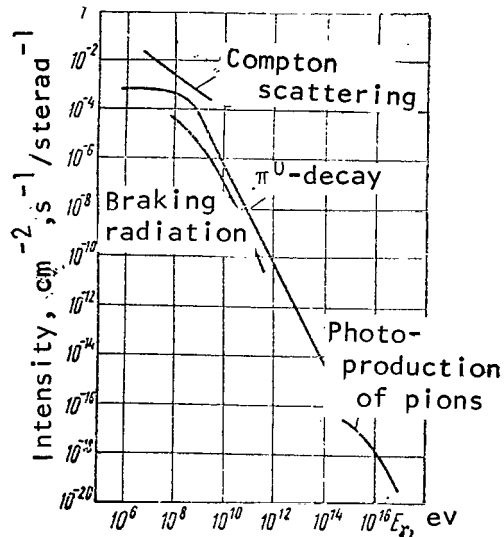


Figure 3. Integral Energy Spectrum of Metagalactic γ -Photons.

Figures 2 and 3 present the energy spectra of galactic and metagalactic γ -photons generated during decay of π^0 -mesons, during the processes of braking radiation and Compton scattering of relativistic electrons [8]. (The fluxes of metagalactic γ -photons were calculated on the assumption that $\xi_{cr} = 1$ and $\xi_e = 1$, and the density of intergalactic gas is equal to 10^{-5} g/cm^3 .) It is obvious from the energy spectra given that the contributions of individual processes of γ -radiation generation to the total flux differ at different energies. Consequently, by making a study of cosmic γ -photons at different energies, we may in principle separate it into fluxes of pion, braking and Compton γ -photons, which permits us to rather refine our knowledge of cosmic rays in the galaxy and the metagalaxy.

4. Discrete Sources of Cosmic γ -Rays

Fluxes of individual cosmic objects, similar to fluxes of local sources of radioemission [15, 16] and X-radiation [6, 9, 11] should exist in addition to the common fluxes of galactic and metagalactic γ -radiation. The cosmic objects which are brighter at the radio wave length are being studied as possible discrete sources of γ -photons--the Crab Nebula, which is in our galaxy and which is the envelope of a Super Nova, the flare-up of which was recorded in 1054; the normal galaxy M31 which is located in the constellation Andromeda; and the radio galaxies M87 (Virgo-A) and Signeus-A. Table 2 [6] shows the anticipated fluxes of γ -photons with an energy of $E_\gamma \geq 1000$ MeV, emitted by these discrete sources and calculated on the assumption that their radioemission has a synchrotron character. The values of γ -photon fluxes with an energy of $E_\gamma \geq 50$ MeV from the same sources is approximately one order greater.

Table 2
Integral Flux of γ -Photons from Discrete Sources
 $F_\gamma(E_\gamma > 1000 \text{ MeV})$ in $\text{cm}^{-2}/\text{sec}^{-1}$

Source	Process			Total Flux
	$\pi^0 \rightarrow 2\gamma$	Braking radiation	Compton effect	
Crab Nebula (Taurus-A)	$2 \cdot 10^{-10}$	$5 \cdot 10^{-11}$	$2 \cdot 10^{-10}$	$4.5 \cdot 10^{-10}$
Galaxy M31 (Constellation Andromeda)	$8 \cdot 10^{-11}$	$2 \cdot 10^{-11}$	$1 \cdot 10^{-8}$	$1 \cdot 10^{-8}$
Radio galaxy M87 (Virgo-A)	$1 \cdot 10^{-11}$	$3 \cdot 10^{-12}$	$1 \cdot 10^{-9}$	$1 \cdot 10^{-9}$
Radio galaxy Signeus-A	$2 \cdot 10^{-12}$	$5 \cdot 10^{-13}$	$1 \cdot 10^{-9}$	$1 \cdot 10^{-9}$

We could continue the list of possible discrete sources, including in it other intensive sources of radioemissions--the radio galaxies Centaur-A, Fornus-A, Perseus-A, Hercules-A and others, quasistellar radio sources (quasars) 3C-273B, 3C-48, 3C-147 and others [20] and recently discovered local sources of X-rays in the constellations of Scorpion, Signeus, Virgo and others [9, 11]. In particular, if the radioemission of quasars is synchrotronic, we may expect from them (i.e., from 3C-273B) rather large fluxes of γ -photon-- $F_q(E_\gamma \geq \text{MeV}) = \frac{107}{10^{-4}-10^{-6} \text{ cm}^{-2}/\text{sec}^{-1}}$.

It should be noted that the intensities of expected γ -photon fluxes given in Tables 1 and 2 are not accurate because of many ambiguities and assumptions made while calculating them. Calculations of similar fluxes by other authors [4, 5, 7, 8, 16, 17] lead to somewhat different results. There are especially

large discrepancies, sometimes by several orders, in calculations of γ -photon fluxes from discrete sources. Further refinement of the values of expected fluxes will be accomplished as new experimental data on cosmic radio, X- and γ -radiation are obtained.

5. Attenuation of Cosmic γ -Photon Flux

The basic process of absorption for γ -photons with an energy of $E_\gamma \approx 50$ -1000 MeV is the process of pair formation and to a lesser extent Compton scattering in atomic electrons. Attenuation of the γ -flux along a path h is calculated by the formula

$$\frac{I}{I_0} = e^{-\mu h}, \quad (1)$$

where I_0 and I are the intensities of initial and final fluxes, and μ is the coefficient of absorption.

Cosmic γ -photons pass through the interstellar medium, which is a very rarified gas (basically hydrogen), and the earth's atmosphere. Attenuation of the γ -photon flux at these two junctures of the path are very different.

a) Transit of γ -Photons Through the Interstellar Medium

Despite the great distances traveled by cosmic photons from their place of origin to the earth, they encounter comparatively little matter. The average amount of matter along their entire path in the galaxy is $\bar{L}_g = 1.6 \cdot 10^{-3}$ g/cm², it is equal to $\bar{L}_{cg} \approx 6 \times 10^{-2}$ g/cm² through the center of the galaxy, and it is equal to $L_M \approx 0.1$ g/cm² on the path through the entire metagalaxy [6]. The exponential index in (1) calculated for these values of L are respectively equal to: $\mu \bar{L}_g \approx 2 \cdot 10^{-5}$; $\mu \bar{L}_{cg} \approx 7.2 \cdot 10^{-4}$; and $\mu L_M \approx 1.2 \cdot 10^{-3}$. The corresponding attenuations of γ -photon fluxes will be $2 \cdot 10^{-3}$, $7.2 \cdot 10^{-2}$ and 0.12%, from which it follows that practically the entire visible universe is transparent for γ -photons. In this regard γ -photons are similar to radioemissions and visible light, but differ from ultraviolet radiation in the range of 10-1000 ev, which is absorbed strongly by interstellar gas (Figure 4 [21]).

b) Transit of γ -Photons through the Earth's Atmosphere

Another situation arises when γ -photons enter the earth's atmosphere. Figure 5 [21] presents a graph of the absorption of electromagnetic radiation reaching the earth from an external source. As can be seen from the graph, the atmosphere is relatively transparent only for certain types of radiation--for radiowaves of metric and centimetric wavelengths, visible light and a number of waves in the infrared region. The atmosphere is completely opaque for hard photons. Even at an altitude of ~ 20 km above sealevel the cosmic γ -photon flux is attenuated by a factor of two.

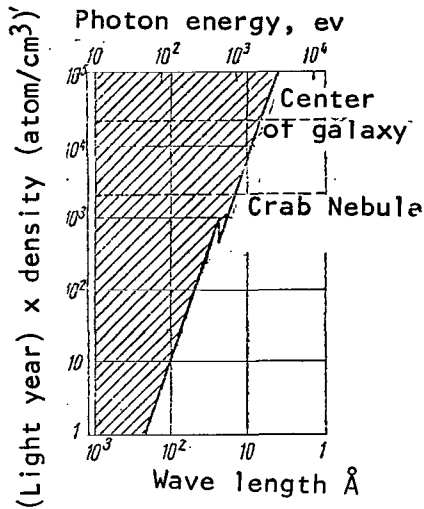


Figure 4. Absorption of Electromagnetic Radiation in Cosmic Space Depending on Photon Energy.

6. Secondary (Atmospheric) Flux of γ -Photons

A secondary flux of γ -photons is generated in the earth's atmosphere by the charged component of cosmic rays, which makes it very difficult to measure the primary cosmic flux. The intensity of the flux of secondary γ -photons according to the data of [24] is equal to $(1.7 \pm 0.1) \cdot 10^{-3} \text{ cm}^{-2}/\text{s}^{-1}/\text{sterad}^{-1} (\text{g}/\text{cm}^2)^{-1}$. This means that the secondary flux and the upper layers of the atmosphere at a depth of several g/cm^2 exceeds by many times the primary flux of cosmic γ -photons. The background of atmospheric γ -photons is one of the main reasons which make it necessary to launch instruments to high altitudes, to the edges of the atmosphere.

/109

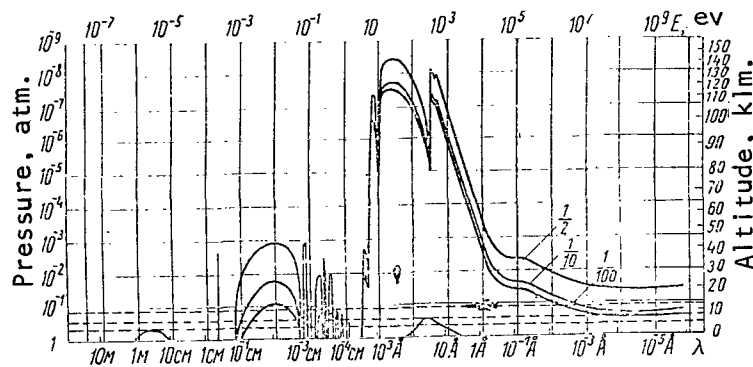


Figure 5. Absorption of Electromagnetic Radiation in the Earth's Atmosphere. The solid lines with the numbers 1/2, 1/10 and 1/100 indicate the levels of decrease of radiation intensity by 2, 10 and 100 times.

Besides the flux of the secondary γ -photons directed downward from above, there is a reverse (albedo) flux of γ -photons of secondary origin which cannot always be correctly calculated in experiments carried out at the edge of the atmosphere and even beyond it. For example, in the first experiments on measurement of cosmic γ -photon intensity [22-24], it was attempted to isolate the primary flux by making measurements at different altitudes and extrapolating the experimental data to the edge of the atmosphere. As indicated by the analysis carried out in [26], such extrapolation was invalid, because it did not

take into consideration albedo γ -photons traveling from the line of the horizon and reaching the apparatus at high angles to its vertical axis. The flux of primary γ -photons of $\sim 2 \cdot 10^{-3} \text{ cm}^{-2}/\text{sec}^{-1}/\text{sterad}^{-1}$ measured in [24] was overestimated for this same reason. Kraushaar and Clark measured the albedo flux during the flight of the artificial satellite Explorer-XI [25, 26]. Figure 6 presents the angular distribution of γ -photons, mainly of secondary origin, recorded during this experiment. The maximum distribution at an angle of $\theta = 63^\circ$ corresponds to the flux of albedo γ -photons from the line of the horizon. Following [26], the albedo flux at any altitude may be presented as the sums of two fluxes--that originating from the disc of the earth $I_{d,e}$ and from the line of the horizon F_{hor} . The change of F_{hor} with the altitude of observation may be represented by the following dependence:

/110

$$F_{\text{hor}} \approx c \frac{1}{r^2 \cos \varphi}, \quad (2)$$

where r is the distance from the point of observation to the center of the earth, and φ is the angle between the direction to the horizon and that normal to the earth. These fluxes at an altitude of $\sim 800 \text{ km}$ are equal to: $I_{d,e} = 3.2 \cdot 10^{-3} \text{ cm}^{-2}/\text{sec}^{-1}/\text{sterad}^{-1}$; and $F_{\text{hor}} = 2.1 \cdot 10^{-2} \text{ cm}^{-2}/\text{sec}^{-1}$.

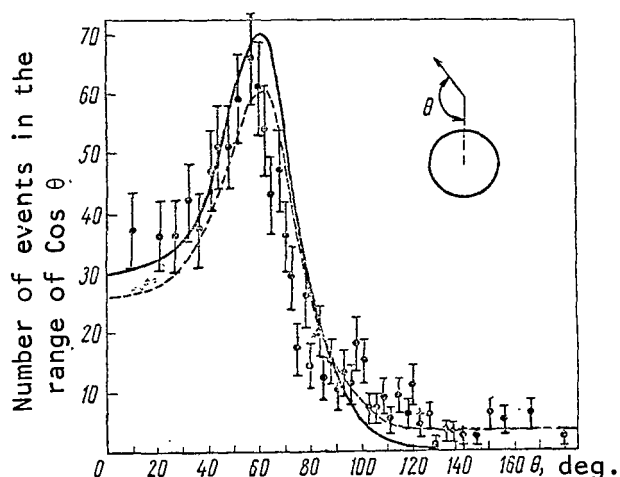


Figure 6. Angular Distribution of γ -Photons Produced in the Earth's Atmosphere [26].

The integral energy spectrum of secondary γ -photons with an energy of $E_\gamma \geq 50 \text{ MeV}$, in particular, was measured in an experiment conducted by N. L. Grigorov et al [27] on artificial satellites "Proton-1" and "Proton-2". The spectrum has a step form with an index of $\alpha = 1.6$. This result agrees with the assumption that secondary γ -photons occur mainly during decay of π^0 -mesons generated in the atmosphere by cosmic rays.

7. Devices for Recording of Cosmic γ -Photons

γ -Photons with energies of 50-1000 MeV are recorded in electron-positron pairs which they produce in a block of matter--the converter-- $\gamma \rightarrow e^+ + e^-$. A device measuring γ -photon flux should consist of a converter, a counter

telescope located beneath the converter, and an anti-coincidence counter located above the converter which altogether separate the generation of charged particles in the converter by neutral radiation. An example of such a device is the Kraushaar-Clark instrument [25, 26], a diagram of which is given in Figure 7. The γ -photon converter is a scintillation "sandwich"-counter

/111

consisting of alternate layers of CsI and NaI crystals, the total thickness of which is equal to a single radiation length. Electron-positron pairs are recorded by the scintillator-sandwich S and Cerenkov counter Č. The solid angle separated by the counter telescope SC is equal to ~ 0.25 steradians. The counter telescope is mounted inside a housing made of a plastic scintillator and which acts as the anti-coincidence counter A. The recorded γ -events are coincidences of the type $S\bar{C}A$. With each such event an amplitude analysis is made of the pulse from the sandwich-counter, which made it possible to isolate γ -photon conversion events from those of nuclear interactions produced by cosmic ray particles, i.e., by neutrons. The efficiency of γ -photon conversion measured during calibration of the instrument in beams of monoenergetic γ -photons in an accelerator were equal to 17% for $E_\gamma \geq 300$ MeV. The geometric factor of the device is equal to 1 ± 0.3 cm²/sterad.

In their experiment [27] N. L. Grigorov et al used a device similar to the Kraushaar-Clark device, the only difference being that a total absorption Cerenkov counter, with which the γ -photon energy was measured, was used in it. This made it possible to determine the energy spectrum of recorded γ -photons simultaneously with the flux.

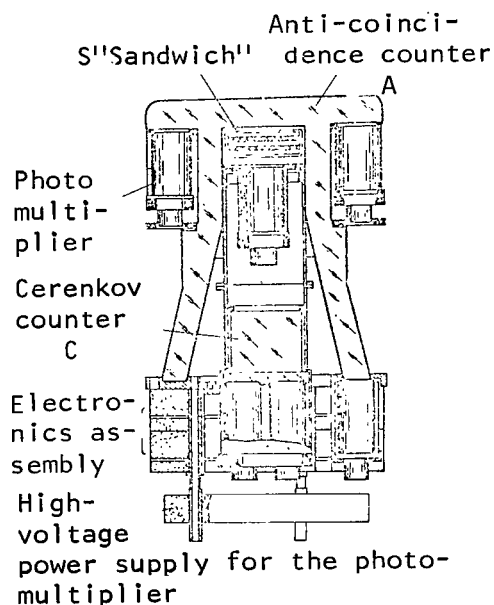


Figure 7. Diagram of the Kraushaar-Clark Experimental Device [25].

The main deficiency of the Kraushaar-Clark device is its poor angular resolution--the viewing angle of the counter telescope is 34° . Moreover, the device records γ -photons impinging at large angles to the axis of the device (right up to angle of 90°) with noticeable efficiency.

The natural element which would substantially improve the angular resolution of the device without decreasing the viewing angle and the geometric factor would be a track detector controlling the counter telescope, with whose help the trajectory of every electron-positron pair could be recorded and by which the direction of γ -photon arrival could be determined. The most suitable track detector for high altitude conditions is a spark chamber, because it is simple to manufacture, may be made sufficiently light and compact, does not require large amounts of electric power to operate and may be con-

trolled by the counter telescope. The angular resolution of a device with a spark chamber is determined by the accuracy of measuring the angle of the particle track which is equal to $1-2^\circ$ in typical multiple layered spark chambers, and of the order of 10^{-3} radians [28] in chambers with large interelectrode gaps, where the sparks are developed along the particle tracks. Spark chamber

/112

devices have been used in all recent experiments of measurement of the cosmic γ -photons [29-36].

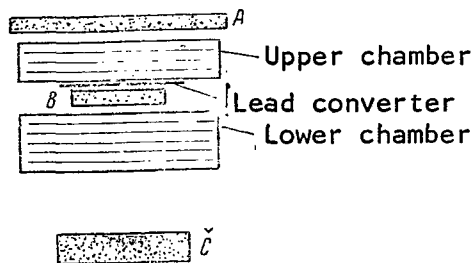


Figure 8. Diagram of the Cobb, Duthie and Stewart Experimental Device [29, 30].

Figure 8 shows the diagram of a device used in the experiment of Cobb, Duthie and Stewart [29, 30, 35]. The device consists of a lead converter 0.27 radiation lengths thick, a counter telescope which switches on a scintillation counter B and Cerenkov counter C, and an anticoincidence counter A and two spark chambers. The electronic circuit separates events of the type \overline{ABC} and feeds a high-voltage pulse to the spark chambers. The upper spark chamber mounted above the converter is used for additional control of the event caused by a neutral particle, and therefore makes it possible to decrease the requirement for the anti-

coincidence counter efficiency, which equaled 99.6% in the given experiment. The electron-positron pair, by which the direction of the γ -photon is measured relative to the axis of the device, is recorded in the lower spark chamber. Knowing the orientation of the device in space, the direction of γ -photon flight may be determined with an accuracy to several degrees. The overall error in measuring γ -photon direction consists of the error which occurs due to multiple Coulomb scattering of the components of the pair in the converter, inaccuracy in measuring the tracks in the spark chamber and inaccuracy in orientation of the device.

The efficiency of γ -photon conversion in the device was measured in a calibration experiment in an accelerated period. Figure 9 shows the measured dependence of the conversion coefficient η_c on γ -photon energy. It is $\eta_c = 17\%$ /113 for γ -photons with an energy of $E_\gamma \geq 100$ MeV.

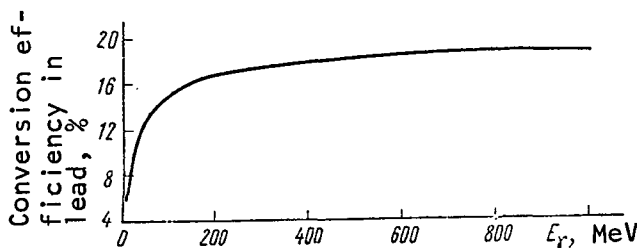


Figure 9. Dependence of the Conversion Coefficient of γ -Photons in Lead on Energy E_γ [30].

The Cerenkov counter in the device of Cobb et al [30] is a directional cut-off counter, which records relativistic particles passing through the radiator from top to bottom. The radiation occurring in the radiator from particles of the reverse flux are absorbed by the darkened upper surface of the radiator. Introduction of a directional counter into the telescope made it possible to eliminate imitations of γ -photon events by reverse fluxed

charged particles which passed through the telescope from top to bottom and remained in the converter.

After examination of the photographic films of spark chamber events, it became clear that only 10% of ABC events agree with cases of γ -photons entering the device. The remaining events are various background phenomena. Thus, due to its great clarity and reliability in interpretation of recorded events, the spark chamber makes it possible to operate in background conditions by an order exceeding the effect.

Spark chambers having different designs and modes of operation are used in devices for recording cosmic γ -ray photons. Of special interest is the use of spark chambers with automatic extraction of information--vidicon, sonic and filament spark chambers [28]. Devices with such spark chambers may be installed on non-returnable satellites, and all information is transmitted by telemetry to the ground station.

A vidicon spark chamber has been used in the Fazio device [32], designed for installation in the observatory satellite OAO, and in the Helmken and Fazio device [33] installed on a balloon. A schematic diagram of the latter device is given in Figure 10. A, B_1 , and B_2 are scintillation counters, γ is a total absorption Cerenkov counter with a radiator of heavy glass 10 radiation /114 lengths thick, and SC-1, SC-2 and SC-3 are spark chambers. $AB_1B_2\gamma$ events are separated by an electronic circuit which feeds a high-voltage pulsed power supply to the spark chambers. Spark chamber SC-1 with thin plates of an over-

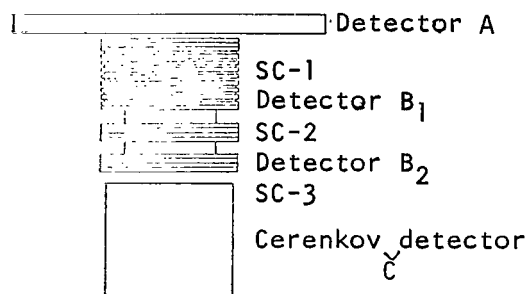


Figure 10. Diagram of the Fazio-Helmken Device [33].

all thickness of $1/3$ the radiation length acts as converter, and SC-2 and SC-3 are used to observe pairs and to measure the direction of the primary γ -ray photon. The spark chamber images in two orthogonal projections are fed to the photocathode of a liticon tube using a mirror system, where all the information about each event recorded by the chambers is converted into successive video signals and may be recorded, i.e., on magnetic tape. The coordinates of the sparks are measured in the liticon spark chamber with an accuracy to 1 mm, and the angles--with an accuracy to several degrees. A 512-channel Cerenkov counter amplitude pulse analyzer is used to determine γ -photon energy. The accuracy of energy determination is 30-50% for $E_\gamma \geq 50$ MeV. The geometric factor (luminous intensity) of the device is $G = 126 \text{ cm}^2/\text{sterad}$. A 7-watt radio transmitter, which transmits the data received from the vidicon, the amplitude analyzer and the counting circuits to a mobile ground station, is installed with the device. The transmitter output makes it possible to maintain communications with the device to 500 km. Total output required by the device is 73 watts.

The spark chamber used in the device of V. A. Bezus et al [36] (Figure 11) recorded not only the electron-positron pair, but also the electron shower

occurring in the lead plates of the chamber. The thickness of each lead plate is 4 mm, and the total amount of material in the chamber is equal to 3 radiation lengths. The upper space of a chamber 4 cm high is used to observe the pair and to measure the angle of γ -photon arrival. The sparks in the space travel at particle trajectories up to angles of 30° in the direction of the electrical field. Each of the next four spaces 2 cm high records the electron shower by which the γ -ray photon energy is determined. The accuracy of measuring energy calculated from theoretical and experimental cascade curves [37-40] is 70% for $E_\gamma \approx 70$ MeV and 25% for $E_\gamma \approx 700$ MeV. Verification of spark chamber operation in electron beams with energies of 100-640 MeV obtained in an accelerator indicated that it has an almost 100% efficiency of recording showers. The geometric factor of this device designed to register cosmic γ -ray photons with an energy of $E_\gamma \geq 1$ MeV is equal to $45 \text{ cm}^2/\text{sterad}$.

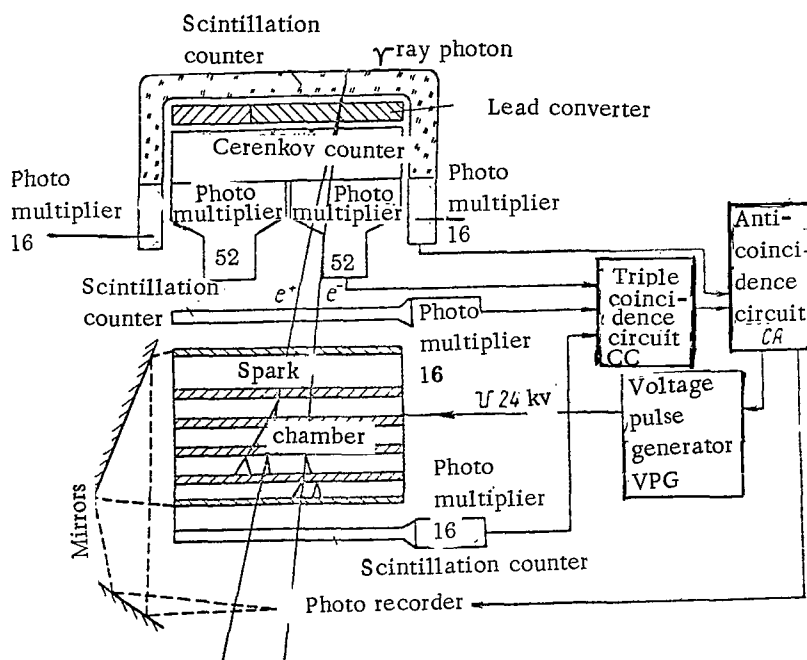


Figure 11. Block Diagram of the Device of Bezus et al [36].

The experimental devices enumerated have been installed on satellites or balloons. Specific operating conditions impose additional requirements on them--the devices should be of small size and weight, consume little electric power and be stable in the presence of vibration and impact loads.

8. Measuring the Intensity of Total Cosmic γ -Ray Photon Flux

A survey of the basic results of measuring cosmic γ -ray photon flux is given in Table 3, which cites simultaneously the authors and year of the experiment, the object on which the device was installed, the altitude of object ascent, expressed in the amount of atmosphere remaining, the geometric factor of the device and the energy of γ -ray photons recorded. The last column presents the intensities of cosmic γ -ray photon fluxes measured. Most of the experiments were conducted on balloons which ascended to altitudes of 30-40 km. Even at the point of highest ascent there remained above the apparatus 4-6 g/cm² of matter in which a significant number of secondary γ -ray photons were generated, so that measurement of the primary flux took place under conditions of an intense background. For this reason it was not possible in most of the experiments to measure the cosmic γ -ray photon flux and only its upper limits, exceeding the anticipated value of cosmic γ -ray photon flux by approximately 1 order, is given (See Table 1). In two experiments carried out on devices installed on artificial earth satellites [25, 27], it was also not possible to separate the primary γ -flux reliably from the background of albedo atmospheric γ -ray photons, but the value of the upper limit was reduced by almost an order compared with the other experiments and was close to the calculated value.

/116

Table 3
Survey of Experimental Data on Measurement of Cosmic
 γ -Ray Photon Intensity

Authors	Object	Altitude, g/cm ²	Geometric factor G, cm ² /sterad	E_{γ} , MeV	I_{γ} , cm ⁻² /sec × sterad ⁻¹
Cline, 1961 [23]	Balloon	8,5 ± 30	1,7	≥ 70	$(1 \pm 3) \cdot 10^{-3}$
Kraushaar, Clark, et al 1962 [25,26]	Satellite	0	$1 \pm 0,3$	≥ 40	$\leq (3,3 \pm 1,3) \times$
Duthie, Hafner, et al 1963 [24]	Balloon	4 ± 250	~82	≥ 60	$\times 10^{-4}$ $\leq 2 \cdot 10^{-3}$
Frye and Smith, 1965 [34]	Balloon				
Cobb, Duthie and Stewart, 1965 [29,30]	Balloon	3,6 6,5	— 25,8	≥ 30 ≥ 100	$\leq 5 \cdot 10^{-3}$ $\leq (1,8 \pm 0,2) \times$
Gregorov, et al, 1966 [27]	Satellite	0	7	≥ 50	$\times 10^{-3}$ $\leq (5 \pm 3) \cdot 10^{-4}$
Ögelman, Delvaille and Greisen, 1965 [31]	Balloon	10	—	≥ 1000	$\leq 3 \cdot 10^{-3}$
Duthie, Cobb and Stewart, 1966 [35]	Balloon	4,1	25,8	≥ 50	$(1,5 \pm 0,8) \cdot 10^{-4}$

The only experiment thus far to measure the final γ -ray photon flux of terrestrial origin is that of Duthie, Cobb and Stewart [35] carried out on the device for which the schematic diagram was given in Figure 8. Final selection of γ -ray photon events and measurement of γ -ray photon direction was carried out by the electron-positron pair recorded in the spark chamber. A certain excess of γ -ray photons above the average recorded flux was discovered in the section of the sky with coordinates of right ascension of $\alpha \approx 20^{\circ}15'$ and northern inclination of $\delta = 35^{\circ}$, which indicates their terrestrial origin. The excessive flux was equal to $(1.5 \pm 0.8) \cdot 10^{-4} \text{ cm}^{-2}/\text{s}^{-1}/\text{sterad}^{-1}$ and were obviously not completely reliable in a statistical sense. Because the indicated section in the constellation Signeus is located on the disc of the galaxy (the Milky Way), it is not clear whether the flux measured is a part of the total galactic flux or originates from a discrete source.

/117

9. Measurement of γ -Ray Photon Fluxes from Discrete Cosmic Sources

Discrete sources of γ -ray photons should be observed on the background of the overall galactic and metagalactic flux. Since the angular dimensions of discrete sources are small (i.e. Signeus-A has a dimension of $1'$, and M87-10'), and since the galactic flux is distributed more isotropically, those from discrete sources may be separated by using devices with good angular resolution. The required angular resolution of a device may be calculated by comparing expected fluxes from discrete sources with the average intensity of the galactic flux \bar{I} (See Tables 1 and 2). It happens that the output from discrete sources investigated in Table 2, and from the overall galactic flux are equal at an angular resolution of the device of 0.5 - 2° . A similar angular resolution is within the capabilities of a spark chamber.

Attempts to record γ -ray photon fluxes from certain cosmic objects considered to be possible discrete sources were undertaken in a number of papers [25, 26, 29, 30, 35]. Due to insufficient angular resolution of the devices and the intense background of secondary γ -ray photons, the final flux from any discrete source was not discovered. As a result of these experiments, only the upper limits of γ -ray photon fluxes were calculated from the objects investigated. Maximum flux was calculated by the formula

$$F_{\max} = \frac{N_{\gamma}}{\bar{F}_{\eta} \int A dt} \quad (3)$$

where N_{γ} is the number of γ -ray photons recorded during the time the object was within the field of view of the device; η is the conversion probability; $\int A dt$ is the effective area of the device during the exposure time; and F is the instrument factor. The results of measuring F_{\max} for different cosmic objects are given in Table 4. In addition to discrete sources, the table includes separate regions of the galaxy (the center of the galaxy, the pole), which is of interest in order to measure the anisotropy of the overall galactic flux. The average flux \bar{F} from all sectors of the sky observed is presented for comparison [26]. It is obvious from Table 4 that the maximum fluxes from

/118

discrete sources exceed the average value of \bar{F} . However, the low statistical accuracy of the experiment and possible systematic errors do not permit us to make a definite conclusion that the measured flux is related to a discrete source. Moreover, it should be noted that the measured fluxes F_{\max} exceed by many times the anticipated fluxes calculated in [6].

Table 4

Survey of Results of Measuring Cosmic γ -Ray Photon Fluxes From Discrete Sources

Object	$F_{\max}, \text{cm}^{-2}/\text{s}^{-1}$		
	$E_{\gamma} > 50, \text{ MeV}$ [25, 26]	$E_{\gamma} > 100 \text{ MeV}$ [20, 30]	$E_{\gamma} > 30, \text{ MeV}$ [34]
Cassiopeia-A	$25 \cdot 10^{-5}$	—	—
M31	$21 \cdot 10^{-5}$	—	—
Signeus-A	$18 \cdot 10^{-5}$	—	$2,2 \cdot 10^{-4}$
Crab Nebula	$22 \cdot 10^{-5}$	$4,9 \cdot 10^{-5}$	$1,5 \cdot 10^{-4}$
Large Magellanic cloud	$18 \cdot 10^{-5}$	—	—
Small Magellanic cloud	$19 \cdot 10^{-5}$	—	—
Sun	$12 \cdot 10^{-5}$	$5,3 \cdot 10^{-3}$	—
Center of galaxy	$16 \cdot 10^{-5}$	—	—
Northern galactic pole	$6,3 \cdot 10^{-5}$	—	—
Southern galactic pole	$12 \cdot 10^{-6}$	—	—
Orion (M42)	—	$2,9 \cdot 10^{-4}$	—
Rosette	—	$3,3 \cdot 10^{-4}$	—
IC-443	—	$1,2 \cdot 10^{-4}$	—
Mean flux \bar{F}	$5,1 \cdot 10^{-5}$	—	—
3C-147	—	—	$1,5 \cdot 10^{-4}$
3C-196	—	—	$1,5 \cdot 10^{-4}$

Conclusion

Although the cosmic γ -ray photon flux has not been reliably measured in experiments conducted thus far, the results of experiments even now permit us to make certain conclusions. Thus, the hypothesis of a fixed universe, according to which the density of matter in an expanding universe remains constant because of the self reduction of matter, has been refuted experimentally. /119 According to this hypothesis there should exist a flux of γ -ray photons generated during proton-antiproton annihilation, which would exceed by 500 times the maximum measured in the experiment of Kraushaar and Clark [10, 25, 26]. The maximum flux from the Crab Nebula measured in [30] was less than the expected flux calculated in certain theoretical papers [2], which forces us to reexamine the assumptions made from calculation.

Only five years have passed since the first experiment in γ -astronomy. Many experimental papers have been written, the number of which is constantly growing. The search for cosmic γ -ray photon fluxes is being conducted by many groups using different equipment, and there is every reason to hope that new important results will be obtained in the near future in γ -astronomy.

REFERENCES

1. Morrison, P., *Nuovo cimento*, Vol. 7, p. 858, 1958.
2. Savedoff, M. P., *Nuovo cimento*, Vol. 8, p. 12, 1959.
3. Ginzburg, V. L., *Uspekhi Fiz. Nauk*, Vol. 62, p. 37, 1957.
4. Hayakawa, S., K. Ito, and J. Terashima, *Suppl. Progr. Theor. Phys.*, Vol. 6, p. 28, 1958.
5. Pollack, J. B. and G. G. Fazio, *Phys. Rev.*, Vol. 131, p. 2684, 1963.
6. Ginzburg, V. L. and S. I. Syrovatskiy, *Uspekhi Fiz. Nauk*, Vol. 84, p. 201, 1964.
7. Hayakawa, S. et al, *Suppl. Progr. Theor. Phys.*, Vol. 30, p. 153, 1964.
8. Garmire, G. and W. L. Kranshaar, *Space Science Reviews*, Vol. 4, p. 123, 1965.
9. Friedman, G., *Uspekhi Fiz. Nauk*, Vol. 84, p. 505, 1964.
10. Rossi, B., *Space Research*, Vol. 5, p. 17, 1965.
11. Ginzburg, V. L., *Uspekhi Fiz. Nauk*, Vol. 89, p. 549, 1966.
12. Chudakov, A. E. et al, *J. Phys. Soc. Japan*, Vol. 17, Suppl. AIII, p. 106, 1962.
13. Fruin, J. H. et al, *Phys. Lett.*, Vol. 10, p. 176, 1964.
14. Long, C. D. et al, *Proc. Ninth-Intern. Conf. Cosmic Rays*, London, Vol. 1, p. 318, 1966.
15. Ginzburg, V. L., *Uspekhi Fiz. Nauk*, Vol. 74, p. 521, 1961.
16. Shklovskiy, I. S., *Uspekhi Fiz. Nauk*, Vol. 77, p. 3, 1962.
17. Hayakawa, S., *Proc. Intern. Conf. Cosmic Rays*, Jaipur, Vol. 3, p. 125, 1964.
18. Meyer, P., *Proc. Intern. Conf. Cosmic Rays*, London, Vol. 1, p. 61, 1966.
19. Zel'dovich, Ya. V., *Uspekhi Fiz. Nauk*, Vol. 89, p. 647, 1966.
20. Grinstejn, J., *Uspekhi Fiz. Nauk*, Vol. 83, p. 549, 1964.
21. Oda, M., *Proc. Ninth Intern. Conf. Cosmic Rays*, London, Vol. 1, p. 68, 1966.
22. Danielson, R. E., *J. Geogr. Res.*, Vol. 65, p. 2055, 1960.
23. Cline, T. L., *Phys. Rev. Lett.*, Vol. 7, p. 109, 1961.
24. Duthie, J. G. et al, *Phys. Rev. Lett.*, Vol. 10, p. 364, 1963; *Proc. Intern. Conf. Cosmic Rays*, Jaipur, Vol. 3, 1964.
25. Kraushaar, W. L. and G. W. Clark, *Phys. Rev. Lett.*, Vol. 8, p. 106, 1962.
26. Kraushaar, W. L. et al, *Proc. Conf. Cosmic Rays*, London, Vol. 3, p. 184, 1964.
27. Grigorov, N. L. et al, *Kosmicheskiye Issledovaniya*, 1967.
28. Dayon, M. I. et al, *Iskrovaya Kamera* [The Spark Chamber], Atomizdat Press, 1967.
29. Cobb, R., J. G. Duthie and J. Stewart, *Phys. Rev. Lett.*, Vol. 15, p. 507, 1965.
30. Cobb, R., J. G. Duthie and J. Stewart, *Proc. Ninth Intern. Conf. Cosmic Rays*, London, Vol. 1, p. 440, 1966.
31. Ogelman, H. B., J. P. Delvaille and K. J. Greisen, *Phys. Rev. Lett.*, Vol. 16, p. 491, 1965.

32. Fazio, G. G., *Proc. Conf. on Filmless Spark Chambers*, CERN, p. 49, 1964.
33. Helmken, H. F. and G. G. Fazio, "Preprint of the Smithsonian Astrophysical Observatory," Harvard University, 1965.
34. Frye, G. H. and L. H. Smith, *Bull. Amer. Phys. Soc.*, Vol. 10, p. 705, 1965.
35. Duthie, J. G., R. Cobb and J. Stewart, *Phys. Rev. Lett.*, Vol. 17, p. 263, 1966.
36. Bezus, V. A., *Materialy Vsesoyuznoy Konferentsii po Kosmicheskim Lucham* [Materials of the All-Union Conference on Cosmic Rays], *Izv. ANSSR Press, Alma-Ata*, 1967.
37. Rossi, B., *Chastity Vysokikh Energiy* [High-Energy Particles], *Gostekhnizdat Press, Moscow*, 1955.
38. Thom, H., *Phys. Rev.*, Vol. 136, B, p. 447, 1964.
39. Zaymidoroga, O. A. et al, *Preprint P-2633 of OIYAI*, 1966.
40. Beclin, E. E. and J. A. Earl, *Phys. Rev.*, Vol. 136, B, p. 237, 1964.

ABSORPTION OF π -MESONS BY COMPLEX NUCLEI

V. G. Kirillov-Ugryumov, F. M. Sergeyev and A. I. Fesenko

ABSTRACT. This paper surveys experiments on the study of π -meson absorption by complex nuclei. Absorption of π -mesons by light emulsion nuclei of C, N and O and by heavy nuclei of Ag and Br is investigated. This article describes experiments conducted in an emulsion chamber consisting of 90 layers of a 10×10 cm BR-400 nuclear emulsion exposed to a beam of π^+ -mesons. The distribution of stars according to the number of beams, the output and mass spectrum of secondary charged particles with an energy greater than 14 MeV in two-prong stars and the kinematics of two-prong stars are described. The authors conclude that there is a significant amount of π^+ -meson capture by pairs of nucleons in low-energy states.

1. Introduction

The study of π -meson absorption by complex nuclei is of great interest to determine the structure and properties of nuclei, and also the mechanism of certain nuclear reactions. π -Mesons have definite advantages as probing particles--they are bosons, their energy may be determined with high accuracy, and it is easy to control the kinematics of the reactions (especially in the case of slow π^- -meson absorption). Finally, it is very important that π -mesons have three charge states π^- , π^0 , and π^+ . This makes it possible to obtain a reaction with a double charge-exchange, i.e., reactions of the type

$$(Z,A) + \pi^+ \rightarrow (Z \pm 2,A) + \pi \pm .$$

It becomes possible in this case to observe the change of the nucleus charge by two units without a change of A. The existence of H_1^5 and H_1^4 nuclei was recently discovered; therefore, a n_0^4 system (and certain other neutron systems) may be more stable than was expected. The reaction of a double charge-exchange of π -mesons in nuclei may be very useful in the study of such systems. Thus, we may determine the energy of the bond of neutron complexes by the energies of π -mesons, in the reactions

$$\pi^- + He_2^3 \rightarrow n_0^3 + \pi^+;$$

$$\pi^- + He_2^4 \rightarrow n_0^2 + \pi^+.$$

This problem has been studied in detail in the survey of Ericson [1].

In the papers in which π^- -meson absorption by nuclei has been studied, the experimental data are analyzed on the traditional basis of the hypothesis of two stages of a high-energy nuclear reaction proposed by Serber [2] and developed in the papers of Brucner, Serber and Watson [3-5]. Total π -meson energy

in the first rapid stage is converted to the kinetic energy of a small group of nucleons with subsequent development of an internuclear cascade. As a result ($E > 30$ MeV) particles escape from the nucleus. In the second, slow stage the excited nucleus is converted to a basic state, emitting γ -photons, nucleons, α -particles, etc., as a result of the evaporation process. However, there is as yet no single opinion regarding the mechanism of π -meson absorption by nuclei in the first stage. The authors of most papers conclude that π -meson absorption in at least 70% of the cases results from a pair of nucleons, the probability of absorption by n-n- and p-p-pairs being 2 to 3 times less than by a n-p-pair [6-11]. In the papers of Ozaki and Weinstein [12] and P. I. Fedetov [13] the ratio R of the probabilities of π^- -meson absorption by n-p- and p-p-pairs was calculated for carbon nuclei:

/122

$$R^{[12]} = \frac{W_{np}}{W_{pp}} = 5,0 \pm 1,5;$$

$$R^{[13]} = 4 \pm 1,3.$$

These conclusions were made on the basis of the following experimental data.

1. Star distribution by the number of beams is characterized by an average number of beams equal to two for π^+ -mesons and to one for π^- -mesons.

2. Distribution according to the angle of diversions between particles in two-prong stars has a peak for angles greater than 140° .

3. The curve of energy distribution falls as energy increases. The maximum value of the energy transferred to the secondary particle during capture of slow π^- -mesons does not exceed 70 MeV. These results hardly change in the energy range of π -mesons studied (< 300 MeV).

Different conclusions were made in a number of investigations regarding the mechanism of π -meson absorption.

In the paper of Van Gan-Chan et al [14], the average number of beams in a star equal to 2.6 in the case of π^+ -meson absorption with an energy of 250-270 MeV by carbon nuclei is explained by the following mechanism of a nuclear reaction--total π -meson energy (~ 410 MeV) is distributed through all nucleons and produces a sudden nuclear burst.

In the papers of A. G. Varfolomeyev [15-17], where slow π^- -meson absorption by light nuclei of an emulsion of C, N and O were studied, the experimental data are explained on the assumption that the π^- -meson in 60% of the cases is captured by a single nucleon, strongly interacting with the remaining nucleus. The latter circumstance is necessary, because the total energy (~ 139 MeV) during capture of a slow π^- -meson is distributed in the form of kinetic energy. Concentration of all this energy in a single nucleon means that the nucleon acquires a pulse $P \approx 535$ MeV/c. The mean pulse of a nucleon inside the nucleus as a result of Fermi motion is equal to $P \approx 200$ MeV/c. It is

/123

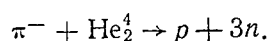
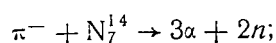
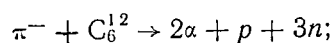
obvious that the law of preservation of the free nucleon pulse cannot be fulfilled; therefore, the nucleon is not free to absorb the π -meson.

The ambiguity of the conclusions is the result that the methodology used in each paper does not make it possible to obtain complete data to determine the mechanism of π -meson absorption. Knowledge of the nature of the nucleus-target, the charge, the mass and energy of the secondary particles is required in order to do this.

In the experiments carried out using scintillation counters [18-20], the intensity attenuation of the π -meson beam was measured and therefore it is impossible to separate π -meson absorption from other inelastic processes. Only high-energy particles were studied in Wilson cloud chambers [21-22], because a rather thick target of carbon absorbs low-energy particles. Severe difficulties arise in separating capture events by light C, N and O and by heavy Ag and Br nuclei when studying π -meson absorption by emulsion nuclei [23-27].

A number of experiments [28-31] on the study of π -meson absorption by nuclei were carried out using bubble chambers without a magnetic field. This does not permit identification of secondary particles by their masses and energy and angular characteristics of nuclear reactions are built up on the assumption that the secondary particles are protons.

The first separation of reaction products by their masses was completed in the experiment of Ammiraju and Lederman [32] during investigation of slow π^- -meson absorption by nuclei of carbon, nitrogen and helium in a diffusion chamber. Among the reaction products were registered protons, deuterons, tritons and α -particles. It turned out in this case that the following reactions are predominant:



On the basis of the data on the output of different particles, and the energy spectra of protons and α -particles, the authors concluded that the experimental results confirm qualitatively the α -particle model of a C_6^{12} nucleus in the two-nucleon model of π -meson absorption by nuclei. The angular distributions between beams of secondary particles also point to this. However, as the authors themselves point out, the unsuccessful configuration of the diffusion chamber resulted in many corrections. Severe difficulties also occurred in separating the hydrogen isotopes. The use of nuclear emulsions permits more reliable separation of secondary particles by mass. The experiment of A. O. Vaysenberg, et al [33] obtained a mass spectrum of secondary particles generated during capture of π^- -mesons by light C and O and by heavy Ag and Br emulsion nuclei, and it also determined the output of protons, deuterons and

tritons. The authors discovered a large (50%) output of deuterons and tritons with an energy > 20 MeV for C^{12}_6 and O^{16}_8 nuclei. The authors compare the experimental data obtained with calculations made on the basis of the theory of direct nuclear reactions proposed by I. S. Shapiro [34-36], and find satisfactory agreement with the experiment in the case when an α -particle is selected as the polar particle. According to the data of [33] about 65% of all splitting of C^{12}_6 and O^{16}_8 nuclei occurs as a result of π^- -meson capture by a virtual α -particle. However, experimental accuracy does not always permit a final conclusion in favor of a polar α -particle (i.e., it was not possible to explain the form of the energy spectrum of deuterons in such a manner). It should be noted that in almost all papers, with the exception of that of Tomar [37], where experimental data are compared with calculated data, only one of the possible mechanisms of π^- -meson absorption by nuclei is investigated, without consideration of the other channels of nuclear reaction, which cannot but effect final conclusions.

The problem of the mechanism of π -meson capture by nuclei has not been completely resolved and requires further experimental and theoretical study.

2. The Experiment

Absorption of π^+ -mesons by nuclei. Investigations were carried out using a nuclear emulsion. The emulsion chamber, consisting of 90 layers of a 10×10 cm BR-400 nuclear emulsion, was placed in a beam of π^+ -mesons of the OIYAI synchrocyclotron. The primary energy of π^+ -mesons was determined by the curves of the π^+ -meson paths in the emulsion. Figure 1 presents the differential curve of the π^+ -meson paths in the nuclear emulsion: $\Delta N/N$ is the relative number of π^+ -meson stops over a path of 0.4 cm. The mean path of π^+ -mesons is equal to $R = 7.9 \pm 0.9$ cm, which agrees with the average meson energy in a beam of $E_\pi = (82.0 \pm 6.0)$ MeV. Corrections taking into consideration the scattering effect on the particle path [38] were introduced when determining the mean path of π^+ -mesons. Absorption of π^+ -mesons by emulsion nuclei was recorded in a 2 cm wide strip at a distance of 1 cm from the forward edge of the emulsion layer relative to the π^+ -meson beam. The energy of the π^+ -mesons in this case was (70 ± 8) MeV.

Distribution of stars by number of beams. The track of a charged particle with a path of $R \geq 10$ microns was considered to be the beam. This agrees with the energy of the protons $E_p \geq 0.8$ MeV, of deuterons $E_d > 1$ MeV, of tritons $E_t > 1.5$ MeV, and of α -particles $E_\alpha > 3$ MeV.

/125

Cases of π^+ -meson interaction with nuclei were determined by two observers independently of each other. This made it possible to determine the total true number of events ($N = 734$). Distribution of the number of beams is presented in Figure 2. This distribution is characterized by an average number of beams per star of $\bar{n} = 3.3 \pm 0.2$.

The indicated result coincides with data of other experiments [29, 32], and indicates that a π^+ -meson is captured by a small complex of nucleons. The maximum number of beams observed per star is equal to 7.

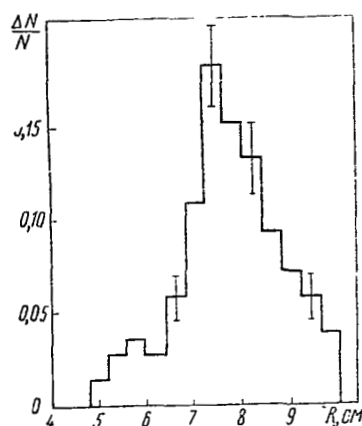


Figure 1. Differential Distribution of π^+ -Meson Paths in an Emulsion.

Output and mass spectrum of secondary charged particles with an energy greater than 14 MeV in two-prong stars. The study of two-prong stars is of special interest from the viewpoint of the study of direct processes. Cases of π^+ -meson interaction with nuclei were determined by scanning the emulsion by area. Two prong stars with a track length of $R \geq 10$ microns were recorded. A total of 1,300 stars were found. The track particles continued until they were stopped in the emulsion stack or exited from it. Thus, events of n-elastic π^+ -meson scattering in nuclei were excluded. Tracks with a residual path of $R \geq 0.1$ cm and an angle of inclination in the undeveloped emulsion of $\alpha \leq 30^\circ$ were selected for analysis of particles according to mass. A total of 463 particles were selected.

Measurement of secondary particle masses was accomplished by the multiple scattering method (the method of a constant sagitta).

The distribution of second differences \bar{D}_2 for secondary particles is given in Figure 3. Calibration was accomplished for further processing, for which protons contained in the primary beam and remaining in the emulsion were used. It turned out that distribution of second differences for these protons is described by the normal lull with parameters of $\langle \bar{D}_{2p} \rangle = 0.568$ microns and $\sigma = 0.100$ microns.

Figure 4 shows the distribution of second differences \bar{D}_{2p} for calibrated protons with a residual path of $R = 0.1$ cm. The solid curve is the normal distribution with an average value $\langle \bar{D}_{2p} \rangle = 0.568$ microns in a dispersion of

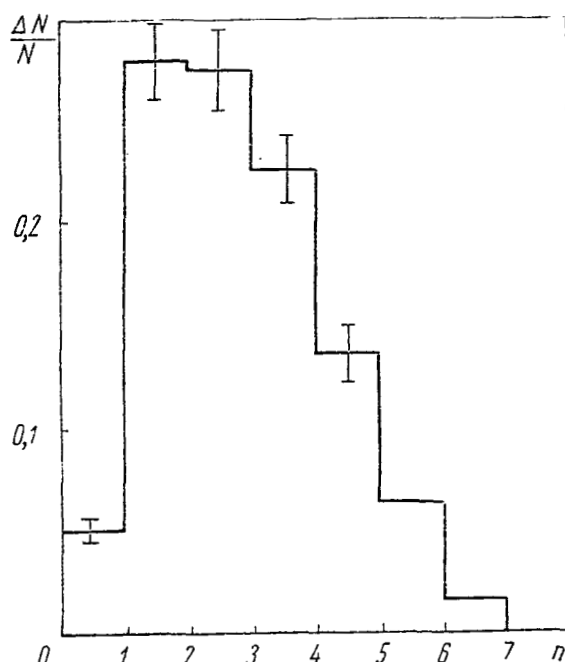


Figure 2. Distribution of Stars by the Number of Beams at a Track Length of $R \geq 10$ microns (Errors are Statistical).

$\sigma = 0.100$ microns. The method of least squares was used for further determination of the output of secondary particles on the assumption that p, d and t are generated in the reaction. We then know that measured distribution \bar{D}_2 is in the form

$$N(\bar{D}_2) = \alpha_p f_p(\bar{D}_2) + \alpha_d f_d(\bar{D}_2) + \alpha_t f_t(\bar{D}_2).$$

Here \bar{D}_2 is the value of second difference, f_p , f_d and f_t are distribution functions for protons of nuclei, deuterons and tritium, respectively, and α_p , α_d and α_t are the weights of specific states.

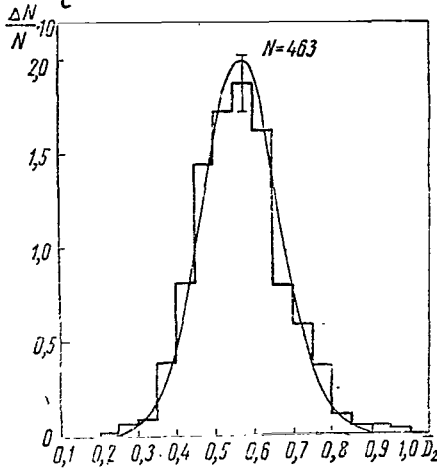


Figure 3. Distribution of Second Differences for Particles of Two-Prong Stars.. $N = 463$.

The law of distribution f for deuterons and tritium nuclei was assumed to be normal with parameters of $\langle \bar{D}_{2d} \rangle = 0.463$ microns, $\sigma_d = 0.070$ microns, $\langle \bar{D}_{2t} \rangle = 0.418$ microns, and $\sigma_t = 0.063$ microns.

It turned out as a result of calculation that the output of protons is $\alpha_p = (89.1 \pm \pm 7.0)\%$, and the output of deuterons $\alpha_d = (10.9^{+7.0}_{-4.0})\%$. Tritium nuclei were not discovered.

Kinematics of two-prong stars. In this paper we selected 125 two-prong stars, in which both particles were identified as protons, the tracks of which ended in the emulsion.

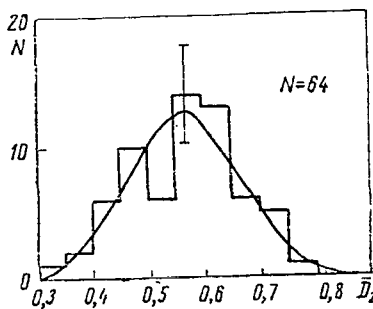


Figure 4. The Proton Line Measured in the Tracks of Calibrated Protons with a Residual Path of $R = 0.1$ cm.

Two protons may be generated as a result of π^+ -meson capture by a pair of n-p nucleons. If we assume that a π^+ -meson with an energy of 70 MeV is absorbed by a quasi-free n-p-pair, the maximum energy carried away by the proton is equal to 140 MeV. This energy value is approximately 200 MeV in the case of π^+ -meson capture by a single nucleon.

Energy distribution of protons in our experiment has a maximum value of $E_p \approx 150$ MeV. We can therefore assume that π^+ -meson capture by a single nucleon does not exist when two-prong stars are generated.

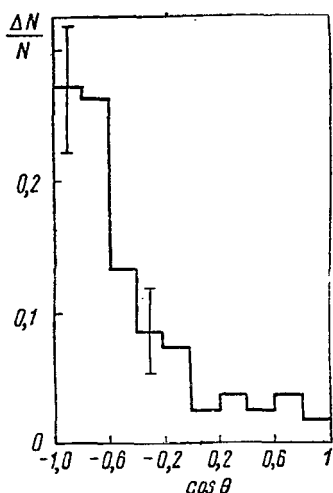


Figure 5. Distribution of Two-Prong Stars According to the Angle Between Two Protons.

Primary particle escape into the forward hemisphere is observed in angular distribution of proton escape. The coefficient of asymmetry is equal to $\alpha = N_B - N_H / N_b + N_H = 0.30 \pm 0.19$.

Anisotropy of the beams relative to the direction of π^+ -meson motion is not preserved when the energy of secondary particles changes. The coefficient of asymmetry is $\alpha = 0.28 \pm 0.03$ for 300 μ two-prong stars, on which no limits were placed relative to the paths and angles of inclination to the emulsion plane. This result agrees with the data obtained in [7, 29].

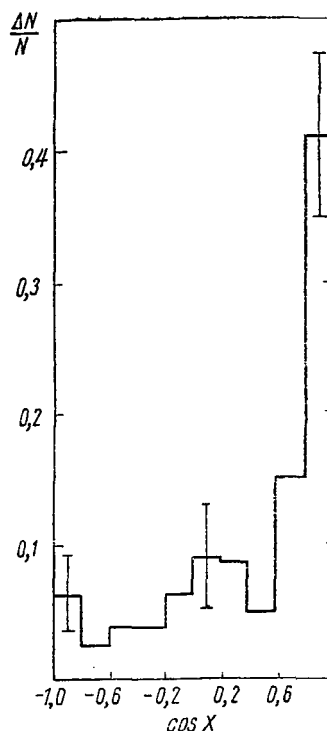


Figure 6. Angular Distribution Between the Total Pulse of Two Protons and the Direction of π^+ -Meson Motion.

Figure 5 shows the distribution of protons according to the space angle θ between them in a laboratory system of coordinates. It is obvious from the graph that approximately 70% of the cases has an angle of divergence $\theta \geq 120^\circ$. Proton distribution of this group of stars according to the angle between the beam and direction of π^+ -meson motion was isotropic (coefficient of asymmetry $\alpha = 0.18 \pm 0.15$). This circumstance indicates that the event selected occurred as a result of the direct process, without preliminary π^+ -meson scattering inside the nucleus. It was also discovered that the total pulse of two protons P_{2p} preserves the pulse path of the impinging π^+ -meson (Figure 6).

Distribution of total kinetic energy E_{2p} and total pulse P_{2p} of two protons is given in Figures 7 and 8. They are characterized by an average value of total energy $\bar{E}_{2p} \approx 115$ MeV and $P_{2p} \approx 330$ MeV/c, respectively. The lack of a balance of energy and pulse could be explained, assuming that neutrons are

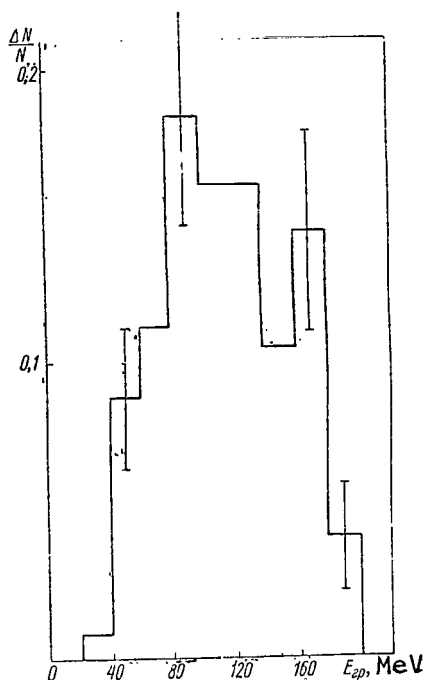


Figure 7. Distribution of Total Kinetic Energy of Two Protons in Two-Prong Stars.

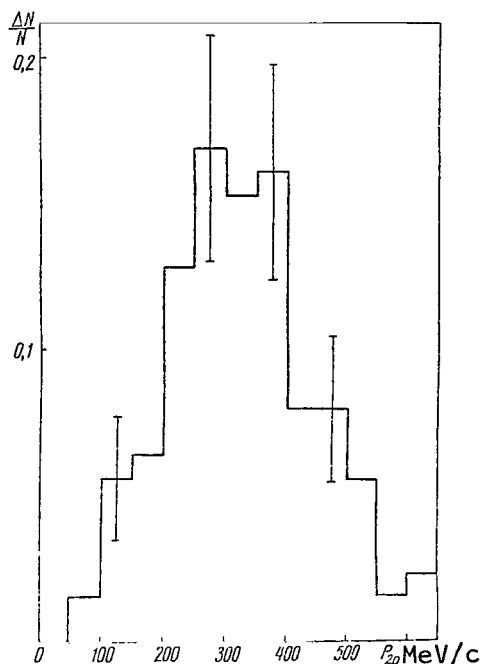


Figure 8. Distribution of Total Pulse of Two Protons.

present in the final state. However, this is apparently contradicted by the angular distributions of secondary particles. Thus, the measurement results obtained indicate qualitatively that no more than two rapid particles are generated in the final state. The nature of the energy spectrum in this case suggests the presence of a significant portion of π^+ -meson capture by pairs of nucleons in low-energy states.

REFERENCES

1. Ericson, T., *Proc. Intern. Conf. on High Energy Physics and Nuclear Structure*. CERN, p. 47, 1963.
2. Serber, R., *Phys. Rev.*, Vol. 72, p. 1114, 1947.
3. Brucner, K. A., R. Serber and K. M. Watson, *Phys. Rev.*, Vol. 81, p. 575, 1951.
4. Brucner, K. A. and K. M. Watson, *Phys. Rev.*, Vol. 83, p. 239, 1951.
5. Brucner, K. A., R. Serber and K. M. Watson, *Phys. Rev.*, Vol. 84, p. 258, 1951.
6. Demidov, V. S. et al, *Zh. Eksperim. i por Fiz.*, Vol. 46, p. 1220, 1964.
7. Salukvadze, R. G. and D. Nyagu, *Zh. Eksperim. i por Fiz.*, Vol. 41, p. 78, 1961.
8. Blinov, G. A. et al, *Zh. Eksperim. i por Fiz.*, Vol. 35, p. 880, 1958.
9. Petrov, I. I. et al, *Zh. Eksperim. i por Fiz.*, Vol. 37, p. 957, 1959.

10. Byfield, H., J. Kessler, and L. Lederman, *Phys. Rev.*, Vol. 86, p. 17, 1952.
11. Tenney, F. N. and J. Tinlot, *Phys. Rev.*, Vol. 92, p. 974, 1953.
12. Ozaki, S. and R. Weinstein, *Phys. Rev. Lett.*, Vol. 4, p. 533, 1960.
13. Fedetov, P. I., *Yadernaya Fizika*, Vol. 2, p. 466, 1965.
14. Van Gan-Chan, et al, *Zh. Eksperim. i por Fiz.*, Vol. 35, p. 899, 1958.
15. Varfolomeyev, A. G., *Zh. Eksperim. i por Fiz.*, Vol. 35, p. 540, 1958.
16. Varfolomeyev, A. G., *Zh. Eksperim. i por Fiz.*, Vol. 42, p. 713, 1962.
17. Varfolomeyev, A. G., *Zh. Eksperim. i por Fiz.*, Vol. 42, p. 725, 1962.
18. Izaacs, P. J., A. M. Sachs and J. Steinberger, *Phys. Rev.*, Vol. 85, p. 803, 1952.
19. Ignatenko, A. Ye., *Zh. Eksperim. i por Fiz.*, Vol. 31, p. 545, 1956.
20. Stork, D., *Phys. Rev.*, Vol. 93, p. 868, 1954.
21. Shapiro, A., *Phys. Rev.*, Vol. 84, p. 1063, 1951.
22. Kessler, J. and L. Lederman, *Phys. Rev.*, Vol. 94, p. 689, 1954.
23. Bernardini, G., E. T. Booth and L. Lederman, *Phys. Rev.*, Vol. 83, p. 1075, 1951.
24. Bernardini, G. and F. Levy, *Phys. Rev.*, Vol. 84, p. 610, 1951.
25. Bradner, H. and B. Rankin, *Phys. Rev.*, Vol. 87, pp. 547, 553, 1952.
26. Morrish, A. H., *Phys. Rev.*, Vol. 90, p. 674, 1953.
27. Podgoretskiy, M. I. et al, *Zh. Eksperim. i por Fiz.*, Vol. 31, p. 756, 1956.
28. Dzhelepov, V. P. et al, *Zh. Eksperim. i por Fiz.*, Vol. 31, p. 923, 1956.
29. Labberig-Frolova, Zh. V. et al, *Zh. Eksperim. i por Fiz.*, Vol. 31, p. 634, 1959.
30. Balandin, M. B. et al, *Zh. Eksperim. i por Fiz.*, Vol. 46, p. 415, 1964.
31. Meshkovskiy, A. G. and Ya. Ya. Shalamov, *Zh. Eksperim. i por Fiz.*, Vol. 37, p. 978, 1959.
32. Ammiraju, P. and L. Lederman, *Nuovo cimento*, Vol. 4, p. 283, 1956.
33. Vaysenberg, A. O., E. D. Kolganova and N. B. Rabin, *Zh. Eksperim. i por Fiz.*, Vol. 47, p. 1262, 1964.
34. Shapiro, I. S., *Zh. Eksperim. i por Fiz.*, Vol. 41, p. 1616, 1961.
35. Shapiro, I. S. and V. Kolybasov, *Zh. Eksperim. i por Fiz.*, Vol. 44, p. 270, 1963.
36. Shapiro, I. S., *Teoriya Prymyikh Yadernykh Reaktsiy* [The Theory of Direct Nuclear Reactions], *Godatomizdat Press*, 1963.
37. Tomar, *Phys. Rev.*, Vol. 77, p. 412, 1950.
38. Pomeranchuk, I. Ya., *Zh. Eksperim. i por Fiz.*, Vol. 18, p. 159, 1948.

STUDY OF THE PHYSICAL AND CHEMICAL PROPERTIES OF THE SURFACES OF SOLIDS USING NUCLEAR γ -RESONANCE [THE MOSSBAUER EFFECT]

I. P. Suzdalev

ABSTRACT. This paper reviews research in the field of surface effects as displayed by non-transfer nuclear γ -resonance (the Mossbauer effect) in applications to atoms located on the surfaces of solids. This paper considers the two groups of the parameters of NGR spectra. The first group is characterized by atomic oscillation on the surface, by the forces linking the atom to the surface and by diffusion along the surface. The second group characterizes the electron state of an atom on the surface, the nature of its environment, and the presence of electrical and magnetic interaction of the nucleus with its electron shell.

1. Introduction

Non-transfer nuclear γ -resonance (the Mossbauer effect) has recently begun /131 to be used intensively to study the different types of phenomena on the surfaces of solids, and also of highly dispersed systems and thin films. We know that the Mossbauer effect is the emission or absorption of non-transfer γ -quanta [1], i.e., it is a purely nuclear effect. However, the exceptional sharpness of resonance tuning caused by the small value of the ratio of the level width to the radiation energy permits the study of the electron envelope of nuclei, the characteristics of the chemical bond, and of electrical and magnetic fields [2]. Applicability of NGR to investigation of surface phenomena is based, in the first place, on the rather high sensitivity of the probability of the effect and width of the spectrum lines to the nature of the oscillations and atomic diffusion on the surface, and secondly, on the sensitivity of the type of spectrum to the nature of the chemical bond and the presence of electrical and magnetic fields. There are however two substantial restrictions on the applicability of the method to investigation of surface phenomena--the limited number of resonance nuclei suitable for study (iron, tin and gold are presently being used), and the requirement for sufficient density of nuclei ($\sim 10^{18}$ particles per cm^2) in the absorbent, which requires that materials having a highly developed surface--hundreds of square meters per 1 gr--be used. These are highly dispersed systems of metals, oxides, salts, silicagel, aluminogels, zeolites, unrestricted ion exchangers and ion exchange resins. By using a radiation source as the material being investigated, we can increase the sensitivity of the method, but this is less convenient.

Despite the fact that only the first steps have been made in the field of using NGR to investigate the surfaces of solids, some basic trends may already be formulated.

121

1. The structure of adsorbents.
2. The dynamics of atomic motion on the surface and surface diffusion.
3. Elementary processes of absorption and catalysis. The chemistry of surface compounds.
4. Highly dispersed systems and films.
5. Topochemical reactions.

Before turning to a survey of experiments in the field of surface effects, let us dwell briefly on the characteristics of the parameters of NGR spectra when applied to atoms on the surface.

It is feasible to separate spectrum parameters into two groups:

The first group characterized atomic oscillations at the surface, the forces binding the atom to the surface, and surface diffusion. These are the probabilities of the effect f , the Doppler shift of the second order δE_D , spectrum asymmetry A_a (due to the anisotropy or the Debye-Waller factor), and the line with G;

The second group characterized the electron state of the atom at the surface, the character of its environment, and the presence of electrical and magnetic interactions of the nucleus with its electron envelope. This is an isomeric or chemical shift δE_I , quadrupole splitting of the spectrum ΔE_Q , magnetic splitting of the spectrum ΔE_μ , and asymmetry of the spectrum A_p (due to relaxation processes).

Probability of the Effect

The common expression for the probability of emission and absorption of non-transfer γ -quanta is given by the formula [3]

$$f = \exp\left(-\frac{\langle x^2 \rangle}{\hbar^2}\right),$$

where $\langle x^2 \rangle$ is the mean square vector of atomic displacement, and π is the square of the wave length.

For a harmonic oscillator with a single frequency ω and a mass m [4, 5] $\langle x^2 \rangle = \hbar/2m\omega \coth \hbar\omega/2kT$, which at high temperatures yields $\langle x^2 \rangle = kT/m\omega^2 \sim \sim kT/\kappa$, where κ is the force constant.

Using this simple model, we may qualitatively characterize the dynamics of atomic motion at the surface. Atoms at the surface of a solid may occupy two

positions--on the surface (Figure 1 a and b) and in the surface (Figure 1, c and d). The position of an atom inside the solid is also shown in Figure 1, e for comparison. If we examine a simple cubic lattice and assume that κ is proportional to the number of bonds with close neighbors of a given atom and with neighbors following the latter, the bond aligned perpendicular to motion being ignored, then for different positions of an atom at the surface and for different directions of oscillations we obtain different values of κ :

/133

- a $\kappa \sim 1 + 4 = 5$ bonds;
- b $\kappa \sim 0 + 2 = 2$ »
- c $\kappa \sim 1 + 4 = 5$ »
- d $\kappa \sim 2 + 6 = 8$ »
- e $\kappa \sim 2 + 8 = 10$ »

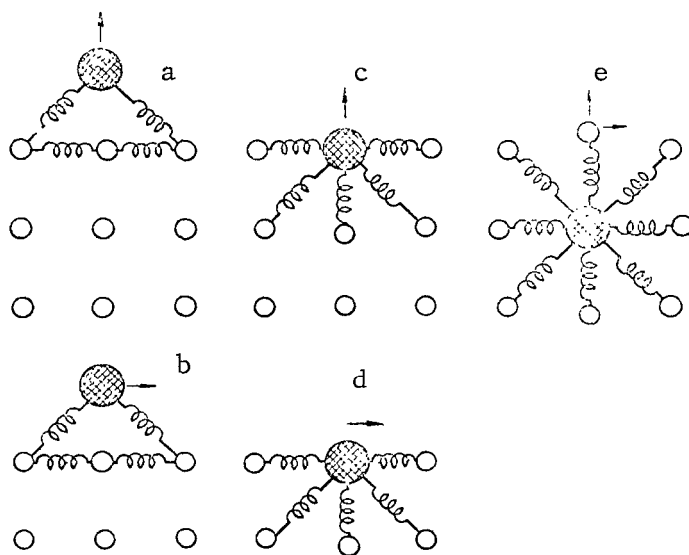


Figure 1. Three Types of Atomic Bonds at the Surface of and Inside a Solid.

Thus, $\langle x^2 \rangle$ for surface atoms increases noticeably and becomes 1.2-5 times greater than for internal atoms, and anisotropy of atomic oscillations at the surface occurs. The amplitude of oscillations perpendicular to the surface is greater for atoms at the surface (Figure 1, b and d) than the amplitude of atomic oscillations parallel to the surface

$$\frac{\langle x^2 \rangle_{\perp}}{\langle x^2 \rangle_{\parallel}} \sim \frac{\kappa_{\parallel}}{\kappa_{\perp}} = \frac{8}{5}.$$

On the other hand the amplitude of atomic oscillations at the surface parallel to it (Figure 1, a and c) is greater than that in a direction perpendicular to the surface /134

$$\frac{\langle x^2 \rangle_{\perp}}{\langle x^2 \rangle_{\parallel}} \sim \frac{z_{\parallel}}{z_{\perp}} = \frac{2}{5}.$$

Rice [6] investigated the model of a semi-infinite cubic lattice taking into consideration the interactions only with close neighbors and determined that $\langle x^2 \rangle$ is noticeably greater for surface atoms than for those inside a solid, the difference increasing as temperature increases. For example, the probability of the effect where $T = 93^\circ \text{ K}$ for internal atoms exceeds the probability of the effect by 26% for atoms at the surface. As temperature increases to $T = 284^\circ \text{ K}$, this difference increases to 60%. However, as the atom moves away from the surface into the solid, the difference in values of $\langle x^2 \rangle$ between internal and surface layers diminishes rapidly and almost coincides (with an accuracy to 0.01%) after the fifth layer from the surface of a value of $\langle x^2 \rangle$ for surface and internal atoms. Maradudin [7] investigated a model of a central-type cubic lattice with consideration of interaction with close neighbors and those following close neighbors. The anisotropy of oscillations of surface atoms was considered in comparison with the preceding model [6]. Since the mean square of atomic displacement at that time for the first layer perpendicular to the surface $\langle z^2 \rangle$ is two times greater than for internal atoms, this difference is approximately 30% for the mean squares of atomic displacements in the plane of the surface-- $\langle x^2 \rangle$ and $\langle y^2 \rangle$. As in the preceding model, the difference in mean squares of displacements for surface and internal atoms disappears at the fifth layer from the surface. Clark, et al [8] carried out similar calculations for atoms at the surfaces (100, 110, 111) of a monocrystal of silicon.

Doppler Shift of the Second Order

Doppler shift of the second order is given by the expression

$$\delta E_D = \frac{E_\gamma}{2c^2} \langle V^2 \rangle;$$

E_γ is the energy of γ -transition, and $\langle V^2 \rangle$ is the mean square of the velocity of resonance nuclei.

For a harmonic oscillator with a single frequency ω and mass m [3]

$$\langle V^2 \rangle = \frac{\hbar \omega}{2m} \coth \frac{\hbar \omega}{2kT}.$$

At high temperatures

/135

$$\langle v^2 \rangle \sim \frac{kT}{m} + \frac{\hbar^2 \omega^2}{12mkT} = \frac{kT}{m} + \frac{\hbar^2 \kappa}{12mkT}.$$

Assuming κ to be proportional to the number of bonds, we conclude that δE_D is less for surface atoms than for internal atoms. The second term in this formula is a quantum correction. However, it is very important, because it permits us to calculate the dynamic matrix from which we can derive the equation of motion in real crystals.

Asymmetry of Quadrupole Splitting

In connection with the fact that $\langle X^2 \rangle$ for surface atoms has a clear anisotropy, it is natural to expect a noticeable asymmetry of spectrum components with quadrupole splitting due to the anisotropy of the Debye-Waller factor [9-11]. This phenomenon is called the Gol'danskiy-Karyagin effect.

When there are many surfaces oriented in a different manner for transition of $3/2 \rightarrow 1/2$ M1, the asymmetry is given by the relation

$$A = \frac{I_\pi}{I_\sigma} = \frac{\int_0^\pi (1 + \cos^2 \theta) f(\theta) \sin \theta d\theta}{\int_0^\pi \left(\frac{5}{3} - \cos^2 \theta \right) f(\theta) \sin \theta d\theta}.$$

Here π is the transition of $(\pm 3/2) \rightarrow (\pm 1/2)$, σ is the transition of $(\pm 1/2) \rightarrow (\pm 1/2)$, and θ is the angle between the direction of γ -quantum escape and the electric field gradient.

It is necessary and sufficient that $f = f(\theta)$ for asymmetry to occur [10]. In order to determine A from the spectrum, it is necessary however to know the direction of the electrical field gradient and its sign in order to determine to which line the transition of $\pm 3/2 \rightarrow \pm 1/2$ and $\pm 1/2 \rightarrow \pm 1/2$ correspond.

Writing $f(\theta) = \exp(-k^2 x^2)$, we obtain

$$A \approx \frac{\int_0^1 (1 + u^2) \exp(-\epsilon u^2) du}{\int_0^1 \left(\frac{5}{3} - u^2 \right) \exp(-\epsilon u^2) du},$$

where $u = \cos \theta$, $\epsilon = k^2 [\langle z^2 \rangle - \langle x^2 \rangle]$ and $\langle z^2 \rangle$ and $\langle x^2 \rangle$ are the squares of the amplitudes of atomic oscillations in the direction of the electrical field gradient and perpendicular to it. Numerical values of $A = f(\epsilon)$ [12] are given in Figure 2. As the temperature increases, the anisotropy of the Debye-Waller factor should increase, and asymmetry of the spectrum increases.

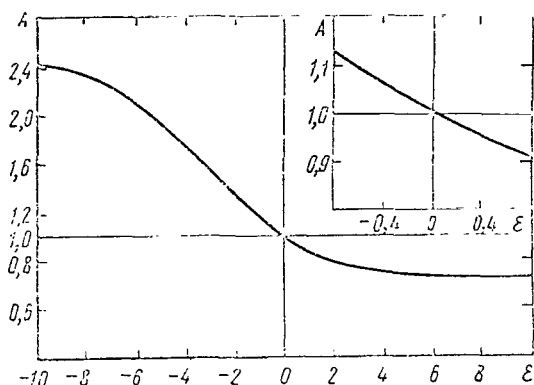


Figure 2. Dependence of Asymmetry of the NGR Spectrum on $\varepsilon = k^2(\langle z^2 \rangle - \langle x^2 \rangle)$.

Line Width

Surface atoms may diffuse along the surface of a solid as a result of jumps from one localized position to another, which leads in certain cases to widening of the NGR line. The coefficient of self-diffusion is $\sim 10^{11}-10^{12}$ cm²/sec for atoms inside a solid, which is several less than the value required for observation of line spread. Coefficient of self-diffusion increases sharply near the point of fusion, but it is difficult to discern line spread, because the probability of the effect becomes very small. Line spread of the NGR spectrum at a sufficiently large value of the effect, due to the specifics of the atomic bond at the surface

may be observed in the case of surface atoms in connection with the common low activation energies for self-diffusion--several kilocalories per mole.

In the case of diffusion as a result of jumps (self-diffusion), the probability of the effect $f \approx e^{-2w} \cdot e^{-\Gamma_D |t|}$. If l is the distance between two centers of localization, $\Gamma_D = 6D/l^2$, where D is the coefficient of diffusion.

Maximum line spread in this case [13]

$$\Delta \varepsilon_p \approx \frac{2h}{\tau},$$

where $\tau = 1/\Gamma_D$ is the arrival time of the atom or molecule at the point on the surface until its transition to another point. For example, we can discern a spread for Fe⁵⁷ (natural level width of $\Gamma = 4.5 \cdot 10^{-9}$ ev), if $2\Gamma + \Delta \varepsilon > 10^{-8}$ ev, which yields $\tau < 1.4 \cdot 10^{-7}$ sec, and $D > 1.2 \cdot 10^{-9}$ cm²/sec ($l \sim 4 \cdot 10^{-8}$ cm). /137

In practice however the lines are almost never of natural width, which may depend on the spectrometer, the radiation sources, the thickness of the model being studied, the presence of crystalline fields which widen the line, etc. Therefore, the coefficient of diffusion should be several times greater than $1.2 \cdot 10^{-9}$ cm²/sec, in order to discern a spread because of diffusion. Determining $D = f(T)$ from the experiment, we can calculate the activation energy Q for a given diffusion process. Activation energy may also be found from the value of τ ($\tau = \tau_0 \exp Q/RT$), where R is the gas constant, and T is temperature.

Isomeric Shift

Let us now turn to the second group of parameters of NGR spectra, related to the electron environment of a resonance nuclei.

The chemical shift is given by the expression [14]

$$\delta E_I = \frac{2}{3} \pi Z e^2 [\langle r_{\text{exc}}^2 \rangle - \langle r_b^2 \rangle] (|\psi(0)_a|^2 - |\psi(0)_s|^2).$$

Here Ze is the charge of the nucleus $\langle r_{\text{exc}}^2 \rangle$ and $\langle r_b^2 \rangle$ are the mean square radii of the resonance nuclei in excited and basic states, $|\psi(0)_a|^2$ and $|\psi(0)_s|^2$ are the squares of the wave functions of electrons in the nucleus for the absorbent and the source. There are as yet no experimental data on the change of δE_I for surface bonds having a single chemical formula with polycrystalline compounds. Actually, it is difficult to anticipate the change of chemical shift in the case of a fixed close environment of the resonance nuclei.

Quadrupole Splitting

In connection with the fact that the surface of a solid has a clearly defined anisotropy, we may expect in most cases axial symmetry of the electrical field gradient aligned perpendicular to the surface. For a nucleus having a quadrupole moment Q , spin I , and a magnetic quantum number m , the quadrupole level shift is

$$\delta E_Q = e \frac{\partial^2 V}{\partial z^2} \cdot \frac{Q}{[4I(2I-1)]} [3m^2 - I(I+1)],$$

and quadrupole splitting, i.e., for nuclei with

$$I = \frac{3}{2} \Delta E_Q = \frac{1}{2} e \frac{\partial^2 V}{\partial z^2} Q.$$

Quadrupole splitting may be greater due to polarization of internal d-electrons /138 by the external crystalline field.

There will be a deficiency of p-electrons and $\partial^2 V / \partial z^2 > 0$ along the axis of z (perpendicular to the surface) for the case of an atom located on the surface, if p-orbits (i.e., in the case of SnO at the surface) are part of the bond.

In distinction from the chemical shift $\partial^2 V / \partial z^2$ increases substantially for surface bonds, because an atom at the surface is in a less symmetrical environment than one inside a solid, which yields large values of ΔE_Q .

Magnetic Splitting

Magnetic splitting between two neighboring sublevels is

$$\Delta E_\mu = \frac{\mu_I}{I} H; \quad \mu_I = g_I \mu_0 I.$$

where μ_0 is the nuclear bohr magneton, g_I is the nuclear level g-factor with a spin of I , and μ_I is the magnetic moment of the nucleus.

Since the surface is formed by a two-dimensional lattice, we should not expect to find magnetic fields in nuclei which could cause magnetic splitting for atoms located on the surface. The spin wave theory of ferromagnetism predicts that ferromagnetism is a three-dimensional effect in that a two-dimensional lattice may not have a spontaneous magnetization. It was shown [15] that magnetization drops off sharply when the thickness of the lattice becomes less than 5 constants of the lattice. However, in the case of slightly porous adsorbents, i.e., for zeolites, where the dimensions of the pores are 5-15 Å, and of highly dispersed systems of certain metals and oxides, we can expect a magnetic field in the nucleus at low temperatures. As temperature decreases spectrum asymmetry with quadrupole splitting may also occur due to increase of relaxation time of electron spin [16, 17].

Let us now turn to the experimental papers in the field of investigating the surface of a solid using NGR.

Adsorbent Structure

Papers [18, 19] investigated zeolites of Y (faugazite) and M (mordenite) with cations of iron and ion-exchange resins of KB-4 and KU-2 with cations of iron, and AV-16 and AV-17 with anions of $(\text{FeCN}_6)^{-3}$, $(\text{FeCN}_6)^{-4}$ and $(\text{SnCl}_6)^{-2}$.

We know that zeolites (molecular screens) are crystalline structures with poor dimensions of 5-15 Å. There are cations of metals in zeolites in order to compensate the negative charge of tetrahedrons $[\text{AlO}_4]^{-1}$. Cations of iron were introduced in the zeolite by cation exchange of Na for Fe enriched by 89% by isotope Fe^{57} . Spectra of Fe^{57}M and Fe^{57}Y were obtained with a source of Co^{57} in Cr up to and after adsorption of $(\text{CH}_3)_4\text{Sn}$, CH_3OH and $n\text{-C}_6\text{H}_{14}$. Figure 3 shows the spectra of Fe^{57}Y , $\text{Fe}^{57}\text{Y} + n\text{-C}_6\text{H}_{14}$ and the spectrum of the adsorbent $(\text{CH}_3)_4\text{Sn}$ in Fe^{57}Y . The appearance of NGR-spectra of iron after adsorption of these sorbents changes substantially. New lines appear which are characteristic for $\text{Fe}^{2+}(\Delta E_Q \sim 1.5 \text{ mm/sec at } 93^\circ \text{ K})$, the intensity of which is much more dependent on temperature than that of Fe^{3+} lines. Moreover, the type of adsorbent of Y and M has a much stronger effect on the appearance of the Fe^{2+} spectrum than on the appearance of the molecule adsorbed. The Fe^{2+} spectrum in zeolite M yields more quadrupole splitting ($\Delta E_Q \sim 3 \text{ mm/sec at } 93^\circ \text{ K}$) than in zeolite Y ($\Delta E_Q \sim 2.5 \text{ mm/sec, } 93^\circ \text{ K}$). The Mossbauer spectrum of Sn^{119} for tetramethyl tin, adsorbed in zeolite Fe^{57}Y (See Figure 3), when compared with the data of [22], indicate in the given case that the tin is linked with the oxygen complex of $[\text{AlO}_4]^{-1}$. This so far as we know is the first experiment when the state of the adsorbent (zeolite Y) as well as that of the adsorbate-- $(\text{CH}_3)_4\text{Sn}$ has been studied according to the NGR spectra of different isotopes.

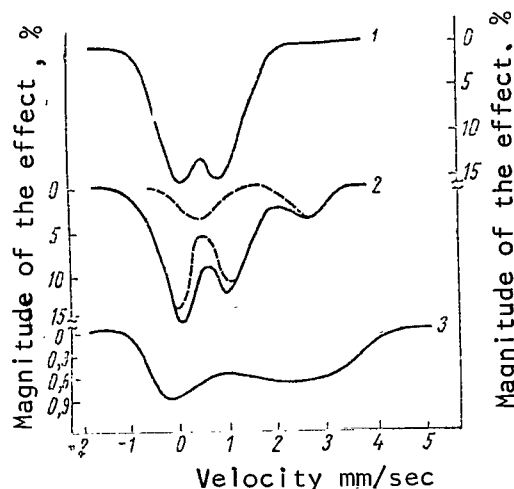


Figure 3. Nuclear γ -Resonance Spectra of Zeolite Y: 1, Fe^{57}Y Before Adsorption, 93°K (NGR of $E = 14.4\text{ keV}$); 2, $\text{Fe}^{57}\text{Y} + (\text{CH}_3)_4\text{Sn}$ After Adsorption of $(\text{CH}_3)_4\text{Sn}$ (NGR of $E_\gamma = 14.4\text{ keV}$); 3, $\text{Fe}^{57}\text{Y} + (\text{CH}_3)_4\text{Sn}$ After Adsorption of $(\text{CH}_3)_4\text{Sn}$ (NGR of $E_\gamma = 23.8\text{ keV}$). The dotted lines denote individual spectra superposition of which gives the observed (by points) complex spectra, indicated by the solid lines.

It is difficult to imagine that during adsorption, for example, of n-hexane, reduction of a Fe^{3+} ion to Fe^{2+} may occur, and therefore the natural assumption remains that Fe^{2+} ions were in the zeolite even before adsorption of $(\text{CH}_3)_4\text{Sn}$ and C_6H_{14} , but they did not give NGR spectra, since they were in a non-localized position before adsorption [20, 21]. This conclusion is strengthened by the sharp temperature dependence of the probability of the Mossbauer effect for Fe^{2+} . After adsorption, localization of Fe^{2+} ions takes place in the zeolite channels and spectra "appear", characteristic for non-localized states of Fe^{2+} . Strong quadrupole splitting of Fe^{2+} into Fe^{57}M compared to Fe^{57}Y occurs in connection with less symmetry in the channels of mordenite (an ellipse) than in the channels of Y (a circle). The weak temperature dependence of the value of the effect for Fe^{3+} characterizes the rather strong bond of Fe^{3+} with the zeolite lattice, i.e., trivalent ions of iron are located in all probability in localized positions.

The temperature dependence of $\Delta E_Q^{2+} = f(T)$ was studied. In all models ΔE_Q^{2+} increased sharply as temperature decreased. Thus $\Delta E_Q =$

$$= 1.68 \pm 0.09 \text{ mm/sec } (293^\circ\text{K}) \text{ and}$$

$\Delta E_Q = 2.98 \pm 0.09 \text{ mm/sec } (93^\circ\text{K})$ for a spectrum of Fe^{2+} into $\text{Fe}^{57}\text{M} + \text{CH}_3\text{OH}$.

A similar temperature dependence is characterized by the change of the input of the electric field of gradients determined by different electron energy levels of a Fe^{2+} ion into total gradient, according to the Boltzmann multiple $e^{-\Delta/kt}$, where Δ is the position of the electron energy level.

Ion exchange in ion-exchange resins (cationites) [19] was accomplished by dissolving Fe_2O_3 , enriched by 89% by a Fe^{57} isotope in hydrochloric acid, and with subsequent exchange in this solution of Na ions and a resin proton for Fe^{3+} . A highly dispersed form of iron hydroxide was also obtained in the resin pores after processing of the NaOH cationites. Ion exchange was conducted in the anionites from aqueous solutions of $\text{K}_4(\text{FeCN}_6)$, $\text{K}_3(\text{FeCN}_6)$ and $(\text{NH}_4)_2\text{SnCl}_6$.

Ion-exchange resins in distinction from zeolites are amorphous polymers, in which the basic chain with fixed ions (negatively charged for cationites and positively charged for anionites) are cross-linked by bridges, i.e., by divinyl benzene. However, degradation may occur in the process of resin synthesis, and readily oxidizable groups appear in the region of the cross-links. As a result further reduced groups appear in the resin instead of functional, ion-exchange groups. Actually, as the NGR spectra in Figure 4 indicate, there are such groups in KU-2 resin which reduce Fe^{3+} to Fe^{2+} . In connection with the simplicity of finding Fe^{2+} in the NGR spectrum of iron, this method may be used to analyze the oxidizing degradation of the resin during synthesis.

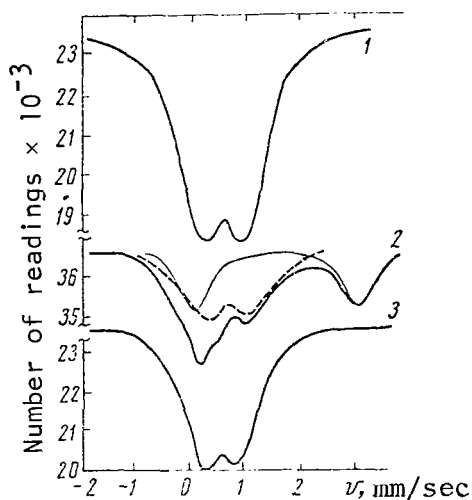


Figure 4. NGR Spectra of Cationites at $T = 77^\circ \text{K}$: 1, KB-4; 2, KU-2 (the spectrum is superposed on the constituent components--the Fe^{3+} spectrum is the dotted line and the Fe^{2+} spectrum is the solid thin line); 3, $\text{Fe}(\text{OH})_3$ in KU-2.

Experimental results indicate a substantial difference in the values of the effect for KU-2 and KB-4. The value of the effect for KB-4 resin is much greater, and its temperature dependence is somewhat weaker than for Fe^{3+} in KU-2. This refers to the more stable bond of the iron ion in resin with carboxyl groups compared with sulfo resin, since the bond strength of functional groups with a polymer network in both resins is almost identical. There is an even greater difference between KU-2 and KB-4 when they interact with water. Swelling of KU-2 in water leads to total disappearance of the effect. This indicates the sharp increase of the mean square of displacement of the resinous atom, and, subsequently, agrees with the concepts of the formation of a diffusion layer of exchange ion in sulfo resin. On the other hand, when KB-4 is swelled in water, the effect does not disappear and, consequently, Fe^{3+} ions remain fixed at their exchange centers. Since a molecule of n-hexane in dis-

tinction from H_2O is nonpolar and incapable of forming a donor-acceptor bond with an iron ion, disassociation or weakening of the ion-polymer bond is excluded in this case as a result of the interaction of the ion with the molecules of the liquid. It follows from this that straightening of the resin changes when they swell in themselves and results in a decrease of force constants and accordingly to an increase of the amplitude of ion oscillations. The assumption that iron ions in KU-2 are converted during interaction with water to a liquid phase, in that those in KB-4 remain fixed at their exchange centers, is confirmed by the results obtained in these same resins with precipitated iron hydroxide in other pours. Reconstitution of iron ions in KU-2 into a hydroxide results in the appearance of the Mossbauer effect in hydrated resins at room temperature. The effect in KB-4 in this case is naturally preserved. The values of the effect in ions and in iron hydroxide are

approximately equal in non-aqueous resins. It is interesting, however, that swelling in water results in a decrease of the effect not only in the ions, but also in the iron hydroxide, the value of the effect decreasing even more sharply in a hydroxide of KB-4 than in ions. This permits us to conclude that iron ions in hydrated resin with carboxyl groups is almost completely fixed at the exchange centers, and a significant decrease of the effect during swelling in water is explained mainly by the increase of the amplitude of fixed ion oscillations, and not by transfer of part of the ions to a liquid phase.

According to extraction conditions iron hydroxide and resins is either in the form of individual molecules linked to a polymer lattice by van der Waals forces, or in the form of aggregates, the dimensions of which are close to molecular. The result of such a highly dispersed state is spectrum asymmetry [5, 12] and an increase of quadrupole splitting of $\Delta E_Q = 0.77 \pm 0.08$ mm/sec at 300° K, at the same time that $\Delta E_Q = 0.55$ mm/sec for ordinary polycrystalline $\text{Fe}(\text{OH})_3$ [2]. It is interesting to note that the value of the effect on hydroxides in non-swollen resins hardly changes in the range from 77° K to 300° K, while the highly dispersed state of a substance is characterized, on the other hand, by a sharp temperature dependence of the effect [27, 28]. We may assume that iron hydroxide is subjected to severe compression in the pores when the resin is dried out, as a result of which the temperature dependence of the oscillation amplitude of hydroxide surface atoms decreases sharply.

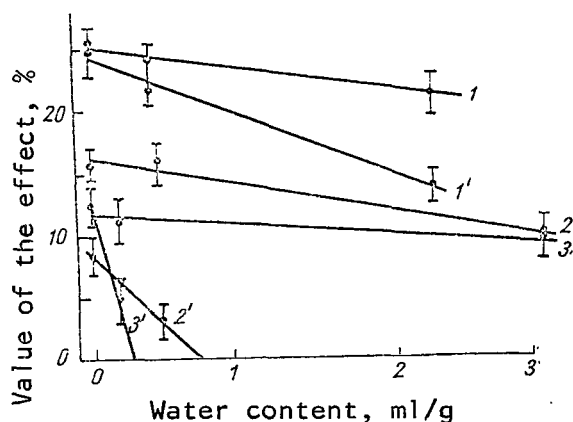


Figure 5. Dependence of the Change of Value of the Mossbauer Effect on the Amount of Water in the Resin: 1, 1', KB-4 ($T = 77^\circ \text{ K}$, 300° K); 2, 2', AV-16 with $(\text{FeCN}_6)^{-4}$ ($T = 77^\circ \text{ K}$, 300° K); 3, 3', AV-16 with $(\text{FeCN}_6)^{-3}$ ($T = 77^\circ \text{ K}$, 300° K).

Turning now to investigation of the structure of ion-exchange resins--anionites, we must note the fact that iron in anion is screened by ligandami and is less sensitive to the structure of the resin. However, even for anionites there is an effect of the resin swelling influence on the value of f' . Figure 5 shows the decrease of f' for anionites depending on the amount of water adsorbed. When the effect disappears completely, we can estimate the minimum amount of water required for complete rupture of the anion bonds with resin. It also turned out [19] that the electrical field gradient in a Mossbauer nucleus in highly basic anionites AV-17 is significantly greater than in poly functional anionite AV-16. A $(\text{FeCN}_6)^{-3}$ ion is most sensitive to a change of the electrical field gradient.

The Dynamics of Atomic Motion on the Surface and Surface Diffusion

The first experiment in this area was done to study the dynamics of the atomic motion of iron on the surface of $n\text{Al}_2\text{O}_3$ [12].

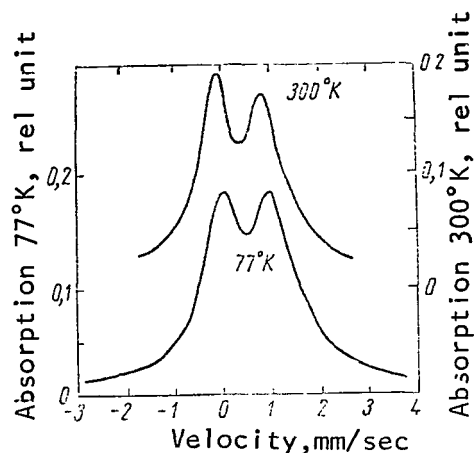


Figure 6. NGR Spectra of Fe^{57} , Chemosorbed in Al_2O_3 .

NGR spectra are given in Figure 6. The chemical shift of $\delta E_I = 0.45$ mm/sec indicates that adsorbed iron is in a trivalent state. Quadrupole splitting of $\Delta E_Q = 1.06$ mm/sec demonstrates a high electrical field gradient due to the asymmetry of the surface distribution of iron ions. Asymmetry of the spectrum lines appears at 300° K due to the anisotropy of the thermal oscillations of an atom on the surface. Assuming the sign of the electrical field gradient to be positive, we may conclude that projection of the moment of a nucleus of $3/2$ corresponds to the upper level of the excited state. From the value of asymmetry of A, anisotropy of the oscillations of iron ions is in a direction normal to the surface, and parallel to the surface. When $T = 300^\circ \text{ K}$

$\langle z^2 \rangle - \langle x^2 \rangle \approx 1 \times 10^{-18} \text{ cm}^2$, i.e., the amplitude of atomic oscillations normally toward the surface is greater than parallel to it. This corresponds to chemisorption, when an atom is located in the surface of a solid. However, the authors did not calculate absolute values of $\langle z^2 \rangle$ and $\langle x^2 \rangle$ in this paper. This was done for atoms of ten chemisorbed on the surface of silicagel with a specific surface of $\sim 300 \text{ m}^2/\text{g}$ in the form of SnO [5].

/144

Figure 7 shows the spectrum of SnO at $T = 213^\circ \text{ K}$. The figure shows spectral decomposition with the help of the M-20 machine for a single line of $\text{SnO}_2 \cdot n\text{H}_2\text{O}$ (1) and a doublet corresponding to SnO (2). As can be seen from the figure, spectral asymmetry ($T = 213^\circ \text{ K}$) appears as temperature increases. The electrical field gradient is axially symmetrical and its value is greater than zero for surface SnO due to the lack of electrons along the z axis [23]. Since the quadrupole moment of the nucleus of $\text{Sn}^{119}\text{Q} < 0$ [24], the nuclear level with $m_I = 3/2$ is located lower than $m_I = 1/2$.

Experimental determination-- $A = 0.80 \pm 0.08$ (at $T = 213^\circ \text{ K}$) yields $\langle z^2 \rangle - \langle x^2 \rangle \text{ SnO} = 1.3 \cdot 10^{-18} \text{ cm}^2$.

Thus, the mean square of the displacement of an atom of ten in a direction normal to the surface of the globule is greater than that along the surface. Assuming that $\langle x^2 \rangle = \langle y^2 \rangle$, and using the value of f for Sn on the surface of silicagel, we can find

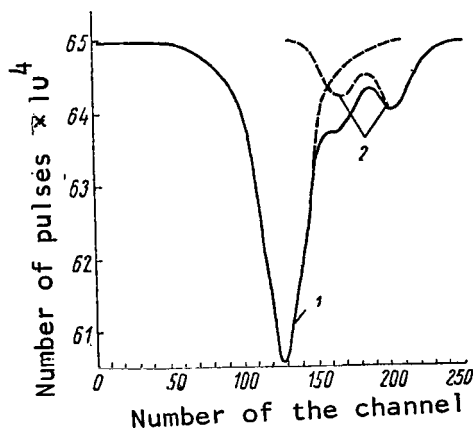


Figure 7. The NGR Spectrum of Sn on the Surface of Silicagel: 1, for $\text{SnO}_2 \cdot n\text{H}_2\text{O}$; 2, for SnO . The number of the analyzer channel of $1 \text{ c} = 0.052 \text{ mm/sec}$ is plotted on the axis of the abscissae, and the selected number of pulses-- along the axis of the ordinates.

tungsten. The two outer lines give $\theta_D = 354^\circ \text{ K}$ for oscillations perpendicular to the surface, and $\theta_D = 255^\circ \text{ K}$ for oscillations along the surface. These results agree with the following relationships for mean squares of the displacements of Co^{57} atoms on the surface of tungsten.

$$\frac{\langle x^2 \rangle_{\parallel}}{\langle x^2 \rangle_{\perp}} = 1,9 \pm 0,4; \quad \frac{\langle x^2 \rangle_{\perp}}{\langle x^2 \rangle_{\text{inside}}} = 1,3 \pm 0,2;$$

$$\frac{\langle x^2 \rangle_{\parallel}}{\langle x^2 \rangle_{\text{inside}}} = 2,5 \pm 0,5.$$

The atoms of Co^{57} here in distinction from the papers [5] and [12] are on the surface and the mean square of atomic displacement along the surface is greater than that normal to it.

In [26] a 0.01 monolayer of Co^{57} was evaporated onto a silicon surface (100) and (111), previously cleaned in a vacuum. The spectrum yielded two lines with $\Delta E_Q = 0.7 \text{ mm/sec}$ because of the electrical gradient on the surface. The Co^{57} diffused internally at 1000° K and the spectrum resembled that of Co^{57} inside silicon. It was established that in the temperature range of 300 and 800° K , the Doppler effect of the second order yields $\delta E_D/E = -2.05 \pm \pm 0.16 \cdot 10^{-15}/\text{K}^0$ for atoms on the surface and $\delta E_D/E = -2.17 \pm 0.16 \cdot 10^{-15}/\text{K}^0$

$$\langle z^2 \rangle - \langle x^2 \rangle = 1,3 \cdot 10^{-18} \text{ cm}^2;$$

$$\langle z^2 \rangle + 2\langle x^2 \rangle = 2,77 \cdot 10^{-18} \text{ cm}^2,$$

hence $\langle x^2 \rangle = 0.46 \cdot 10^{-18} \text{ cm}^2$ and $\langle z^2 \rangle = 176 \cdot 10^{-18} \text{ cm}^2$. The difference in $\langle x^2 \rangle$ and $\langle z^2 \rangle$ disappears at a temperature of 93° K .

Paper [25] investigated the dynamics of Co^{57} motion on the surface of tungsten, i.e., the radiation source was used as the object of study. A 0.1 monolayer of Co^{57} was evaporated onto a tungsten substrate. The experiment was conducted in a vacuum (10^{-9} mm Hg). Measurements were made for two angles between the direction of γ -photon escape and that normal to the surface of the sample ($\theta = 0$ and 60°). The spectrum consisted of three unresolved lines. The central line indicates the temperature dependence corresponding to a Debye temperature of 403° K , and corresponds to Co^{57} atoms diffused inside the

/145

for internal. As a result experimental confirmation was obtained of the decrease of the shift due to the Doppler effect of the second order for atoms located on the surface.

Let us now dwell on the dynamics of motion of atoms on the surface of the solid not because of adsorption, but due to the fact that they are boundary atoms in a normal crystal lattice.

Highly dispersed white tin with particle diameters of 250, 370, 650 and 1550 Å were investigated [27]. The average size of the particles is determined with the help of an electron microscope. The dependence $f' = F(T, d)$ was investigated. The results of the investigations indicate that f' decreases as the diameter of the particles of tin decreases, beginning at $d = 600$ Å, and the temperature dependence becomes sharper. Figure 8 shows the decrease of the value of f' at 93° K as the diameter of the particle decreases and as the specific surface α increases, $f' - f'_\infty \sim 1/d$ (f'_∞ is the probability of

/146

γ -resonance of a foil of β Sn, and d is the diameter of the particle), and $\alpha \sim 1/d$, i.e., the change of f' and α correspond to the same law. This indicates a direct link of the decrease of f' in highly dispersed tin with an increase of the specific surface. Assuming that decrease of f' is caused only by atoms of tin going into the surface layer to a depth of five constants of the lattice, the values of f'_{theor} were calculated according to [6, 7]. The experimental results in this case indicate that f' for surface atoms decreases much more rapidly than follows from theoretical models. The Debye temperature was calculated for particles with a different diameter, and for five surface layers. The estimates given for particles with $d = 600$ Å are $\theta = 135^\circ$ K; $d = 370$ Å, $\theta = 130^\circ$ K and $d = 250$ Å, $\theta = 120^\circ$ K. The average for five surface layers is $\theta \sim 100^\circ$ K. Weak forces influence surface atoms of β Sn, which causes an increase of the mean square of atomic displacement and a decrease of f' .

Paper [5] also investigated the dynamics of the motion of atoms of tin, sorbed due to physical sorption on the surface of silicagel in the form of $\text{SnO}_2 \cdot$

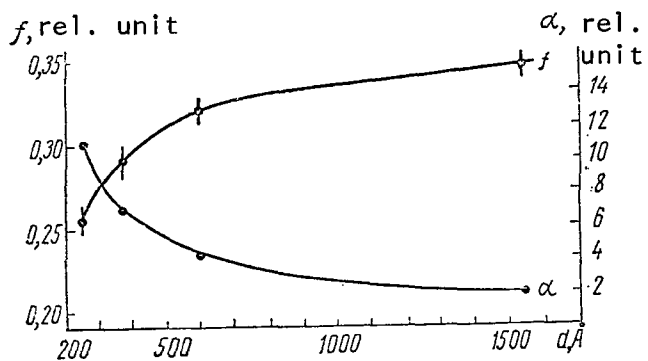


Figure 8. Dependence of f' and Specific Surface α on the Diameter of the Particles d .

$\cdot n\text{H}_2\text{O}$. Figure 9 shows the dependence of the value of the effect on temperature for chemisorbed tin and tin sorbed due to physical sorption. In connection with the fact that chemisorbed atoms of tin are maintained on the surface by stronger bonds than physically sorbed atoms of tin which are bound to the surface by weak van der Waals forces, the temperature dependence of f' for chemisorbed atoms should be weaker than is indicated in Figure 9.

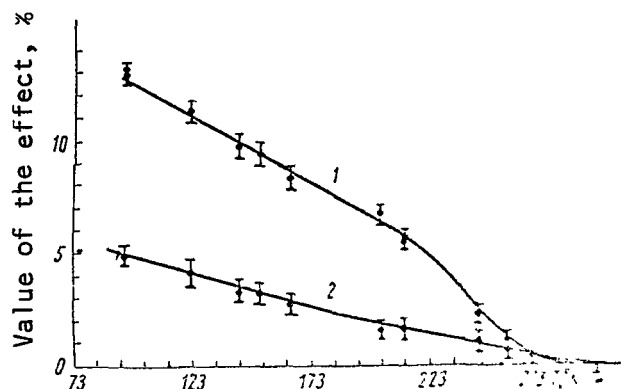


Figure 9. Temperature Dependence of the Value of the Mossbauer Effect for Physically Sorbed Tin in the Form of $\text{SnO}_2 \cdot n\text{H}_2\text{O}$ (1) and Chemosorbed Tin in the Form of SnO_2 (2).

As a result it becomes possible to separate physical and chemical sorption. The probability of the Mossbauer effect in the case of physical sorption of $\text{SnO}_2 \cdot n\text{H}_2\text{O}$ on the surface will be determined by the displacement of an individual atom of tin per molecule and by displacement of the entire molecule of $\text{SnO}_2 \cdot n\text{H}_2\text{O}$ ($f = f_M \cdot f_A$). Having the experimental curve of $\langle x^2 \rangle = F(T)$ for $\text{SnO}_2 \cdot n\text{H}_2\text{O}$, with the help of the dependence

$$\langle x^2 \rangle_{\text{SnO}_2 \cdot n\text{H}_2\text{O}} = \langle x^2 \rangle_{0 \text{ mol}} \coth \alpha_{\text{mol}}/T + \langle x^2 \rangle_{0 \text{ at}} \coth \alpha_{\text{at}}/T,$$

we find the coefficients of $\langle x_0 \rangle$ and α and calculate the energy of zero oscillations-- $E_{0 \text{ mol}} = 0.26 \cdot 10^{-2} \text{ ev}$ and $E_{0 \text{ at}} = 1.9 \cdot 10^{-2} \text{ ev}$. When $T = 0^\circ \text{ K}$, f' is determined mainly by the value of f'_A , but at higher temperatures the oscillations of the molecule itself play the predominant role in the decrease of f' . The amplitude of molecular oscillations increases strongly above 230° K , which is characterized by a sharp decrease of the value of the effect. This is apparently related to fusion of the surface bond of $\text{SnO}_2 \cdot n\text{H}_2\text{O}$. The molecule is torn away from the localization center and begins to jump from one localized position to another. However, due to the smallness of the value of the effect, no spreading of the lines because of such jumps was noted.

Cation diffusion due to jumps from one localized position to another was studied in zeolites [18] and in more detail in ion-exchange resins [19]. The capability of Fe^{2+} cations to diffuse in zeolite pores when there is a molecule of hexane present resulted in spreading of the Fe^{2+} lines at temperatures of 213 and 293° K (Figure 10). Assuming the distance between the localization centers as $l \sim A$, which is related to the structure of zeolite M, we can estimate that $\tau \sim 3.9 \cdot 10^{-8} \text{ sec}$, $D = 0.68 \cdot 10^{-8} \text{ cm}^2/\text{sec}$ ($T = 213^\circ \text{ K}$) and $\tau = 2.2 \cdot 10^{-8} \text{ sec}$, $D \sim 1.2 \cdot 10^{-8} \text{ cm}^2/\text{sec}$ ($T = 300^\circ \text{ K}$). The lines of trivalent iron in both zeolites and in ion-exchange resins did not spread as temperature increased.

The self-diffusion of Fe^{2+} cations with the presence of water and hexane in the resin pores was studied in the case of ion-exchange resin KU-2. Figure 11, a shows the experimental dependence of $\Gamma_{\text{exp}} = f(T)$. The values of Q and τ_0 which in the case of hexane were equal to 5 kcal/mole and $7 \cdot 10^{-13} \text{ sec}$, and in

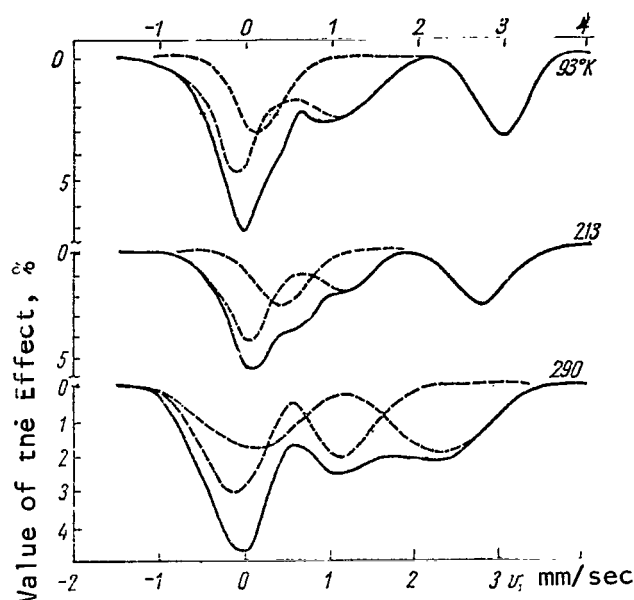


Figure 10. NGR Spectra of $\text{Fe}^{57}\text{M} + n\text{-C}_6\text{H}_{14}$ at Different Temperatures.

the case of water--0.8 kcal/mole and $1 \cdot 10^{-8}$ sec, were calculated on the basis that the time of duration of an atom or molecule on the surface of a solid in a depression of depth Q is determined by the relationship $\tau = \tau_0 \exp Q/RT$. We note that diffusion of Fe^{2+} begins in the region of hexane melting ($\sim 190^\circ \text{K}$). The least energy of activation for diffusion of Fe^{2+} in KU-2 when there is water in the molecule pours is apparently related to the polar characteristics of water molecules which decreases diffusion activation energy.

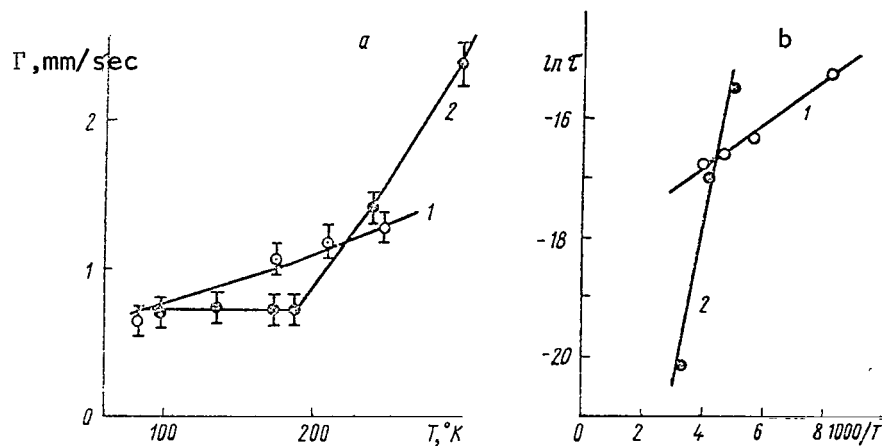


Figure 11. Change of $\Gamma = f(T)$:
a, for Fe^{2+} in KU-2 + H_2O (curve 1);
for Fe^{2+} in KU-2 + C_6H_{14} (curve 2);
b, $\ln \tau = f(1/T)$ for Fe^{2+} in KU-2 + H_2O ; $\ln \tau = f(1/T)$ for Fe^{2+} in KU-2 + C_6H_{14} .

Study of elementary processes of adsorption and catalysis with the help of nuclear γ -resonance still requires significant improvement of the method. It is necessary that all processes of aging the sample, sorption and obtaining the spectrum be carried out in a vacuum of 10^{-6} mm Hg. Only in such conditions is it possible to obtain a clear interpretation of NGR spectra and to compare study of surface effects, such as infrared spectroscopy, EPR and NMR with such widely used methods. However, the results obtained, despite nonfulfillment of the third of these conditions (a vacuum of $\sim 10^{-6}$ during the measuring process), permits us to draw initial conclusions about the nature of atomic interactions on the surface of a solid.

In [22] a study was conducted of the adsorption of tetramethyl tin on the surface of Al_2O_3 , silicagel and aluminosilicate. It was shown that the appearance of the spectrum depends substantially on adsorption temperature. The spectra of freshly prepared samples obtained at an adsorption temperature of -30°C , differed sharply from the spectra of samples which had been left in air for a day or more. Figure 12 shows the spectra of the reference $(\text{CH}_3)_4\text{Sn}$ adsorbed on Al_2O_3 at -30°C of a freshly prepared sample and one kept in air for twenty and thirty-five hours at an adsorption temperature of -30°C . Besides the reference tetramethyl tin, two secondary peaks are observed, which are apparently a doublet, which may be related to chemisorbed $(\text{CH}_3)_4\text{Sn}$. In connection with the fact that the spectra of $\text{R}_3\text{SnOR}'$ and R_3SnOH are similar to the spectrum attributed to chemisorbed $(\text{CH}_3)_4\text{Sn}$, we make the conclusion that the adsorption sinters are either oxygen atoms or hydroxyl groups. The presence of lines of the reference substance is attributed to physically adsorbed $(\text{CH}_3)_4\text{Sn}$. Aging it at room temperature for twenty hours results in an increase of doublet intensity. Further aging of the sample to thirty-five hours causes a radical change of the spectrum. Two new lines appear which correspond either to a change of the bonds in a molecule of $(\text{CH}_3)_4\text{Sn}$ with adsorbed sinters or a change of the properties of the sinters themselves. Adsorption on silicagel and aluminosilicate takes place simultaneously, but the rate of the processes is somewhat different as are the properties of the adsorbed sinters. The conclusion about the activated nature of tetramethyl tin adsorption is made on the basis of the dependence of the spectrum appearance on adsorption temperature and adsorption kinetics on the type of adsorbent. Chromatographic analysis of the gas phase of Al_2O_3 with tetramethyl tin adsorbed on it at room temperature indicated the presence of methane and ethane, and also small amounts of other hydrocarbons. This is apparently related to the dissociative nature of tetramethyl tin adsorption on the surface. Significant electrical field gradients occur in connection with the asymmetry of atomic distribution on the surface, which leads to increase of the value of ΔE_Q on the surface. /150

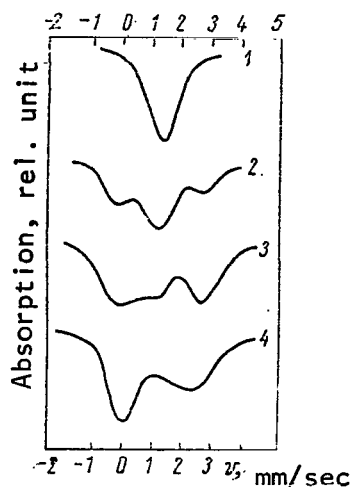


Figure 12. NGR Spectra: 1, Reference $(\text{CH}_3)_4\text{Sn}$; 2, Adsorbed on Al_2O_3 at $T = -30^\circ\text{C}$; 3, Aged in air for 20 hours; 4, For 35 hours.

Rough calculation of quadrupole interaction is carried out for Fe^{3+} , chemisorbed on $\eta\text{Al}_2\text{O}_3$ [12]. Assuming the position of an Fe^{3+} ion in a surface state near an adjacent neighbor of O^{2-} to be octahedral and assuming the charge as equal to +2 at a normal distance to oxygen neighbors, we find the electrical field gradient in the nucleus for γ_∞ (constants of antiscreening) equal to - 6.18. We obtain $\Delta E_Q = 1.6 \text{ mm/sec}$ at $Q = 0.28 \text{ barn}$, which is close to the value obtained from the experiment.

An increase of ΔE_Q , especially at high temperatures, was also observed for Sn on the surface of silicagel [5]. The surface form of SnO has a value of $\Delta E_Q = 1.72 \pm 0.07$ at $T = 93^\circ \text{ K}$ (for crystalline SnO $\Delta E_Q = 1.3 \text{ mm/sec}$), and $\Delta E_Q = 2.18 \pm 0.07 \text{ mm/sec}$ at $T = 257^\circ \text{ K}$. /151

Determination of the nature of interaction of adsorbed atoms during formation of an intermediate process is important for understanding the process of catalysis.

The surface form of SnO_2 in highly dispersed βSn [28] with particle dimensions of 300 and 1000 Å was studied. Having an electron environment similar to the normal polycrystalline form of SnO_2 , the Sn atoms on the surface have large mean square displacements which results in a decrease and a sharper temperature dependence of f' . X-ray diffraction analysis indicated an absence of SnO_2 on the surface at oxidation temperatures to 400° C . Oxidation at 500° C yielded ~50% SnO_2 according to X-ray diffraction analysis. The NGR even at room temperature oxidation indicated the presence of SnO_2 with an unusually sharp temperature dependence, which becomes normal at an oxidation temperature of 500° C . Apparently a dioxide of SnO_2 close to the amorphous phase is formed on the surface of the particles at low-temperature oxidation (less than 400° C), which was not detected by X-ray diffraction analysis, but which displays the Mossbauer effect. Amorphous SnO_2 changes to an ordinary crystalline state at a temperature of $\sim 500^\circ \text{ C}$, according to X-ray diffraction analysis.

Highly Dispersed Systems

Determination of the role played by the effect of a decrease of particle size to hundreds and tens of angstroms on the structure of such particles, the

frequency spectrum of atomic oscillations, the temperature of phase transitions etc. is of special interest.

Non-magnetic materials, for example tin [27] and gold [29], are naturally selected for easier and more reliable study of the change of the frequency spectrum of highly dispersed particles.

An increase of f' was obtained for highly dispersed gold with particle dimensions of 60 Å when compared with $d = 200$ Å in the temperature range of 4-63° K. The increase of f' is related to the change of the phonon spectrum of internal atoms in these gold particles. Actually, since the wave length of phonons cannot be greater than a particle size of 60 Å, lower frequencies may not be excited in the spectrum and f' should increase. However, the effect of surface atoms (~50% for two layers from the surface) is very great for such small particles, which should cause f' to decrease. Obviously a change of the frequency spectrum in the given case is so great that it overshadows the effect of surface atoms. No changes of the phonon spectrum of internal atoms in the temperature range of 93-300° K was noted for highly dispersed tin [27], and the decrease of f' as the size of the particles decreases is related only to surface effects. /152

The results of several experiments are known on the study of the ferromagnetism of highly dispersed systems and thin films. The first of them [30] was conducted in highly dispersed Fe_2O_3 with a particle diameter of 50 Å. It was determined for such particles that the Neel point decreased sharply compared to ordinary $\alpha\text{Fe}_2\text{O}_3$ (~900° K) and lies between 300 and 120° K. There is a paramagnet at room temperature with strong quadrupole splitting, and an antiferromagnet at 120° K.

In [31] it was found that there is no point on highly dispersed Fe_2O_3 precipitated in silicagel pours, below which magnetization of M is parallel to the electrical field gradient (for $\alpha\text{Fe}_2\text{O}_3$, $T_{\text{Morin}} = 263^\circ \text{ K}$) and always $M \perp V_{zz}$.

Assuming the probability of spin flip $e^{-\frac{2Kv}{kT}}$ where K is the constant of anisotropy, and v is the volume of the particle, it was found that the energy of anisotropy varies from $4.7 \cdot 10^4$ ergs/cm³ to $4.1 \cdot 10^4$ ergs/cm³ for particles of 100, 135, 150, 180 Å.

Another antiferromagnet FeOOH , which has a Neel point of 400° K, was investigated in [32, 33].

As the size of the particles decreases, paramagnetism increases and susceptibility increases [32]. This occurs in an antiferromagnetic due to deterioration of the balance of two magnetic sublattices. The Neel point decreases as the particle sizes decrease.

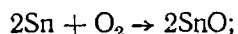
The Neel point is equal to 294° K for particles with a volume of $3 \cdot 10^{-17}$ cm³, and is equal to 210° K for particles with a volume of $1 \cdot 10^{-17}$ cm³ (~60 Å). The energy of anisotropy corresponds to $1 \cdot 10^4$ and $1.5 \cdot 10^4$ ergs/cm³. As a

result it is obvious that highly dispersed particles are a quite suitable object to study the time change of spin relaxation. In [33] the Neel point decreased for particles of FeOOH $d = 500 \text{ \AA}$, while in the case of Fe_2O_3 this decrease is observed for particles $< 100 \text{ \AA}$ (the energy of anisotropy is higher for Fe_2O_3).

A substantial decrease of the Curie point was also found for highly dispersed particles of NiFe_2O_4 and CoFe_2O_4 [34] as particle size decreased, i.e., as relaxation time of electron spin decreased, which leads to the phenomenon of superparamagnetism. Ultrathin films 1.2-15 Å thick, applied to silicon oxide were also investigated [35]. Successive layers of Fe (92% Fe^{57}) and SiO were applied in a vacuum $3 \cdot 10^{-8} \text{ mm Hg}$. The magnetic field in the nucleus has a common value for the films of $\sim 15 \text{ \AA}$ and thicker. The field for thinner films decreases slightly; it is 4% less for 6 Å than for films 15 Å thick. The spectrum of a 6 Å film shows quadrupole splitting of $\Delta E_Q = 0.12 \pm 0.03 \text{ mm/sec}$, and quadrupole splitting is completely lacking for thicker films. Quadrupole splitting of $\Delta E_Q = 0.6 \text{ mm/sec}$ for 1.2-4.6 Å films. All films except 4.6 Å, when measured at 4.2° K, yield the same spectrum as those at room temperature (6 lines). The spectrum of a 4.6 Å film consists of 2 lines at $T = 298^\circ \text{ K}$ and 6 lines at $T = 4.2^\circ \text{ K}$. A mixed spectrum was observed at temperatures of 20-77° K. The data obtained indicate that the Curie point decreases as film thickness decreases. The conclusion is made of a sharp change of the Curie point, ΔE_Q and H , when film thickness becomes an order of two parameters of the lattice, which suggests the presence of a critical film thickness.

Topochemical Reactions

Study of the mechanism of topochemical reactions is interesting both from the point of view of preparing catalysts with different catalytic activity, as well as from the point of view of determining the interaction of the different phases during the reaction process. NGR spectroscopy was first used to study the topochemical reaction of the oxidation of highly dispersed tin [28]. It was shown that oxidation of highly dispersed tin up to the melting point is made difficult by the SnO_2 which formed on the surface; however, the nature of oxidation changes sharply above the melting point of tin. Intensive formation of SnO takes place, which becomes much greater for 300 Å particles than for βSn . However, spectra up to 400 Å indicate the presence of non-oxidized tin, βSn being greater at an oxidation temperature of 300° C than for SnO for particles of 1000 Å. These results indicate that oxidation takes place up to 400°C apparently due to the reaction



and the reaction $2\text{SnO} + \text{O}_2 \rightarrow 2\text{SnO}_2$, which is characterized by a disappearance of SnO without formation of βSn , plays a very small role.

Above 400° C the reaction $2\text{SnO} + \text{O}_2 \rightarrow 2\text{SnO}_2$ becomes intense and all tin is oxidized into SnO_2 . Papers [36, 37] studied the reaction of thermal decomposition of an oxalate of trivalent iron in air [36] and in a nitrogen atmosphere [37]. As a result of experiment [36] highly dispersed Fe_2O_3 was detected, but the mechanism of its formation with, and also the stages of the reaction of the composition of a trivalent iron oxalate were not established in this case.

The experiments of [37] investigated the decomposition of an oxalate of bivalent and trivalent iron using a complex method--NGR and derivatography. The derivatograph made it possible to obtain curves of weight change, differential weight change, temperature change and differential temperature change during thermal decomposition at a uniformly increasing temperature. Figure 13 shows the differential curves of the change of weight DTG and temperature DTA and the spectra of nuclear γ -resonance obtained at the points indicated. The differential curves for an oxalate of bivalent iron have two minimums of 200 and 400° C, and for an oxalate of trivalent iron they have three minimums of 200, 260 and 400° C.

/155

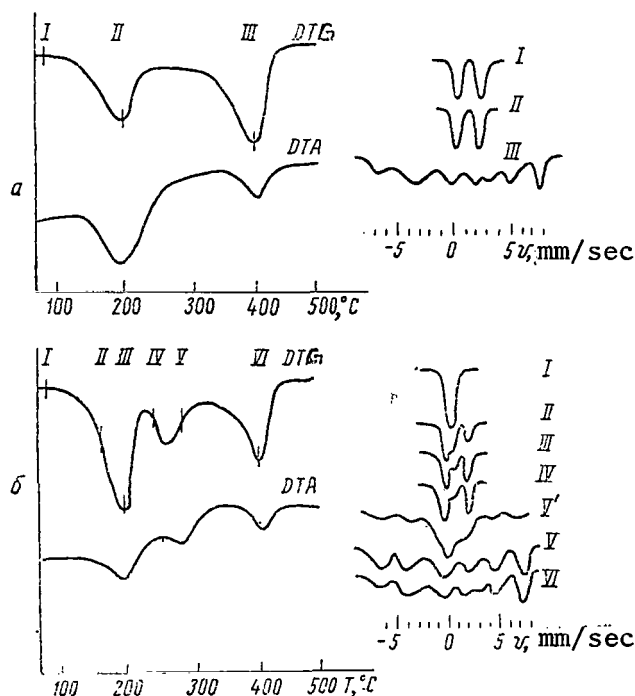
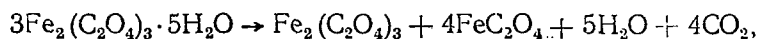
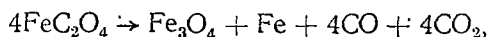


Figure 13. Derivatogram and NGR Spectrum of Thermal Decomposition of $\text{FeC}_2\text{O}_4 \cdot 2\text{H}_2\text{O}$ (a) and $\text{Fe}_2(\text{C}_2\text{O}_4)_3 \cdot 5\text{H}_2\text{O}$ (b), respectively (points at which samples were taken for studies by the NGR method are indicated on the derivatograms).

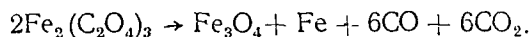
NGR spectra indicate that the first phase transition at 200° C for $\text{Fe}_2(\text{C}_2\text{O}_4)_3 \cdot 5\text{H}_2\text{O}$ is related to decomposition into FeC_2O_4 and $\text{Fe}_2(\text{C}_2\text{O}_4)_3$ with simultaneous dehydration.



a certain amount of $\text{Fe}_2(\text{C}_2\text{O}_4)_3$ remaining. The first phase transition for $\text{FeC}_2\text{O}_4 \cdot 2\text{H}_2\text{O}$ at 200° C is simply related to dehydration of $\text{FeC}_2\text{O}_4 \cdot 2\text{H}_2\text{O} \rightarrow \text{FeC}_2\text{O}_4 + 2\text{H}_2\text{O}$. The third phase transition at 400° C for $\text{Fe}_2(\text{C}_2\text{O}_4)_3 \cdot 5\text{H}_2\text{O}$ coincides with the second phase transition for $\text{FeC}_2\text{O}_4 \cdot 2\text{H}_2\text{O}$. NGR spectra indicate the appearance of Fe_3O_4 and Fe and subsequently the reaction



which is characterized by decomposition of an oxalate of bivalent iron, is observed in both cases. The relationship of the second phase transition at 260° C with the remaining $\text{Fe}_2(\text{C}_2\text{O}_4)_3$ now becomes clear:



However, this reaction yields Fe_3O_4 in a very specific state in distinction from the preceding reaction. Figure 13 showed the NGR spectra of an oxalate of trivalent iron at a decomposition temperature of 300° C. The appearance of the spectra is strongly dependent on the temperature of change. At 300° K almost all the Fe_3O_4 is in a paramagnetic state and yields a single line in the spectrum. Six lines characteristic of Fe_3O_4 in an antiferromagnetic state appear in the NGR spectrum taken at 77° K. Thus, Fe_3O_4 with a severely decreased Neel point when compared with the normal phase (a Neel point of ~900°K) is obtained at a decomposition temperature of 220-320° C. All of this suggests formation of an oxide of Fe_3O_4 in a highly dispersed state with particle dimensions less than 100 Å, and having, according to the preceding [26-30], a decreased Neel point, in the temperature range of 220-320° C. Such properties of an oxide of Fe_3O_4 formed make it desirable to study it further, especially in catalysis.

The consideration given the applicability and possibilities of NGR as a method of investigating the physical and chemical properties of the surface of a solid shows its unconditionally high effectiveness and comparability with results of infrared spectroscopic, electron paramagnetic resonance and nuclear magnetic resonance.

REFERENCES

1. Méssbauer, R. L., *Z. Phys.*, Vol. 151, p. 124, 1958.
2. Gol'danskiy, V. I., *Effect Messbauera i ego Primeneniye v Khimii* [The Mossbauer Effect and its Application in Chemistry], *USSR Academy of Sciences*, Moscow, 1963.
3. Shapiro, F. L., *Uspekhi Fiz. Nauk*, Vol. 72, p. 685, 1960.
4. Wallis, R. F., *Surface Science*, Vol. 2, p. 146, 1964.
5. Suzdalev, I. P. et al, *Zh. Eksperim. i Teor. Fiz.*, Vol. 49, p. 1424, 1965.
6. Rich, M., *Phys. Lett.*, Vol. 4, p. 153, 1963.
7. Maradudin, A. A. and I. Meingailis, *Phys. Rev.*, Vol. 133, p. A1188, 1964.
8. Clark, B. C., R. Herman, and R. F. Wallis, *Bull. Amer. Phys. Soc.*, Vol. 9, p. 624, 1964.
9. Gol'danskiy, V. I., Ye. F. Makarov and V. V. Khrapov, *Zh. Eksperim. i Teor. Fiz.*, Vol. 44, p. 752, 1963.
10. Karyagin, S. V., *Dokl. AN SSSR*, Vol. 148, p. 1102, 1963.
11. Gol'danskiy, V. I. et al, *Dokl. AN SSSR*, Vol. 147, p. 127, 1962.
12. Flinn, P. A., S. L. Ruby and W. Kehl, *Science*, Vol. 143, p. 1434, 1964.
13. Singwi, K. S. and A. Sjolander, *Phys. Rev.*, Vol. 120, p. 1093, 1960.
14. Frauenfel'der, G., *Effekt Messbauera* [The Mossbauer Effect], *Atomizdat. Press*, Moscow, 1964.
15. Class, L. and M. Klein, *Phys. Rev.*, Vol. 109, p. 288, 1958.
16. Blume, M., *Phys. Rev. Lett.*, Vol. 14, p. 96, 1965.
17. Wickmann, H. H. and A. M. Trozzolo, *Phys. Rev. Lett.*, Vol. 15, p. 156, 1965.
18. Gol'danskiy, V. I. et al, *Dokl. AN SSSR*, Vol. 169, p. 872, 1966.
19. Suzdalev, I. P., *Zh. Fiz. Khimii*, Vol. 11, 1967.
20. Dubinin, M. M., *Dokl. AN SSSR*, Vol. 159, p. 166, 1964.
21. Neymark, I. Ye., *Izv. AN SSSR, Ser. Khim.*, No. 6, p. 959, 1965.
22. Karasev, A. N. et al, *Kinetika i Kataliz*, Vol. 6, p. 710, 1965.
23. Gordi, V., V. Smit and R. Trambarulo, *Radiospektroskopya* [Radiospectroscopy], p. 275, *Gostekhzdat Press*, Moscow, 1955.
24. Boyle, A. I. F., D. S. P. Bunbury and C. Edwards, *Proc. Phys. Soc.*, Vol. 79, p. 416, 1962.
25. Burton, J. W., H. Frauenfelder and R. P. Godwin, *Appl. Mossb. Effect in Chem. and Sos. St. Phys.*, p. 73; IAEA, Vienna, 1966.
26. Allen, F. G., *Bull. Amer. Phys. Soc.*, Vol. 9, p. 296, 1964.
27. Suzdalev, I. P. et al, *Zh. Eksperim. i Teor. Fiz.*, Vol. 51, p. 118, 1966.
28. Suzdalev, I. P. et al, *Kinetika i Katalaz*, Vol. 6, p. 1108, 1965.
29. Marshall, S. W. and R. M. Wilenzik, *Phys. Rev. Lett.*, Vol. 16, p. 219, 1966.
30. Nakamura, T. et al, *Phys. Lett.*, Vol. 12, p. 178, 1964.
31. Kundig, W. et al, *Phys. Rev.*, Vol. 142, p. 327, 1966.
32. Shinjo, T. J., *J. Phys. Soc. Jap.*, Vol. 21, p. 917, 1966.
33. Van der Kraan, A. M. and J. J. Loeff, *Phys. Lett.*, Vol. 20, p. 614, 1966.
34. Schuele, W. J., S. Shtrocmán and D. J. Treves, *Appl. Phys.*, Vol. 36, p. 1010, 1965.
35. Lee, E. L. and P. E. Boldue, *Violet Phys. Rev. Lett.*, Vol. 13, p. 800, 1964.
36. Gallagher, P. K. and G. R. Kurkjian, *Inorg. Chem.*, Vol. 5, p. 214, 1966.
37. Suzdalev, I. P. et al, *Kinetika i Kataliz*, Vol. 7, p. 919, 1966.

Translated for the National Aeronautics and Space Administration under Contract No. NASw-1695 by Techtran Corporation, P.O. Box 729, Glen Burnie, Md. 21061

NATIONAL AERONAUTICS AND SPACE ADMINISTRATION
WASHINGTON, D. C. 20546
OFFICIAL BUSINESS

FIRST CLASS MAIL



POSTAGE AND FEES PAID
NATIONAL AERONAUTICS AND SPACE ADMINISTRATION

140 001 54 51 305 70151 00903
AIR FORCE WEAPONS LABORATORY /WL0L/
KIRTLAND AFB, NEW MEXICO 87117

ATTN: LEO BULMAN, CHIEF, TECH. LIBRARY

POSTMASTER: If Undeliverable (Section 158
Postal Manual) Do Not Return

"The aeronautical and space activities of the United States shall be conducted so as to contribute . . . to the expansion of human knowledge of phenomena in the atmosphere and space. The Administration shall provide for the widest practicable and appropriate dissemination of information concerning its activities and the results thereof."

—NATIONAL AERONAUTICS AND SPACE ACT OF 1958

NASA SCIENTIFIC AND TECHNICAL PUBLICATIONS

TECHNICAL REPORTS: Scientific and technical information considered important, complete, and a lasting contribution to existing knowledge.

TECHNICAL NOTES: Information less broad in scope but nevertheless of importance as a contribution to existing knowledge.

TECHNICAL MEMORANDUMS: Information receiving limited distribution because of preliminary data, security classification, or other reasons.

CONTRACTOR REPORTS: Scientific and technical information generated under a NASA contract or grant and considered an important contribution to existing knowledge.

TECHNICAL TRANSLATIONS: Information published in a foreign language considered to merit NASA distribution in English.

SPECIAL PUBLICATIONS: Information derived from or of value to NASA activities. Publications include conference proceedings, monographs, data compilations, handbooks, sourcebooks, and special bibliographies.

TECHNOLOGY UTILIZATION PUBLICATIONS: Information on technology used by NASA that may be of particular interest in commercial and other non-aerospace applications. Publications include Tech Briefs, Technology Utilization Reports and Technology Surveys.

Details on the availability of these publications may be obtained from:

SCIENTIFIC AND TECHNICAL INFORMATION DIVISION
NATIONAL AERONAUTICS AND SPACE ADMINISTRATION
Washington, D.C. 20546